# DEVELOPMENT OF HIGH BAND GAP MATERIALS FOR TANDEM SOLAR CELLS AND SIMULATION STUDIES ON MECHANICAL TANDEM SOLAR CELLS

by

VISHNUVARDHANAN VIJAYAKUMAR

A Dissertation submitted to the

Graduate School-New Brunswick

Rutgers, The State University of New Jersey

In partial fulfillment of the requirements

For the degree of

Doctor of Philosophy

Graduate Program in Materials Science and Engineering

Written under the direction of

Dunbar P. Birnie, III

And approved by

_____

_____

_____

_____

New Brunswick, New Jersey

October, 2013

# ABSTRACT OF THE DISSERTATION

DEVELOPMENT OF HIGH BAND GAP MATERIALS FOR TANDEM SOLAR CELLS AND SIMULATION STUDIES ON MECHANICAL TANDEM SOLAR CELLS

By VISHNUVARDHANAN VIJAYAKUMAR

Dissertation Director

Dr. Dunbar P. Birnie, III

Development of low cost, high efficiency tandem solar cells is essential for large scale adoption of solar energy especially in densely populated regions of the world. In this thesis four-terminal mechanical (stack like) tandem solar cells were evaluated using detailed simulation models and design criteria for selecting candidate materials were established. Since silicon solar cells are low cost and have a multi-giga watt global manufacturing and supply chain capacity already in place then only tandem stacks incorporating silicon as one of the layeres in the device was investigated. Two candidate

materials which have high band gaps that could be used as top cells in the mechanical tandem device were explored as part of the thesis.

Dye-sensitized solar cells (DSSC) sensitized with N719 dye (one of the candidates for the top cell) were fabricated with the goal of enabling a flexible processing path to lower cost. Stainless steel (SS) mesh substrates were used to fabricate anodes for flexible DSSC in order to evaluate them as replacements for more expensive Transparent Conducting Oxides (TCO's). Loss mechanisms in DSSC's due to SS mesh oxidation were quantified and protective coatings to prevent oxidation of SS mesh were developed. The second material which was evaluated for use as the top cell was copper zinc tin sulfide (CZTS). CZTS was deposited through a solution deposition route. Detailed investigations were done on the deposited films to understand the chemistry, crystal structure and its opto-electronic properties. Deposited CZTS films were found to be highly crystalline in <112> direction. The films had a direct band gap of 1.5 eV with absorption coefficient greater than $10^4$ $cm^{-1}$ in agreement with published values.

In the second part of the thesis detailed electrical and optical simulation models of the mechanical tandem solar cells were developed based on the most up-to-date materials physical constants available for each layer. The modeling was used to quantify the various theoretical and practical loss mechanisms in tandem devices. Two configurations were evaluated, first was silicon / germanium tandem cell and the second was gallium arsenide / silicon tandem cell. The simulation models were validated by their close match to the performance of experimental standalone solar cells devices reported in the literature.

Finally the efficiency limits of the present generation of high band gap solar cells were discussed. Voltage and current loss of the high band gap solar cells were compared with present generation silicon solar cells and challenges in improving their efficiencies were described.

# ACKNOWLEDGEMENTS

I would like to thank my adviser Prof. Dunbar P. Birnie, for providing me tremendous support and guidance during the course of my graduate life. His deep insights into the world of renewable energy were invaluable and I appreciate all the long and helpful discussions I have had with him over the last 5 years. He provided me with immense freedom to explore the world of solar energy, emphasizing always on finding solutions to 'real world' problems.

I would also like to thank Dr. Aurelien Du Pasquier for teaching me about dye-sensitized solar cells and motivating me through my PhD. I would like to thank Dr. Sarika Phadke, Dr. Sukanya Murali, Dr. Steve Miller, Dr. Yi Yun and Dr. Ankush Biradar for training me to use various deposition and characterization equipments over the years. My fellow group mates Brian, Emma, Josh and Sean, I would like to thank them all for help and motivation. I would like to extend special thanks to Dr. Saquib Ahmed, Dr. Beda Mohanty, Chetan Tonde and Sankha Banerjee for helpful discussions, motivation and lot of fun during the long hours spent in the lab.

I would like to thank my committee members Prof. Adrian Mann, Prof. Leonard Feldman and Dr. Allan Bruce for spending their valuable time providing useful comments and constructive criticisms on my thesis work which helped me in improving my thesis.

I would like to thank all my teachers over the years who have had huge influence on me, especially my father Mr. Vijayakumar Gopalswamy and Prof. Sasi Kottayil for

inspiring me to pursue renewable energy. I would like to thank all my friends who have made the entire graduate school experience very memorable. I would also like to thank Prof. Lisa Klein and Ms. Phyllis Cassell for providing a wonderful atmosphere for graduate students in the materials sciences department.

I would like to specially thank my mother, who has been a huge inspiration to me in my life. Her motivation and kind words really helped me finish my thesis. Finally I would like to thank the almighty for unconditional love and blessings.

# Table of Contents

# List of Figures

# List of Tables

# CHAPTER 1

## 1. Introduction

### 1.1. Global electricity sector scenario

There are three major dynamics happening currently in the global electricity sector; first is the rapid growth in electricity consumption across the world especially in non-OECD countries, second is the 'greening' of world's electricity sector due to environmental concerns driven by governmental policy and improvements in technology and third is the technology developments in hydraulic fracturing of shale rock to produce abundant cheap natural gas particularly in North America. The above factors have contributed to the rapid growth of solar and wind power installations worldwide and will lead to tera-watt scale installations of renewable energy infrastructure in the future. They are described in detail below.

#### 1.1.1. Rapid growth in electricity sector

Let's look at the first feature, growth in the electricity sector. Worldwide electricity consumption in 2008 was estimated to be 19.1 trillion KWh and it is projected to increase by 85% to reach 35.2 trillion KWh in 2035 as shown in figure 1.1, according to US Energy Information Administration [1]. In OECD countries which have well established electricity infrastructure, the growth in electricity consumption is expected to increase on an average 1.7% per year or 46% overall from 2008 to 2035. In non-OECD

countries where the electricity infrastructure is getting expanded to meet the electricity demand, which is not yet met today, the electricity consumption is projected to increase 4.7% per year or overall 127% during this period. In China and India electricity consumption growth is going to be higher than the average in non-OECD countries at 5.% per year or overall 154% during this period. This large growth in demand for electric power coupled with improvements in technology will provide an opportunity for new energy generation technologies to be deployed at a large scale across the world.

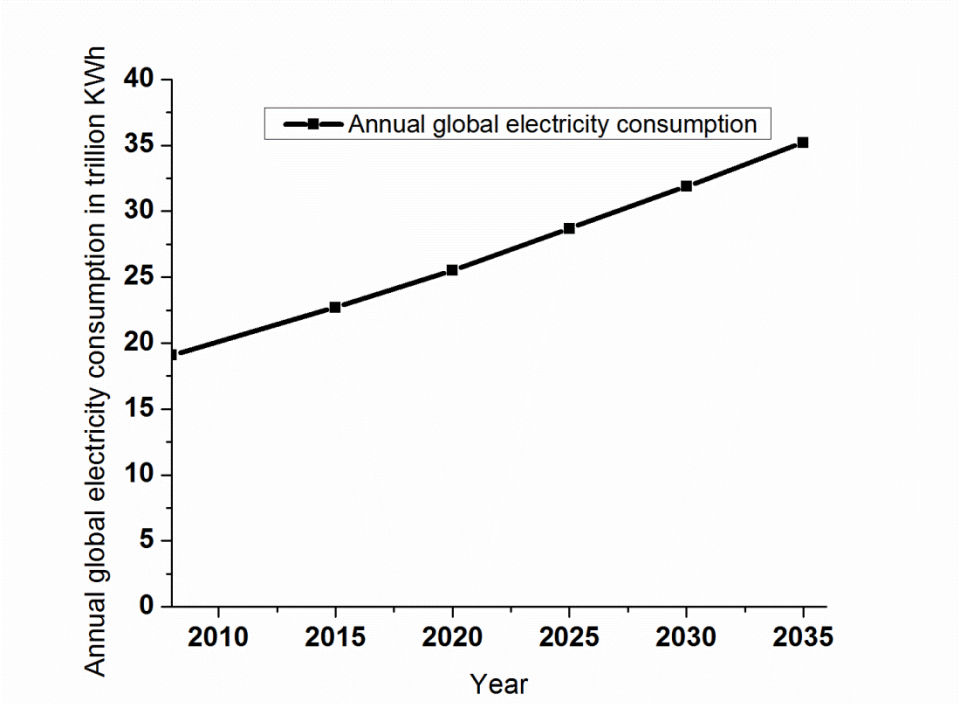


**Figure 1.1 Projected annual global electricity consumption in trillion KWh [1].**

### 1.1.2. 'Greening' of world's electricity infrastructure

Electricity sector is the largest polluter of global green house gas emissions, 26% of global [2] and one third of US [3] green house gas emission is due to electricity sector, so any rise in electricity consumption without clean energy technology deployment could lead to significant rise in green house gas emissions. In OECD countries, especially

European Union, Japan and United States substantial investments are being made every year to increase the contribution of renewable energy in the electric grid, with renewable energy contributing more than 50% of all new power plant installations in terms of MW capacity. In 2012 US installed a record 13,200 MW of wind power [4] and 3,300 MW of photovoltaic [5] as shown in table 1.1, representing nearly 53% [6] of all new total power plant installation in the country. European Union installed 11,895 MW of wind power and 16,750 MW of photovoltaic in 2012 representing 64% of all new power plant installations [7] as shown in table 1.1.

**Table 1.1 Wind, PV and Natural gas power plant installations measured in MW's in 2012 in European Union, USA and China.**

| Region | PV installed in 2012 (MW's) | Wind power installed in 2012 (MW's) | Natural gas power plants installed in 2012 (MW's) | Wind and PV as a % of new power plant installations in 2012 | Natural gas power plant as % of new power plant installations in 2012 |
|---|---|---|---|---|---|
| European Union | 16,750 | 11,895 | 10294 | 64% | 23% |
| USA | 3,300 | 13,200 | 8717 | 53% | 28% |
| China | 1,200 | 15,900 | 0 | 21.5% | - |

Non-OECD countries especially China and India, have also made significant investments in wind power installations with China being the largest and India being the 5$^{th}$ largest wind power installed countries in the world. As seen in table 1.1, about 21.5% of China's new power plant installation in 2012 is from PV and wind power [8].

Across the world PV and wind power deployments grew on an average 56% and 25% per year respectively during the 6 year period between 2006 to 2012 [9-11] outpacing all other new electricity infrastructure installations. 2012 was a record year for both wind and PV industry with 44,000 MW new wind power installations [10] and 32,000 MW of new PV plants were brought online across the world [11] as shown in table 1.2. These large scale PV and wind power deployments across the world are poised to accelerate in the coming years as they reach grid cost-parity at more parts of the world due to their falling costs and improvements in technology.

**Table 1.2 Renewable electricity sector installations worldwide.**

| Technology | MW's installed in 2012 | 6 year growth rate 2006 ~ 2012 (average per year) | Cumulative worldwide installations in MW's in the end of 2012 |
|---|---|---|---|
| Hydro Power* | 25,000* | 3% per year* | 980,000* |
| Wind Power | 44,000 | 25% per year | 280,000 |
| Photovoltaics | 31,000 | 56% per year | 100,000 |
| Ocean Power* | 257* | - | 524* |

* For hydro power and ocean power the data is until the end of year 2011, i.e. MW's installed is for the year 2011, the growth rate is for the period 2006 ~ 2011 and cumulative installations is until the end of 2011.

### 1.1.3. Abundant natural gas reserves

Natural gas powered thermal power plants have lower green gas emissions compared to coal powered thermal power plants. This environmental benefit combined

with the availability of abundant cheap natural gas reserves due to technology developments in hydraulic fracturing ("fracking") of shale rock formations have led to a rapid growth in natural gas based power plants. In 2012, 23% and 28% of name plate capacity for all new power plants in European Union and US were powered by natural gas as shown in table 1.1. In fact a large number of existing coal power plants are being switched to natural gas in the US [12] because of the low fuel costs. These new natural gas power plants could be made to increase or decrease power generation quite rapidly. Thus acting as reserves to deal with the rapid and unpredictable changes in electricity demand or changes in electricity generation due to intermittency associated with wind and solar energy [13]. So availability of large number of natural gas power plants as spinning reserves would help in increasing the penetration of solar and wind power technologies without affecting the reliability of the electric grid.

## 1.2. Photovoltaics

There is abundant solar energy irradiation hitting the surface of the planet all the time: about $1.7 \times 10^{11}$ MW [14]. If 30 seconds of the solar energy incident on the planet were completely captured that would be enough to meet the electricity requirements of the entire planet for a year. However the cost of solar energy generation has been high in the past; only recently has it has been reducing rapidly enough to bring it closer to grid parity. As of 2012, cost of electricity due to PV is at parity with the electric grid in 105 countries as shown in figure 1.2. It is forecasted that by 2020, about 98% of world's population will have solar power at the same price as electric grid [15].

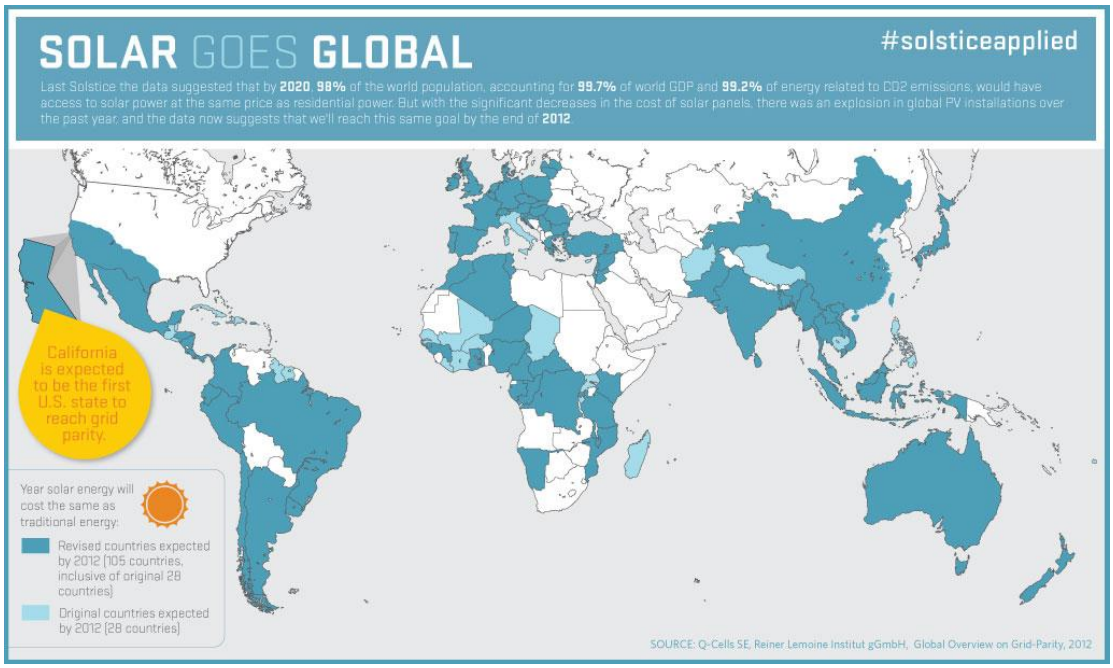


**Figure 1.2 Map of PV grid parity as of 2012 [15].**

## 1.3 Challenges with PV

### 1.3.1 Low power conversion efficiency

One of the biggest challenges with PV has been that large land area that is required to generate the desired energy using present technologies. This is because most of the commercially available silicon and thin film solar cells are 12% ~ 18% efficiency. The theoretical maximum efficiency for silicon solar cells is calculated to be about 33% but the practical maximum efficiency is around 25% [16], taking into account the losses due to reflection and absorption at the front glass and encapsulation layers. So if 20% of the projected global electricity demand in 2035 is met by photovoltaic devices, contributing 7 trillion KWh, that would entail a global installation of 3,850,000 MW or 3.85 TW (Tera Watts), about 38X the present day installed capacity, (considering average solar irradiation of 5000 Wh/sq.m per day). PV installations have been growing at 56%

per year average for the last 6 years [9,11] and with an estimated solar module manufacturing infrastructure of about 70 GW per year [17] it is possible to have a couple of TW scale installation in less than 20 years because of the decreasing solar manufacturing costs. However the corresponding land area required for 3.85 TW will be approximately 11.5 million hectares with the present generation of silicon solar cells having circa 15% efficiency. To put the land requirement in perspective, 11.5 million hectares is about 7.2% of the global land area used for cultivating maize (corn) [18]. Such high land requirement would pose significant challenges for Asia, Western Europe and parts of Africa and South America, which are some of the most densely populated regions in the world.

### 1.3.2 High installed cost

Though the price of PV devices have reduced rapidly in the last decade and a half, it is still high enough necessitating significant subsidies. About 50% ~ 65% of the total cost per peak watt ($/$W_{peak}$) of installed photovoltaic systems is associated with balance of systems (BOS) and labor [17]. However it is very hard to find a technology solution to reduce the costs in BOS.

If the solar module efficiency could be improved without significant cost increase then the cost per watt of installed photovoltaic systems could be brought down through reduction in balance of system costs. Also it could drastically reduce the land requirement for deploying solar panels in densely populated areas. So a pathway to higher module efficiency at a reasonable cost increase is essential if solar energy is to play a significant part of the global electricity generation mix.

## 1.4 Basic Principle of solar cells

The heart of a solar cell is the p-n junction. If both 'p-type' and 'n-type' semiconductors are of the same material it is called homo-junction solar cell (example - conventional silicon solar cells) or if it is made up of different materials it is called hetero-junction solar cell (example - thin film solar cells made up of Cadmium Telluride or Dye Sensitized Solar cells). When the 'p-type' and 'n-type' junctions are brought together, the Fermi levels on either side align together causing the valence and conduction bands to bend as shown schematically in figure 1.3.

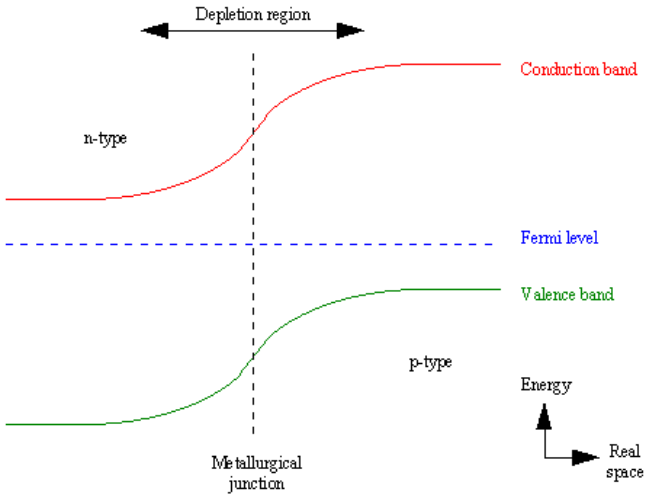


**Figure 1.3 p-n junction band-bending. [19]**

This region where the conduction and valence bands are bent is referred to as the depletion region. These bent bands give rise to an electric field in the depletion region. When a photon of energy greater than the band gap of the semiconductor is incident on the solar cell it is absorbed by the device as shown in figure 1.4. The absorbed photon gives rise to an electron/hole pair, called an exciton. In inorganic semiconductors the exciton binding energy is of the order of milli electron volts (meV) but for organic

semiconductors the exciton binding energy is of the order of 10's ~ 100's of meV. Since excitonic binding energy is less in inorganic semiconductors the thermal vibrations in the lattice provides enough energy to overcome the binding energy of the exciton in order to split them into electrons and holes. The minority charge carriers then diffuse to the depletion region where they get transported by drift due to electric field to the respective contacts. In organic semiconductors because of the high exciton binding energy the exciton gets separated into electrons and holes only at the electron donor / electron acceptor interface (analogous to p-n junction interface) due to the built in electric field. So excitons which diffuse to the depletion region before recombination, get separated into an electron and hole and they are transported by the electric field to the respective electron donor and electron acceptor materials. From there these charges are collected through the metal contacts in order to flow through an external load. This is the origin of the solar cell's photocurrent and is shown in Figure 1.4.

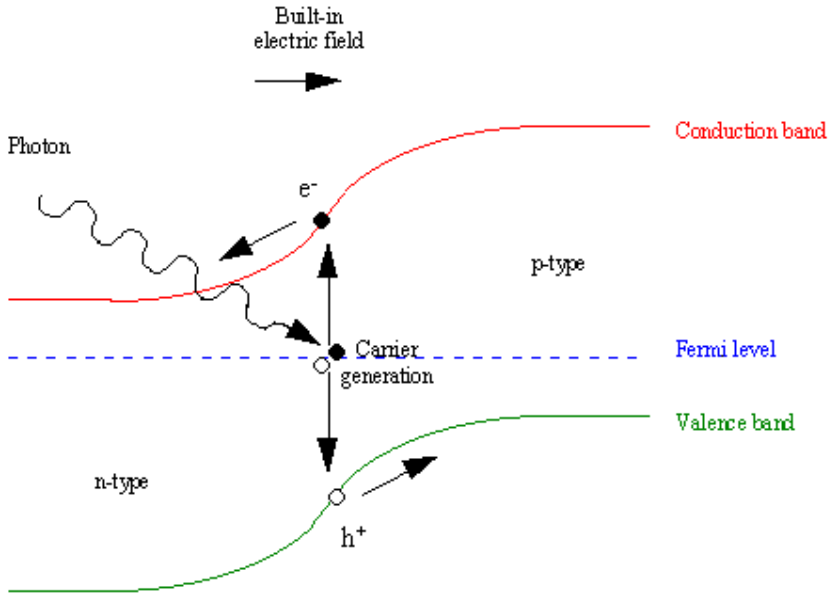


**Figure 1.4 Principle of a photovoltaic device. [19]**

## 1.5 Photovoltaic Technologies

### 1.5.1 Silicon solar cells

A schematic of a conventional silicon solar cell is shown in figure 1.5. A p-n homo-junction is formed by doping the p-type silicon wafer of 200 µm thickness with phosphorous to form 0.5 µm thick n-type region. Aluminum and silver are the most commonly used back and front metal contacts for the silicon solar cell. These metals are chosen so as to provide an ohmic contact with the silicon. In order to reduce the contact resistance, regions of silicon close to the back and front contacts are heavily doped. These regions are called BSF (back surface field near the back contact) and FSF (front surface field near the front contact). Also the front surface of the silicon solar cell is often textured by commercial etching solvents and coated with a thin layer of antireflection coating (for example, silicon nitride, SiNx) in order to increase the light absorption of the device.

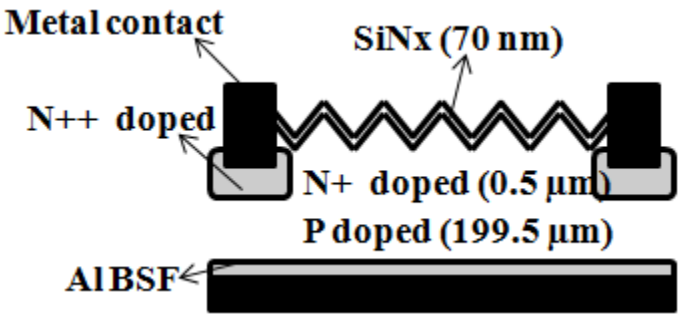


**Figure 1.5 Schematic cross-section of a conventional silicon solar cell.**

Figure 1.6 is an illustration of a fully assembled solar cell device. EVA (Ethylene Vinyl Acetate) is used as an encapsulation material protecting the semiconductor device from moisture and mechanical shock. Low iron glass and fluoropolys act as the front and

back sheets providing mechanical support and electrical insulation to the device. They are laminated to the silicon solar cell with a 0.4 µm thick EVA layer in between them [20].

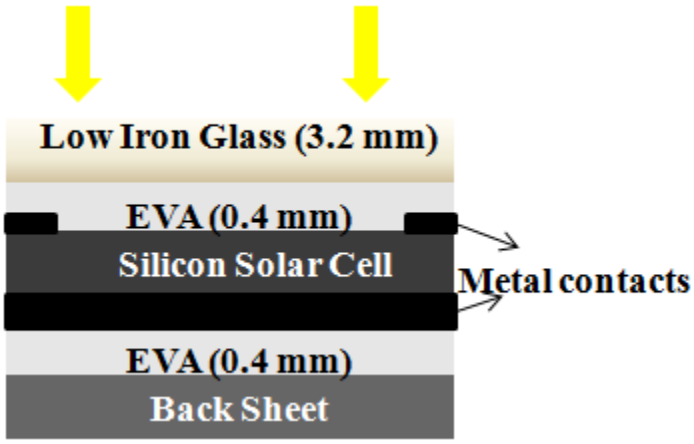


**Figure 1.6 Cartoon of an assembled silicon solar cell.**

### 1.5.2 Dye-sensitized solar cells (DSSC)

In dye-sensitized solar cells (DSSC), the light absorption is done by an organic or an inorganic dye and charge transport is through a semiconductor matrix and a redox electrolyte. Since light absorption and charge transport is done by different material systems it is possible to engineer these systems individually. Since fabrication of DSSC's require only organic dyes, solution deposited semiconductor matrix and liquid electrolytes, it is possible to make large volumes of inexpensive solar cell devices.

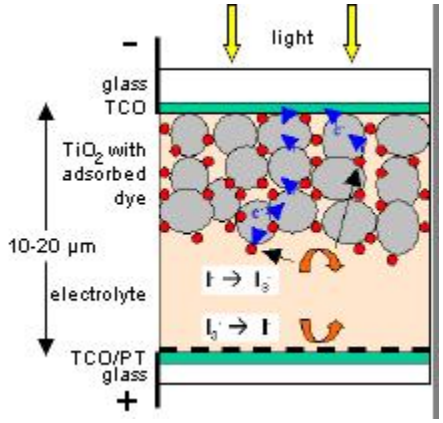


**Figure 1.7 Schematic of a Dye-sensitized solar cell. [21]**

A schematic of a DSSC is shown in figure 1.7 [21]. It consists of a mesoporous titanium dioxide ($TiO_2$) layer of 10-12 μm thickness with a particle size of 10 ~ 30 nm. The film porosity is typically around 50%. The $TiO_2$ is adsorbed with a mono layer of organic dye, typically a Ruthenium complex N719. The $TiO_2$ layer is coated on a transparent conducting oxide (TCO) on a glass substrate. Photon absorption of the dye results in the injection of an electron into the conduction band of the $TiO_2$, leaving the dye in an oxidized state. The dye is restored to its original electronic configuration by electron transfer from the electrolyte, typically an iodide/tri-iodide redox couple. The electrolyte in turn is regenerated at the platinum cathode. The basic electron transfer processes in typical DSSC is shown in figure 1.8.

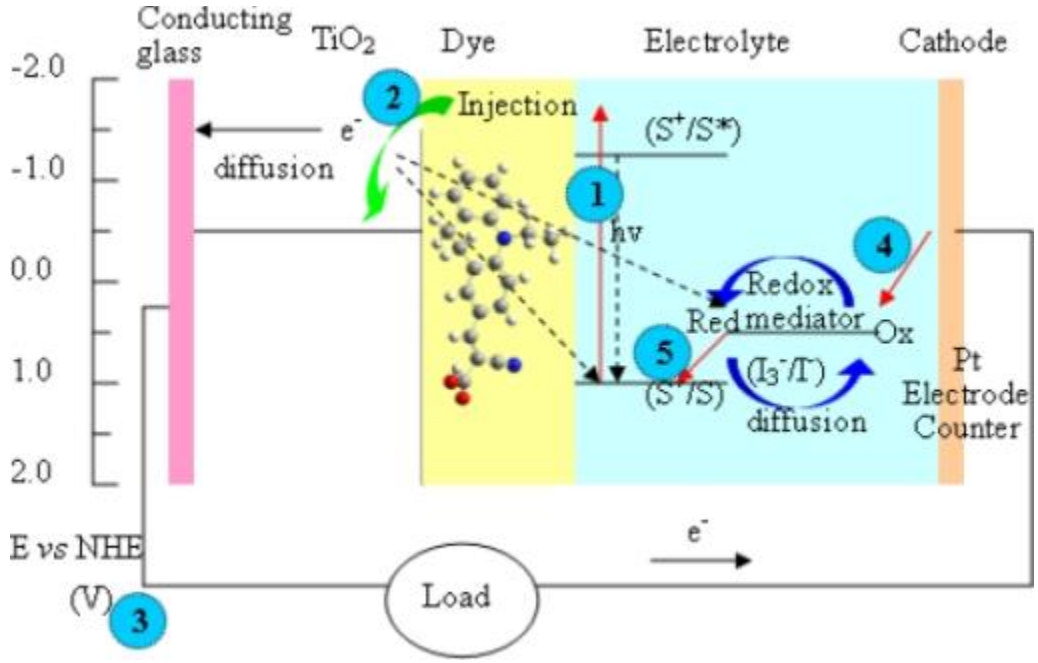


**Figure 1.8 Electron transfer process in a typical Dye-sensitized solar cell. [22]**

### 1.5.3 Other Photovoltaic technologies

There are various other PV device architectures utilizing a combination of organic, inorganic semiconductors and quantum dots. Organic solar cells operation is

similar to inorganic solar cell devices, they have an electron-donor and electron-acceptor junction analogous to p-n junction in inorganic solar cells. Semiconductor quantum dots are also used in solar cells as light absorption material and the generated charges are usually transported through other materials. One of the examples of quantum dots in solar cells is DSSC's sensitized with quantum dots rather than organic dyes [23]. Various other architectures exist to enhance the light absorption and reduce the amount of semiconductor material in solar cell devices but all devices work on a similar principle as a p-n junction device for the photovoltaic action to occur.

### 1.6 Efficiency limit of PV devices

Present generation of silicon solar cells have reached a laboratory efficiency of 24.7% [24] and it has a theoretical maximum efficiency of 34%. The efficiency of PV devices are limited primarily by three intrinsic losses.

1. All photons having energies less than the band gap of the solar cell are not absorbed by the semiconductor and pass through the device without contributing to the photocurrent as shown in figure 1.9.
2. All photons having energies more than the band gap of the solar cell lose their excess energy as phonons, contributing to lattice vibrations and heating up the device as shown in figure 1.9. This loss is known as thermalization loss.
3. Radiative recombination because every biased semiconductor also acts as a light emitting source.

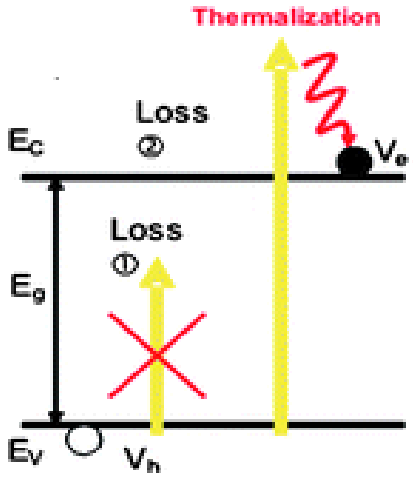


**Figure 1.9 Fundamental losses in a photovoltaic device. [25]**

In 1961, Shockley and Queisser quantified the maximum efficiency of a PV device taking into account thermalization loss, non-absorption of photons below the band gap and radiative recombination in the solar cell [26]. This is now known as Shockley - Queisser limit and figure 1.10 shows the Shockley - Queisser limit for a single junction solar cell and the maximum possible efficiency is about 34%.

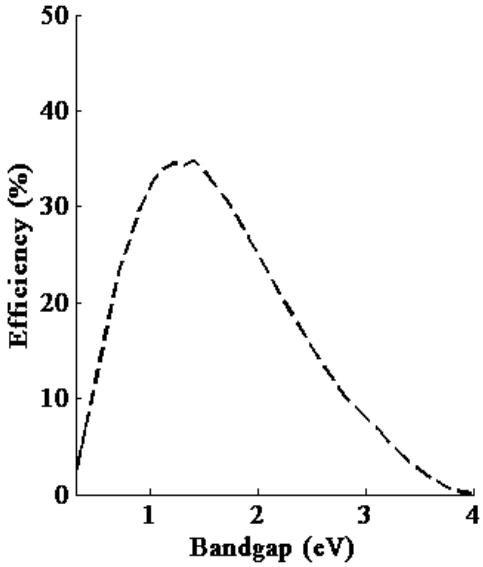


**Figure 1.10 Maximum possible theoretical conversion efficiencies for single junction solar cell based on Shockley and Queisser limit under AM 1.5 solar spectrum.**

## 1.7 Pathways to higher efficiency PV devices

Higher power conversion efficiency PV devices are possible by efficient broadband absorption of solar insolation [27]. Various architectures have been proposed for this purpose namely multi-junction solar cells [28-37], photon up-conversion and multiple exciton generation in solar cells [38-41].

### 1.7.1 Multi-junction PV devices (Tandem solar cells)

Multi-junction PV devices have more than one p-n junction with each junction stacked on below the other, such that the band gaps of the semiconductor junctions are placed at decreasing order of magnitudes with the highest band gap at the top and the lowest band gap at the bottom. A cartoon of a multi-junction device is shown in figure 1.11.

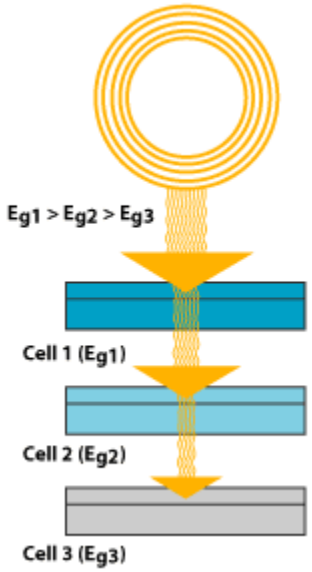


**Figure 1.11 Multi-junction PV device architecture. [42]**

As the light passes through the device, high energy photons are first absorbed at the high band gap junction. Photons which are transparent to the first p-n junction are absorbed at the subsequent lower band gap junctions at the bottom. Thus more photons are captured efficiently in a multi-junction PV device leading to higher device efficiencies as shown in figure 1.12. The p-n junctions could either be electrically connected together in a series circuit through a tunnel junction with 2 electrical terminals (1 positive and 1 negative contact) [28-30] as shown in figure 1.13 or it could be optically coupled together with the p-n junctions placed as a mechanical stack [31-37] as shown in figure 1.14.

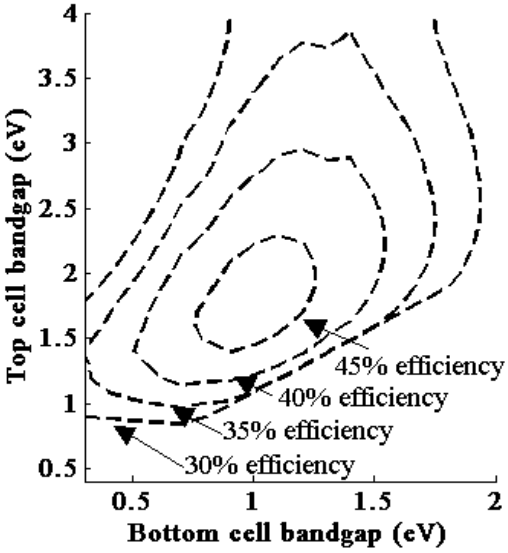


**Figure 1.12 Theoretical conversion efficiencies based on Shockley and Queisser limit for two junction (mechanical stack) solar cells under AM 1.5 solar spectrum.**

#### *1.7.1.1 Tunnel junction (2 terminal) based multi-junction PV devices*

An impressive 44.4% power conversion efficiency record was reported by Sharp Inc. for multi-junction (2 terminal) solar cell with InGaP / GaAs / InGaAs architecture

with light concentration of 302x [43]. Sharp's cell also had the record of highest power conversion efficiency at AM 1.5 solar spectrum without light concentration at 37.7% before it was broken by Spectrolab's device which had 37.8% efficiency [46].

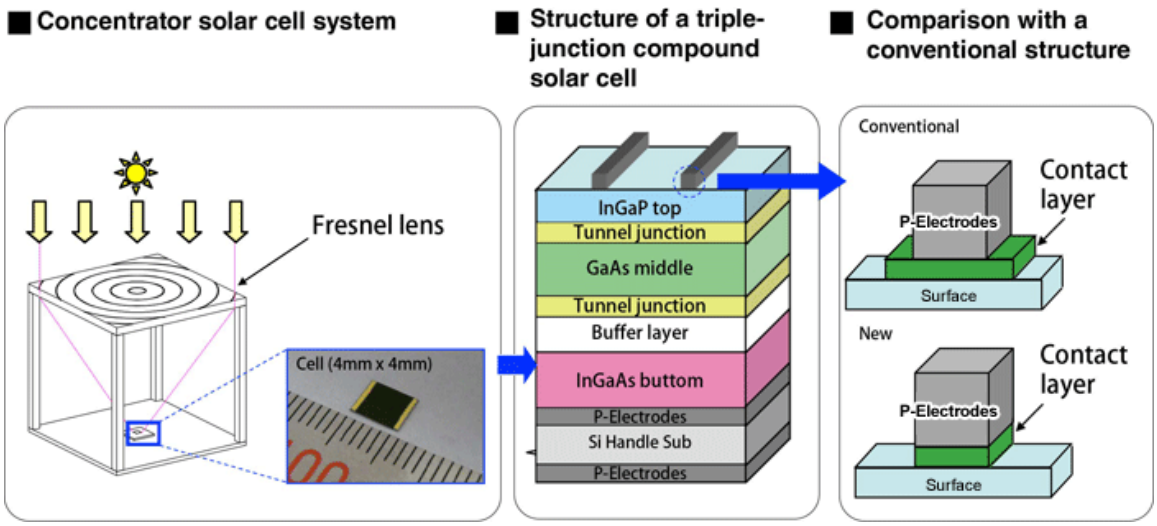


**Figure 1.13 A cartoon of the Sharp's record 44.4% efficiency multi-junction PV device with light concentration using Fresnel lens. [43]**

Many companies have set up shop for commercial deployments of multi-junction solar cells with light concentration. However to manufacture them at scale necessary to compete with existing single junction solar cell manufacturers in terms of $\$/W_{peak}$ seems to be difficult. This is because tunnel junction based multi-junction devices are typically grown using MOCVD reactors which because of their low deposition rate leads to lower throughput increasing the $\$/W_{peak}$. So the high cost of manufacturing multi-junction solar cells have led to the closures of many companies notably Soliant, Sol-Focus, Energy Innovations and Green Volts [45]. However much effort also has been put in the recent years to develop deposition equipment for scale large production of 2 terminal multi-

junction PV devices and companies like Emcore, Solar-junction, Sharp and Spectra-watt are working to improve efficiencies and lowering manufacturing costs to commercialize these devices. So it remains to be seen whether this technology gets commercialized and reaches wide spread acceptance for terrestrial applications. Nevertheless multi-junction solar cells are used extensively in aerospace applications where high power conversion efficiency and low weight of a solar cell are the most important criteria.

#### *1.7.1.2 Mechanical stack like tandem multi-junction PV devices*

A tandem structure in a simple mechanical (stack like) arrangement of solar cells is promising because of its lower complexity in assembling multi-junction solar cells. Especially if it can utilize the existing multi gigawatt manufacturing capacity of silicon solar cells as one of the device thereby making it easier for wide spread adoption in the market place. Figure 1.14. is a schematic of mechanical tandem multi-junction device. Figure 1.10 and 1.12 shows the theoretical power conversion efficiencies for single and two junction (mechanical stack) solar cells based on Shockley-Queisser's calculations in their seminal paper [26] for AM 1.5 spectrum. Tandem solar cells with GaAs / CISe [31 - 34] and a-Si / CISe [35] structure were first reported two decades ago with enhancement in relative efficiencies of ~ 20% compared to individual cell efficiencies. In the recent years there have been renewed efforts to study the efficiency enhancement and feasibility of tandem solar cells using CuGaSe / CuInSe [45 - 48], Dye Sensitized Solar Cell (DSSC) / CISe [36 - 37], DSSC / DSSC [49], GaAs / Ge [50-51], and organic solar cell / CIGS [52] tandem architecture. However the increase in efficiency was more modest for devices having CuGaSe devices as high band gap top solar cells because of their lower

efficiency [53] and low light transmission. But a recent theoretical study on organic solar cell / CIGS tandem architecture has shown potential efficiency improvement of over 5% [52] is feasible.

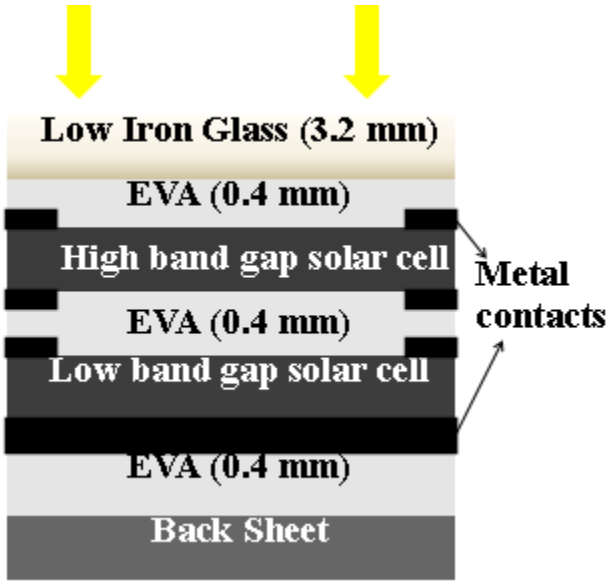


**Figure 1.14 A schematic of tandem (mechanical stack like) multi-junction PV device.**

### 1.7.2 Photon up-conversion, down conversion and multiple exciton generation

Photon up-conversion and down-conversion in PV devices could dramatically improve the power conversion efficiency. In up - conversion two or more photons with energy $1/2E_g \leq h\nu < E_g$ (where $E_g$ is the semiconductor band gap) create one photon with $h\nu \geq E_g$, while in down-conversion one photon with energy $h\nu \geq nE_g$, yields two or more photons with energy $h\nu \geq E_g$. Photon up-conversion and down conversion have higher theoretical efficiencies [38-41]. Though devices utilizing these phenomenon have been

reported in the literature but their power conversion efficiencies have so far been very low. More work is required to study these fundamental properties and demonstrating these phenomena in a wide range of materials. So making efficient devices using these phenomenon though theoretically feasible, will require more effort to make efficient devices with an eye toward the manufacturing scale.

## 1.8 Characterization Techniques

Electrical characterization techniques which are used to examine the PV devices are I-V (current - voltage) curves, IPCE (Incident Photon Conversion Efficiency) and in the case of DSSC's electrochemical impedance spectroscopy (EIS) is used. In the following sections these characterization methods which are used extensively in this thesis for data analysis are reviewed.

### 1.8.1 I-V (Current - Voltage) Curves

The light spectrum used to characterize the PV device is calibrated for AM 1.5 G (global) spectrum. The spectrum resembles a blackbody radiation at a temperature of 5760K with absorption bands of the various atmospheric gasses due to ozone, water vapor, carbon dioxide and etc. The spectrum is normalized so that the integrated irradiance is 1000 $W/m^2$.

The current flowing through the PV device incident with this spectrum is measured at various voltages from short-circuit condition (0 Volts) to open circuit condition (0 Amps), the plot of which is shown in figure 1.15. The maximum current generated by the device is at short circuit condition and is noted as Jsc. The maximum

voltage is at the region in the curve where the total current flowing through the device is 0 Amps and is noted as Voc. Pin is the incident power and FF is the "fill factor" which takes values from 0 to 1, and is defined by the ratio of the maximum power (Pmax) of the PV device divided by Voc and Jsc. The maximum power is obtained at the point where the product of the current and voltage of the device is maximum.

$$\eta = \frac{\text{Jsc} \times \text{Voc} \times \text{FF}}{\text{Pin}}$$

$$\text{FF} = \frac{\text{Pmax}}{\text{Jsc} \times \text{Voc}}$$

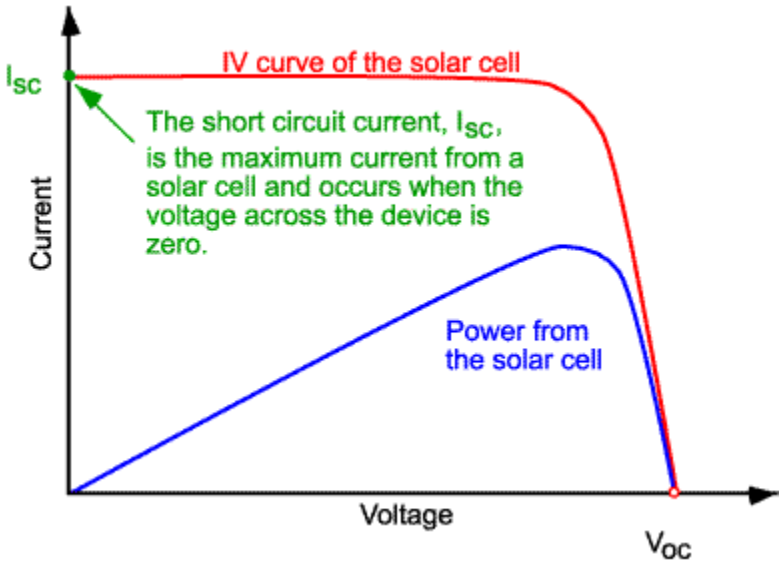


**Figure 1.15 Current - Voltage curve of a PV device. [54]**

### 1.6.2 IPCE (Incident Photon Conversion Efficiency)

External quantum efficiency (EQE) also known as the incident photon to current conversion efficiency (IPCE) provides information about the efficiency of the PV device

in converting incident light to electrons at each specific wavelength. It is normally a plot of wavelength of operation of the device on the x-axis and photon to electron conversion efficiency on y-axis.

$$IPCE = \frac{Jsc\ (\lambda)}{e\varphi(\lambda)} = 1240\ \frac{Jsc(\lambda)[A\ cm-2]}{\lambda\ [nm]Pin(\lambda)[W\ cm-2]}$$

where *e* is the elementary charge. IPCE values provide more information to quantify the loss mechanisms in the PV device.

### 1.8.3 Electrochemical Impedance Spectroscopy

Electrochemical impedance spectroscopy (EIS) is extensively used to characterize DSSC's. It provides information about the electrical impedance due to various components of the device, thereby providing insights to develop efficient device architectures. In this technique impedance of the device is measured at various operating frequencies and since each component of the device has a unique frequency response, impedance of each component can sometimes then be isolated. Using EIS, following parameters can be obtained for DSSC's: series resistance of the device, impedance due to charge transport at the electrolyte / platinum electrode interface, charge transport impedance at the $TiO_2$ / dye / electrolyte interface and the charge transport impedance in electrolyte.

## 1.9 Simulation Software

As a part of this research work detailed simulation models of various PV devices were developed to quantify their optical absorption and electronic performance. In this

section software used for modeling and simulation and their underlying equations are described.

### 1.9.1 Electronic modeling - WxAMPS

The electronic simulations of the modeled devices were performed using WxAMPS developed at University of Illinois [55]. WxAMPS is a tool for one-dimensional numerical simulation of opto-electronic devices. It is an updated version of AMPS 1-D developed by Prof. Fonash at Pennsylvania State University [56-57]. The program works by solving three coupled non-linear differential equations which captures the electron and hole transport properties in a semiconductor, i.e. Poisson's equation, the continuity equation for free holes, and the continuity equation for free electrons.

Solution to Poisson's equation provides information about electric field at any point in the device,

$$\frac{d}{dx}\left(-\varepsilon(x)\frac{d\Psi'}{dx}\right) = q.[p(x) - n(x) + ND(x) - NA(x) + pt(x) - nt(x)]$$

Solution to continuity equation provides information about electric current at any point in the device,

$$\frac{1}{q}\left(\frac{dJp}{dx}\right) = G(x) - R(x)$$

$$\frac{1}{q}\left(\frac{dJn}{dx}\right) = -G(x) + R(x)$$

Where $\varepsilon$ is permittivity, $\Psi'$ is the electrostatic potential, q is the magnitude of the charge, n and p are free electron and free hole concentrations, nt and pt are trapped electron and trapped hole concentrations, ND and NA are ionized donor and ionized

acceptor concentrations, Jp and Jn are hole and electron currents, R is the net recombination and G is the generation of charge carriers.

WxAMPS utilizes finite element method (FEM) to form a mesh along which the above coupled differential equations are solved by computing electric fields, electron and hole currents at the mesh boundary conditions. The advantages of WxAMPS is its ability to model defect energy level distributions (surface recombination, mid gap, band tail defects) and especially its ability to analyze transport in devices under voltage bias and light bias. It allows customization of light spectrum and in this study AM 1.5 G (Air Mass 1.5 Global) a standard spectrum used for testing solar cells is used. Light absorption in the semiconductor is modeled by Beer-Lambert's law.

### 1.9.2 Optical modeling - Lumerical & Matlab

Optical modeling and simulation of the PV devices was done to quantify the light absorption at each layer of the device. The simulation models of the PV device with and without texturing were developed. The simulation model of non-textured device was done in Matlab as thin solid films [58-59] using equations reported below and for textured device the simulation model was developed by finite-difference time-domain (FDTD) method using Lumerical.

$$R\ cell = \left|\frac{no\ m11 + no\ nsemi\ m12 - m21 - nsemi\ m22}{no\ m11 + no\ nsemi\ m12 + m21 + nsemi\ m22}\right|^2$$

$$\begin{pmatrix} m11 & m12 \\ m21 & m22 \end{pmatrix} = \begin{pmatrix} \cos \delta antiref & i \sin \dfrac{\delta antiref}{nantiref} \\ i\, nantiref \times \sin \delta antiref & \cos \delta antiref \end{pmatrix}$$

$$n = ni - iki$$

$$\delta\, SiNx = \frac{2\,\pi\, d}{\lambda}\, nSiNx$$

Where R cell is the reflection at the cell, encapsulation or air, antireflection coating interface. $n_o$, $n_{antiref}$ and $n_{semi}$ are the complex refractive indices of the incident medium (encapsulation or air), antireflection coating and semiconductor. Light absorption in the material is given the expression below.

$$A = 1 - \ e^{(-\alpha\, d)}$$

$$\alpha = \frac{4\,\pi\, k}{\lambda}$$

Where A is the light absorption in the material, d is the thickness and $k$ is the extinction coefficient of the material.

## 1.10 Goal of the present research

The main goal of the present research is to quantify the extrinsic optical and electrical losses in a mechanical tandem device in order to design high efficiency PV devices. In this research detailed electrical and optical simulation models of silicon, GaAs, and Ge solar cells were developed. Since silicon solar cells are widely available

commercially and have an established multi-giga watt manufacturing infrastructure, they were selected as one of the candidate materials for the tandem device. Two different tandem solar cell device configurations were analyzed with silicon as top cell in Si / Ge tandem device and silicon as a bottom cell in GaAs / Si tandem device architecture. The simulations of the tandem devices were compared with experimental device performances reported in the literature.

Ge which has a band gap of 0.67 eV [60] is selected as a candidate for the bottom cell in Si / Ge tandem device so that the tandem device could capture wavelengths starting from U-V to far infra-red spectrum of the incident light. The intrinsic efficiency limit of Si / Ge device is 38% which is lower than the intrinsic efficiency of GaAs / Si device, nevertheless the knowledge of the extrinsic loss mechanisms for a tandem device designed to absorb wavelengths from 300 nm - 1907 nm would be useful in designing future broadband solar cells.

GaAs has a band gap of 1.43 eV [60] and the intrinsic efficiency limits for GaAs / Si and GaAs / Si is 43% compared to standalone GaAs cell which has an intrinsic efficiency limit of 34%. Higher intrinsic efficiencies of close to 47% are possible in tandem solar cells with top cell band gaps of 1.7 eV ~ 1.9 eV but in this work the focus is to understand the extrinsic losses in tandem devices so GaAs whose optical and transport properties are well understood is used as a top solar cell.

The other part of the research focused on developing high band gap PV devices as other candidate materials for the top solar cell with silicon as the bottom solar cell. Two candidate devices were selected for this purpose because of their advantages of low cost and flexibility in manufacturing. DSSC's (Dye Sensitized Solar Cells) were considered as

a candidate device because the conventional dye N719 used in the DSSC has absorption only until 700 nm corresponding to > 1.7 eV. DSSC's have low processing and material cost except for ITO (Indium doped Tin Oxide) which is used as the transparent conducting oxide (TCO). So in this research an alternative to ITO was explored and Stainless Steel (SS) meshes based DSSC's were developed. Their photovoltaic device performance was characterized and compared with ITO based DSSC devices. The other candidate material for high band gap PV device studied in this thesis was copper zinc tin sulfide, $Cu_2ZnSnS_4$ (CZTS). CZTS is a promising solar light absorber with all of its constituent elements being abundant, low cost (similar to silicon) and a direct band gap of 1.5 eV [61]. Coatings of CZTS were deposited onto molybdenum and glass substrates and characterized.

### 1.11 Break down of thesis work

Chapter 2 focuses on flexible stainless substrates (SS) used to make DSSC's. SS meshes were used as substrates for the DSSC's with $TiO_2$ spray coated on to the substrates. The DSSC's made using SS meshes were quantified using impedance spectroscopy, current - voltage curves, and through optical and electron micro-graphs. SS mesh based devices had lower open circuit voltage and higher electrical impedance at SS / $TiO_2$ / dye interface. The causes for this poor photovoltaic performance and high electrical impedance were probed and solution was found to lower impedance. Finally efficient DSSC's were demonstrated using SS meshes.

Chapter 3 focuses on deposition and characterization of CZTS. Solution of CZTS precursors were dissolved on to an organic solvent and were spin coated / blade coated on to molybdenum and glass substrates. The deposited coatings were annealed in nitrogen

atmosphere. The annealed coatings were characterized for their chemistry, crystal structure and optical properties.

Chapter 4 describes the simulation model of Si / Ge mechanical tandem solar cell device. The simulation model was used to quantify the various electrical and optical losses in standalone silicon and germanium devices and also in the Si / Ge tandem device. Explanations are also provided about the data used to build the simulation models. The simulated Si, Ge and Si / Ge device performances were compared with experimental efficiencies reported in the literature. Future efficiency improvements possible in the Si / Ge device architecture is also suggested.

Chapter 5 describes the simulation model of GaAs / Si mechanical tandem solar cell device. Detailed analysis was performed to quantify the electrical and optical losses in this device architecture. Future efficiency improvements possible in this architecture are also suggested.

Chapter 6 quantifies the losses in present state of the art high band gap solar cells and describes the tandem efficiencies possible with present generation of high band gap solar cells including DSSC and CZTS. Also, the improvement in electrical performance necessary for future high band gap solar cells is discussed.

Chapter 7 provides concluding remarks and future outlooks and projects to carry on the work presented in this thesis.

# CHAPTER 2

## 2. Flexible Stainless Steel Mesh Electrodes for Dye Sensitized Solar Cells

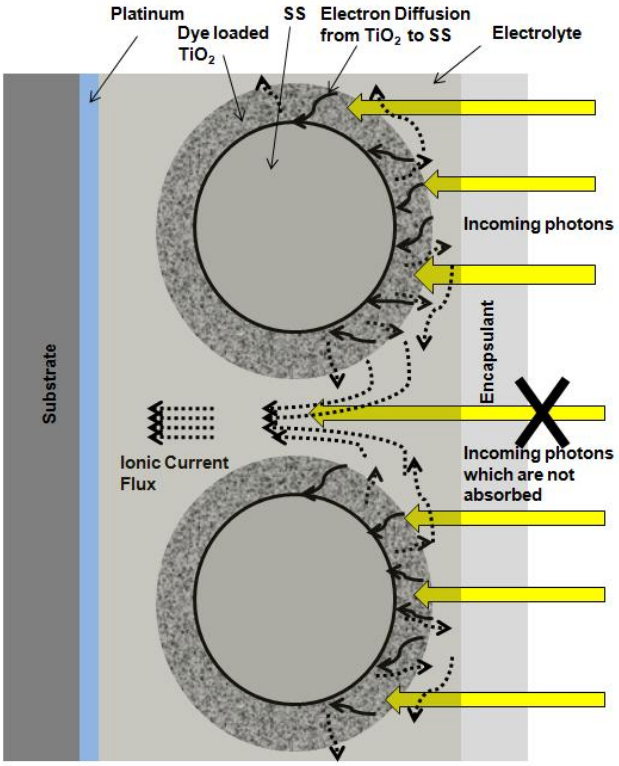


### 2.1 Background and Motivation for work

Dye sensitized solar cells (DSSC) are typically sensitized with N719 dye which absorbs light from UV to 700 nm wavelength corresponding to 1.7 eV band gap. Hence DSSC's sensitized with N719 or other wide band gap dyes forms a promising candidate for top cell with Si as the bottom cell in a mechanical tandem configuration.

DSSC's are beginning to enter large scale commercial production [62] and so significant effort has been put towards developing roll-to-roll manufacturing techniques to bring device costs down. However, titania coatings deposited on currently available flexible transparent conductor oxide (TCO) substrates (e.g. ITO/PET sheet) cannot be sintered at high enough temperatures due to heat resistance limits of the plastic, which leads to poor interconnection or bonding of titania particles. In order to circumvent this problem, reactive chemical sintering [63, 64], high pressure sintering [65, 66] and electrophoresis deposition [67, 68] have been suggested but each of these options might also have expensive commercialization paths. Moreover, the price of PET/ITO substrate has gone up over 250% [69] in the last 10 years making it an expensive material in the manufacture of solar cells.

In order to reduce the materials cost and to widen the application of DSSC, Lund et al. [70] studied the stability of industrial sheet metals in the presence of iodide / tri-iodide electrolyte and concluded that stainless steel and carbon steel are stable in the presence of ionic electrolyte and used these substrates with Pt coating as counter electrodes in DSSC with 3.6% and 3.1% efficiency respectively. Kang et al. [71-75] reported stainless steel (SS) sheets sputtered with ITO and $SiO_x$ layers as substrates for photo-electrodes in DSSC with an efficiency of 4.2% for a 0.2 $cm^2$ active area device under 1sun. Vacuum deposited $SiO_x$ layers were added to protect SS sheet from oxidation during high temperature sintering process and the expensive ITO layer was used to improve the conductivity since $SiO_x$ is an insulator. Due to opacity of SS photo-electrodes, TCO coated with a thin layer of Pt was used as the counter electrode to allow light penetration into the device, making a back-side-illuminated architecture.

In order to eliminate light absorption at Pt counter electrodes in a back-lit geometry and to overcome the opacity of SS sheet photo-electrode, a front-illuminated SS mesh architecture was proposed by Zou et al. in [76]. A 120-count SS mesh coated with titania acts as photo-electrode with a best cell efficiency of 1.49% was reported. Huang et al [77] reported a best cell efficiency of 1.51% for a photo-anode made of 500-count SS mesh coated with titania. A higher efficiency of 2.8% was also reported in [78] for a 500-count SS mesh photo-anode having a 2 layered coating, a lower titania colloid layer with small quantities of MgO reportedly to passivate the surface and a top layer of electrospun titania fibers to enhance light harvesting.

An illustration of SS mesh electrodes for DSSC is shown in figure 2.1, where the SS mesh is coated with $TiO_2$ adsorbed by Ru dye which acts as photo electrode and counter electrode is TCO coated with Pt. The excited electron from $TiO_2$ gets transported to the external circuit through SS meshes and the oxidized dye is regenerated by the electrolyte which transports the ions to the Pt electrode through the mesh openings. Some of the incoming light is lost, depending on the fractional area of mesh opening.

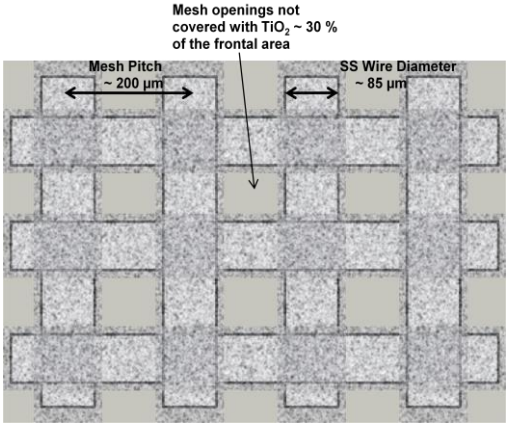


(a)

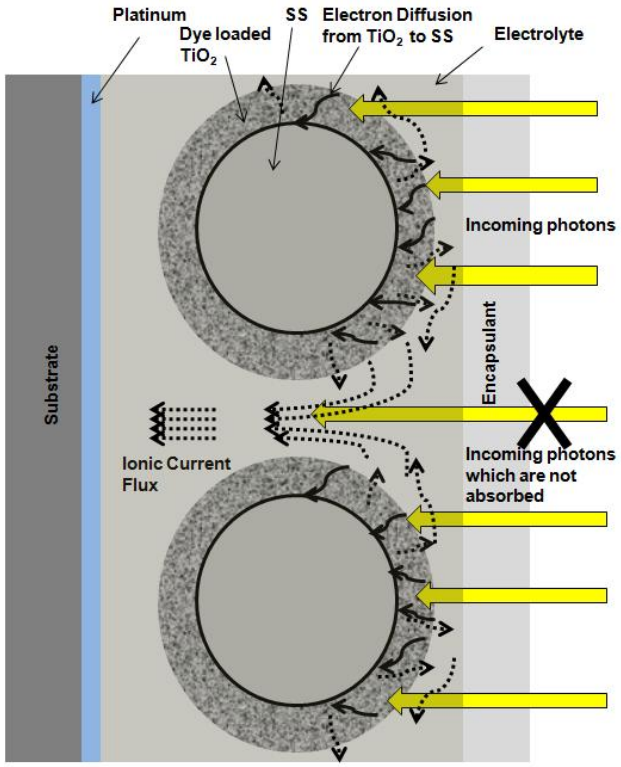


(b)

**Figure 2.1 Illustration of Dye Solar Cells with Stainless Steel mesh electrodes a) Front view showing mesh open area with schematic coverage of SS wires by sintered titania material, b) Cross section showing conduction pathways (small solid arrows give electron conduction pathways (small solid arrows give electron conduction within the titania, and longer dashed arrows give the counterbalancing electrolyte ion flows).**

In the present work, I extended the SS mesh electrode concept and examined device performance using optical measurements and electrical impedance spectroscopy. Bare SS mesh substrates oxidize during the sintering of titania particles thereby affecting the transport and interface resistances of the device, which were quantified through

electrical and optical measurements. In order to protect the SS electrodes from being oxidized, a thin non-porous titania layer was coated on top of SS mesh. These electrodes were then analyzed and their performances were compared with the FTO electrodes. The effects of mesh opening size and microstructure on the performance of the device were analyzed through SEM and impedance spectroscopy to correlate the performance of the electrodes and to suggest new design strategies.

## 2.2 Experimental

The SS meshes used in the experiments were 120-count type 304 SS mesh obtained from TWP Inc. SS meshes used were first washed in soap, and then ultra-sonicated for a few minutes in ethanol and acetone separately. The sonicated meshes were then dried for 10 minutes at 150$^{o}$C before being used in the experiments. The SS meshes were coated with inner non-porous 'protective' titania and outer porous 'dye loading' titania layers. The dense titania coatings were made by dip coating the mesh substrates into titania sol-gel and then sintering them at 150 $^{o}$C for 10 minutes after each dip coating step and they were finally annealed at 500 $^{o}$C for 15 minutes. The protective coating thickness was controlled by varying the number of dipping steps used. The porous titania coatings were made by spray coating the substrates with titania dispersion. The thickness of the coating was controlled by varying the concentration of titania precursor while keeping the spraying time and other conditions constant. The SS mesh substrates were finally sintered at 450 $^{o}$C for 30 minutes. The titania coated FTO photo-

anodes were prepared by doctor blade coating with titania dispersion. The sintering and dye-soaking steps were the same as used for SS mesh substrates.

Titania sol-gel for dip coatings was synthesized as reported in [78] with titanium isopropoxide (Sigma Aldrich), anhydrous ethanol and acetic acid (Sigma Aldrich) as precursors. The titania dispersion was synthesized with P25 (Degussa), acetyl acetone (Sigma Aldrich), DI water and Triton X-100 (Sigma Aldrich) as reported in [79]. Dye sensitization of $TiO_2$ films was done by soaking the SS mesh coated with bi-layer titania in $3x10^{-4}$ M ethanol solution of $RuL_2(NCS)_2$ : 2 TBA; L = 2,2'-bipyridyl-4,4'-dicarboxylic acid ; TBA = tetrabutylammonium (Solaronix), overnight. Pt counter electrodes were prepared by sputtering ~ 150 nm of Pt onto glass substrates. The liquid electrolyte used was composed of 0.70 M 1-vinyl-3- methyl-immidazolium iodide (Sigma Aldrich), 0.10 M LiI (Sigma Aldrich), 40 mM iodine (Sigma Aldrich), and 0.125 M 4-tert-butylpyridine (Sigma Aldrich) in 3-methoxypropionitrile (Sigma Aldrich). The dye solar cell was tested at 1 sun with an aperture area of 0.25 $cm^2$. Impedance spectroscopy measurements were performed with a Solartron SI 1286 impedance analyzer, under open circuit voltage conditions at an illumination of 100 $mW/cm^2$ in the frequency range of 1 MHz to 50 mHz and a signal amplitude of 10 mV.

## 2.3 Results & Discussion

### 2.3.1 Dye Solar Cells on bare SS mesh substrates

Bare SS meshes spray coated with titania dispersion without the protective titania layer had low open circuit voltage and low short circuit current as observed in figure 2.2.

Also from the impedance spectroscopy data in table 2.1 it is clear that a significant barrier to electron transport is present when bare SS mesh substrates were used as electrodes. The drop in short circuit current is due to the increased impedance of SS mesh electrodes and due to reduction in light absorption. Since ~ 30% of the mesh area (figure 2.3.c) is open leading to reduced effective area for energy harvesting. SS mesh openings should be open as in figure 2.3.a because if it is closed it increases the electron and ion transport resistances of the device as quantified in table 2.1. An explanation of the phenomenon is given in section 2.3.4.

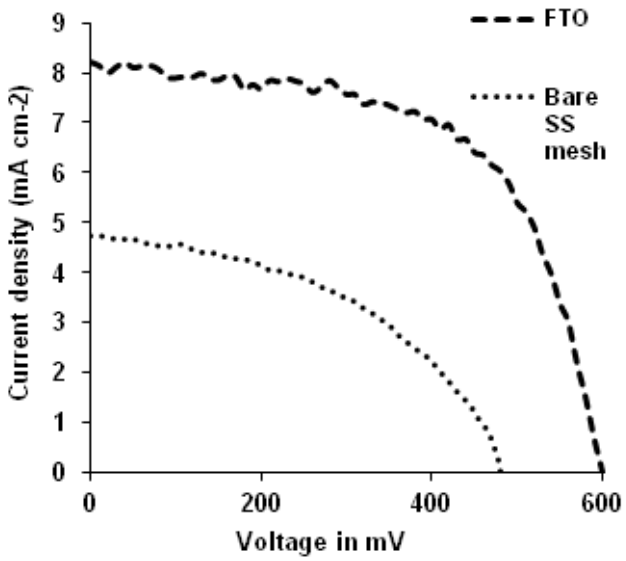


**Figure 2.2 Current-voltage curves for bare SS mesh and FTO based Dye Solar Cells.**

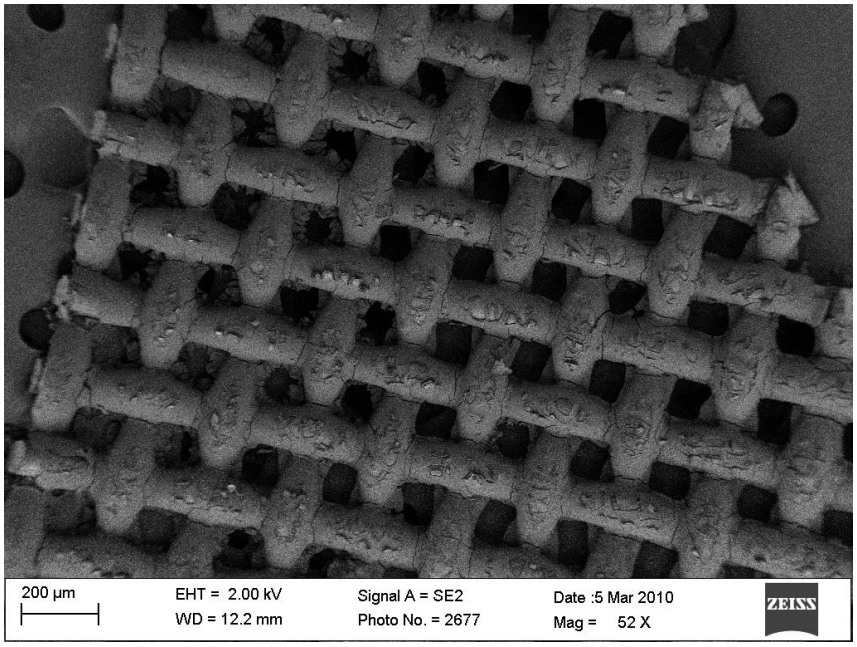
200 µm
EHT = 2.00 kV
WD = 12.2 mm
Signal A = SE2
Photo No. = 2677
Date :5 Mar 2010
Mag = 52 X
ZEISS

(a)

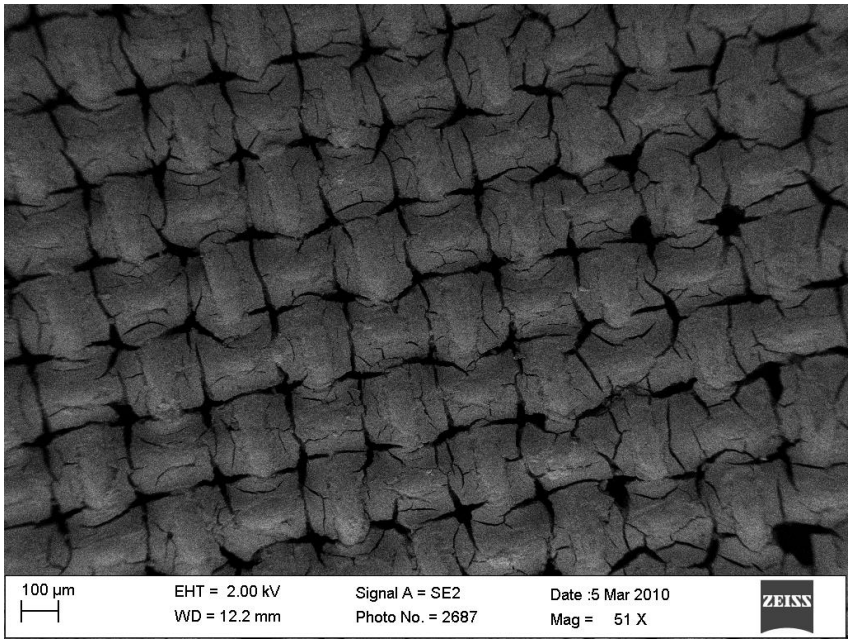
100 µm
EHT = 2.00 kV
WD = 12.2 mm
Signal A = SE2
Photo No. = 2687
Date :5 Mar 2010
Mag = 51 X
ZEISS

(b)

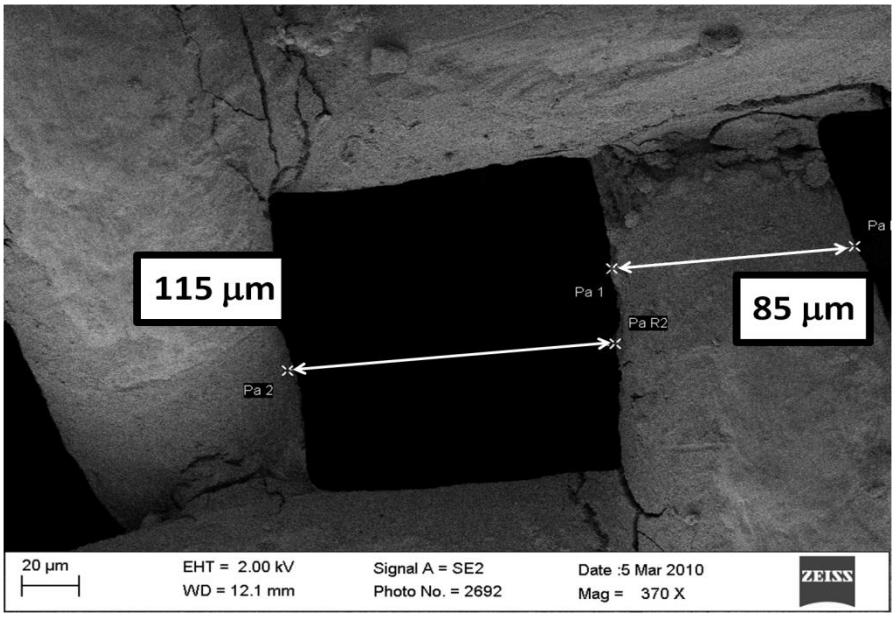


(c)

**Figure 2.3 SEM pictures of titania coated SS mesh electrodes a) with mesh openings open b) with mesh openings closed with titania c) close up for dimensions of mesh opening.**

The increased impedance to electron transport in SS mesh electrodes is attributed to the oxidation of SS mesh which increases the SS / $TiO_2$ interface resistance. The work function for FTO typically used in DSSC is ~ 4.4 eV, which forms an ohmic contact with $TiO_2$. By contrast, stainless steel on oxidation is thought to form a thin n-type semiconductor layer of $Fe_2O_3$, which has a work function of ~5.5 eV, while Fe has a work function of 4.7 eV [80]. Therefore, $Fe_2O_3$ will act as a recombination layer, preventing electrons transfer from $TiO_2$ to the metal current collector. This results in non-ohmic contact of higher impedance, and reduced open-circuit voltage. This is consistent with

our impedance data in table 2.1. Evidence of the oxidation of SS can also be seen from the optical pictures of the SS mesh in figure 2.4.

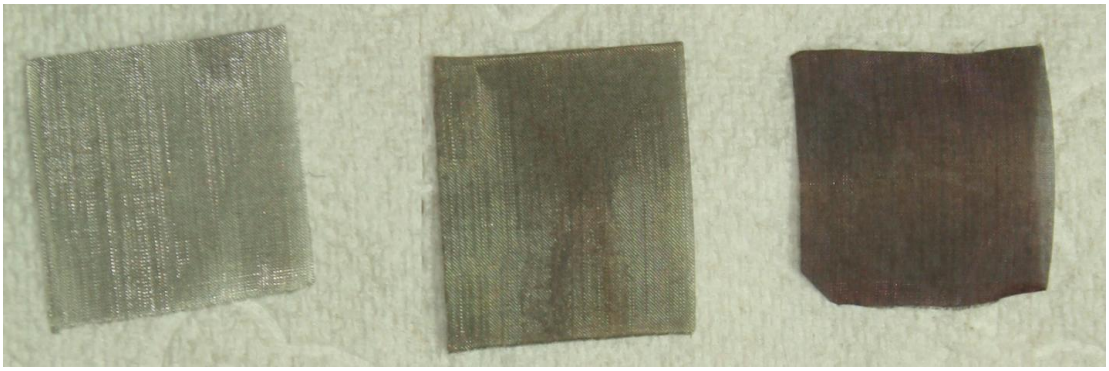

**Figure 2.4 SS mesh before heating (left), SS mesh coated with dense titania protective layer heated at 450 deg C for 30 mins (center) and bare SS mesh heated at 450 deg C for 30 mins (right).**

### 2.3.2 Dye Solar Cells on non-porous titania coated SS mesh substrates

To prevent the oxidation of SS, dense titania coatings were applied to the mesh through a sol-gel route by dip coating, as described above. The decrease in oxidation is due to a non-porous protective layer of titania covering the SS mesh and is visible from the optical picture above. The electrodes with protective titania coatings had higher open circuit voltage, 580 mV, compared to 490 mV with no sol-gel layers as observed in table 2.1 and figure 2.5. The number of sol-gel layers was optimized and the best performance cell was obtained with 63% efficiency improvement compared to cells without sol-gel layers. Since the effective area for light absorption in 120 counts SS mesh is 30% less (figure 2.3) than FTO, its effective area was normalized to compare with the performance of FTO.

**Table 2.1Photovoltaic parameters and impedance data of the dye solar cells.**

| Substrate | $V_{oc}$ mV | $J_{sc}$ (a) mA / $cm^2$ | FF | η (a) % | Rs ohms | $R_{TiO2}$ Ohms | $R_{Pt}$ ohms |
|---|---|---|---|---|---|---|---|
| FTO | 600 | 8.2 (8.2) | 0.6 | 3.02 (3.02) | 33.33 | 30.6 | 4 |
| Bare SS mesh | 490 | 4.72 (6.84) | 0.44 | 1.03 (1.47) | 25.3 | 188 | 6 |
| SS mesh coated with protective titania layer | 572 | 5.32 (7.72) | 0.55 | 1.68 (2.45) | 13.75 (b) 34.5 (c) | 91.6 (b) 118.9 (c) | 6 |

(a) Values in parentheses are normalized for effective light absorbing area due to mesh openings

(b) SS mesh electrodes with mesh openings open (see figure 2.3a)

(c) SS mesh electrodes with mesh openings blocked (see figure 2.3b)

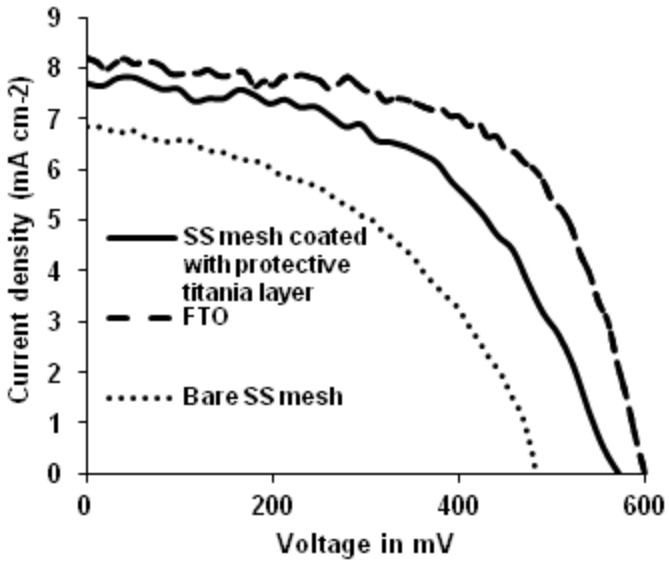


**Figure 2.5 Current-voltage curves comparison with normalization for effective light absorbing area of the mesh.**

### 2.3.3 Impedance Spectroscopy

From the Nyquist plots of the dye solar cells under illumination (figure 2.6), we can extract the impedance data reported in table 2.1. At high frequencies the series resistance Rs is found. At mid frequencies is a semi-circle attributed to the Pt / electrolyte interface and at low frequencies is a semi-circle attributed to the $TiO_2$ charge transfer resistance. It is observed that series resistance ($R_s$) of SS mesh electrodes is lower than FTO. But the $TiO_2$ charge transfer resistance ($R_{TiO2}$) for SS mesh electrodes is higher than FTO. Since the $TiO_2$ / dye / electrolyte interface is the same in FTO and SS mesh, this increase in resistance is attributed to the oxidation of SS mesh during sintering process. SS on oxidation predominantly forms $Fe_2O_3$ [79]. $Fe_2O_3$ has a Fermi level higher compared to $TiO_2$ and due to multiple valence of $Fe^{3+}$ ions, which are known to act as recombination sites in $TiO_2$ [80, 81], the interface resistance of SS / $TiO_2$ is higher

compared to FTO and the open-circuit voltage is lower because of recombination. Reducing the oxidation of SS mesh by protecting it with dense titania layer reduces the interface resistance by more than 50% (table 2.1). Also reducing the oxidation of SS mesh lowers the series resistance of the device. Impedance spectroscopy can provide useful information on both electronic current flow and ionic current flow in the high frequency part of the spectrum. Typically, the electrolyte ionic conductivity is part of the series resistance. The effect of blocking ionic current flow can be seen in the increase in series resistance from 13.75 to 34.5 ohms when mesh openings are closed with $TiO_2$. We note this value is still very close to the series resistance of the FTO electrode. This suggests that the limiting factor is not ionic diffusion, but $R_{TiO2}$ , which is still three times higher than in the case of FTO.

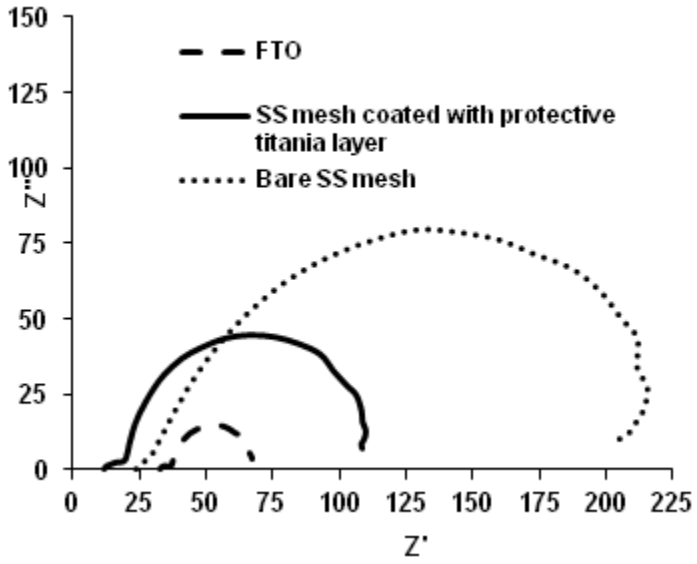


**Figure 2.6 Nyquist plots under identical illumination conditions.**

Comparing protective titania layer coated SS mesh with FTO, series resistance of SS mesh electrode is ~ 60% lower than FTO based device due to higher conductivity of metals compared to TCO's. But the resistance at $TiO_2$ / dye / electrolyte interface for SS

mesh is 3 times higher than FTO based device. This illustrates that there is still partial oxidation of SS mesh occurring which is confirmed from the optical picture in figure 2.4. By better protecting the SS mesh through improvement of the dense titania deposition methods then better SS anodes for DSSC could be developed. Further reduction in series resistance of the device could be obtained by replacing Pt sputtered TCO with Pt sputtered SS foil as the counter electrode because of higher conductivity of metals compared to TCO's.

### 2.3.4 Microstructure and coating effects on SS mesh electrodes

The P25 dispersion on SS mesh was deposited through dip coating, blade coating and spray coating methods. In dip coating and blade coating methods the coatings either blocked the mesh openings entirely due to the non-uniform morphology of mesh architecture or it was so thin that the performance of the device was low. So we report only the data for cells with spray coated titania dye-adsorption layers.

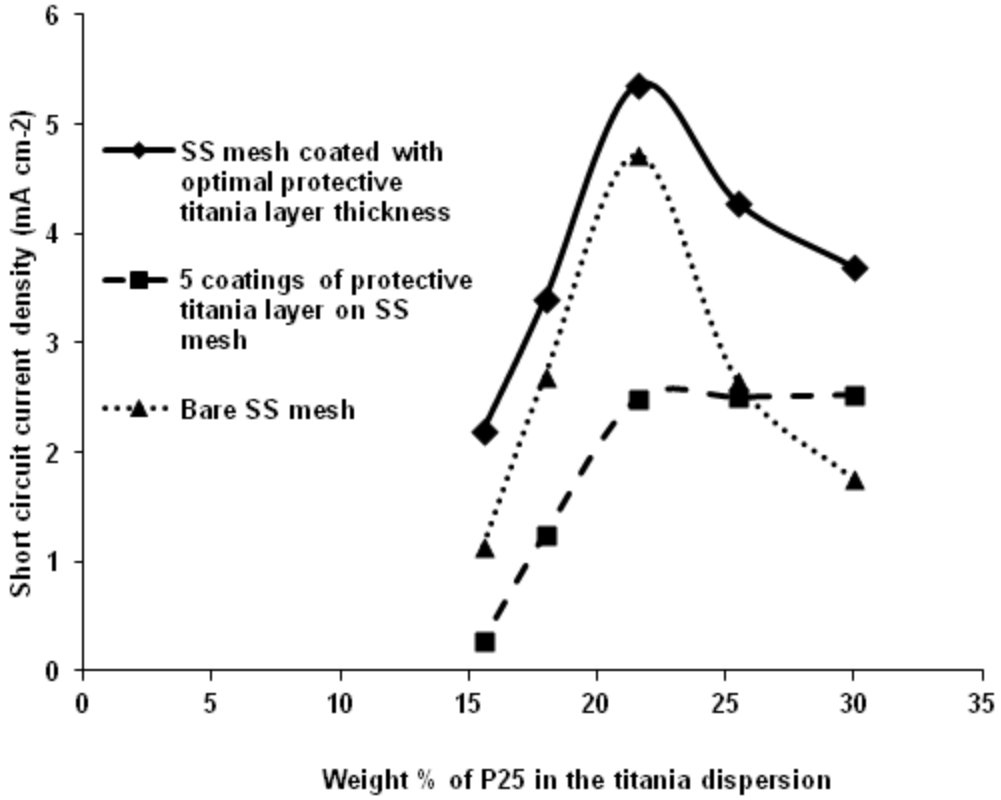


**Figure 2.7 Effect of dense and porous titania coating thickness on the performance of Dye Solar Cells.**

Protective and porous titania layers were optimized separately. Protective titania layer thickness was controlled by varying the number of times the meshes were dip coated and the porous titania layer thickness was varied by changing the concentration of P25 in the titania dispersion which was uniformly sprayed on top of the SS mesh electrodes for 5 seconds. The best performance was obtained for SS meshes dip coated twice in titania sol-gel and sprayed with titania dispersion containing 21.5 % by weight of P25 in it.

Comparing SS mesh electrodes dip coated twice and dip coated five times with titania sol-gel (figure 2.7), it was noted that the electrodes dip coated with 5 times had higher series and $TiO_2$ / dye / electrolyte interface resistances. This was attributed to the thick protective layers of titania covering the mesh and clogging the mesh openings thereby impeding the ionic current flow.

Keeping the protective titania layer thickness constant at two dip coatings, the effect of variation in porous titania thickness on the performance of the cell was also studied (figure 2.7). Due to the difficulty in measuring the titania thickness because of the mesh morphology, the concentration of P25 in the dispersion was used as the metric. At lower P25 concentrations, the performance of the device was poor due to lower dye loading. At concentrations above 21.5% it was noted that titania was beginning to block the mesh openings due to its increased thickness. Blocking of mesh openings increases light absorption as it increases the effective light absorbing area, but it also increases the series resistance of the device as the ions in the electrolyte have to travel a longer distance through the titania to reach the Pt counter electrode. The ideal titania coating thickness for FTO based planar DSSC are known to be in the range of 12 ~ 15 μm. For the SS mesh electrodes if the mesh openings are completely blocked with titania, then for the electron – ion pairs generated at the front surface of SS mesh, the ions in the electrolyte have to travel a distance of 90 μm of porous titania layer (diameter of the wire) to reach the Pt counter electrode. Thus increasing titania concentration beyond 21.5% increases the series resistance by blocking mesh openings thereby lowering the performance of the device as observed in figure 2.8.

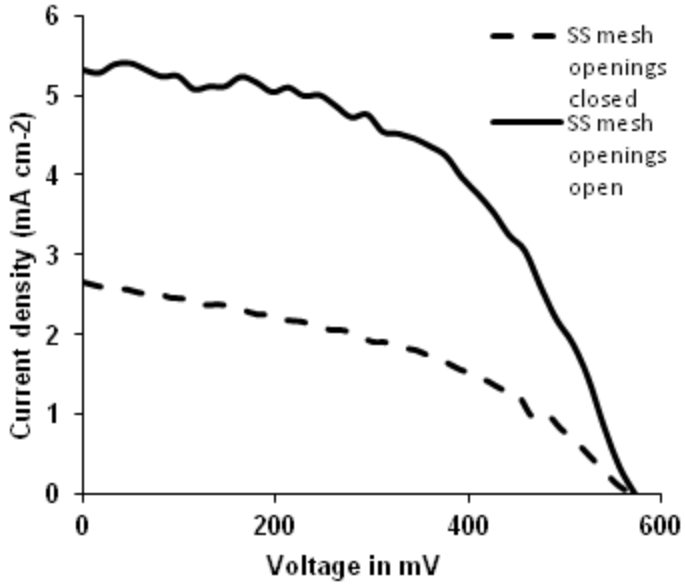


**Figure 2.8 Current-voltage curve of Dye Solar Cells with mesh openings open and closed.**

## 2.4 Conclusion

In the present work 120 count SS meshes were used as electrodes for DSSC which have an opening area of 30%. We have evidenced a lower series resistance for stainless steel mesh electrodes compared to FTO coated glass. This is very advantageous for current collection in large area modules. We have also observed the detrimental effect of stainless steel oxidation and demonstrated it could be significantly reduced by pre-treating the meshes with a dense titania sol-gel coating. This resulted in 63% improvement solar power conversion efficiency over uncoated SS meshes, with $\eta$ = 1.68%, compared to $\eta$ = 3.0% in FTO reference cells[1].

[1] This work has been published as "Electrical and optical studies of flexible stainless steel mesh electrodes for dye sensitized solar cells" in Solar Energy Materials and Solar Cells, DOI: 10.1016/j.solmat.2011.03.010. Copyright 2011 Elsevier BV. It is reprinted here with permission.

# CHAPTER 3

## 3. Solution deposition Copper Zinc Tin Sulfide ($Cu_2ZnSnS_4$)

### 3.1 Background and motivation

Copper zinc tin sulfide, $Cu_2ZnSnS_4$ (CZTS) is a promising solar light absorber with all of its constituent elements being low cost. It has a Kesterite crystal structure with p-type conductivity and a direct band gap of >1.5 eV [61]. It is being researched extensively as a light absorbing p-type semiconducting material for thin film solar cells because of its high absorption coefficient, direct band gap, and availability of constituent materials in abundance. Devices with CZTS as a light absorber and p-type semiconductor and zinc oxide (ZnO) as the n-type semiconductor have yielded efficiencies of 11.1% [61]. Also since the band gap of CZTS is >1.5 eV, it could also be a potential future candidate as top cell for silicon in tandem mechanical solar cell architecture.

It has so far been challenging to produce stoichiometric CZTS thin films because of the high volatility of tin sulfide, sulfur and zinc, leading to deficiency and non homogeneity of thin films. In this chapter synthesis and characterization of solution deposited CZTS films is described. In order to control the volatility, solution deposited thin films were annealed in an environment of tin sulfide and sulfur vapors. The as-annealed thin films' composition, structure, morphology, and electronic properties were characterized. It was determined that the films annealed in tin and sulfur environment had high crystallinity, homogeneity, and good opto-electronic properties. The band gap of the

deposited films were measured to be 1.5 eV, which is a suitable for tandem devices. More discussion about the choice of band gap and material for tandem devices is discussed in chapter 6.

## 3.2 Experimental

The sol-gel like system was prepared by adding 1 M of Copper(I) Iodide (99.99%), 0.5 M of Zinc(II) Acetate (99.99%), 0.5 M of Tin(II) Chloride (97%) and 3 M of Thioacetamide (99.99%) in Pyridine as adapted from [82]. The precursors were then stirred over night to form a suspension. The prepared suspension was then blade coated on to a Fluorine doped Tin Oxide (FTO) coated glass with a surface resistivity of 15 ohms per square and also molybdenum sputtered glass substrates.

The coated substrates were then annealed in a tube furnace under flowing argon conditions at 450 deg C for 30 mins. The substrates were placed in a ceramic vessel inside the tube furnace with 40mg of Sulfur and 10 mg of Tin powder, to create an excess vapor pressure of Tin and Sulfur in order to prevent loss of Tin and Sulfur from the substrates.

## 3.3 Results and Discussion

Chemical, structural and optical properties of the annealed solution deposited thin films were analyzed, figures 3.1 and 3.2 shows the x-ray diffraction pattern (XRD) and Raman spectra of the deposited films. From figure 3.1, it is seen that the deposited film is polycrystalline with high crystallinity in <112> direction. Since the CZTS XRD peaks overlap with ZnS and $Cu_4SnS_4$ peaks Raman spectra were obtained to confirm the

presence of CZTS. Figure 3.2 provides the characteristic signature of CZTS Raman spectra.

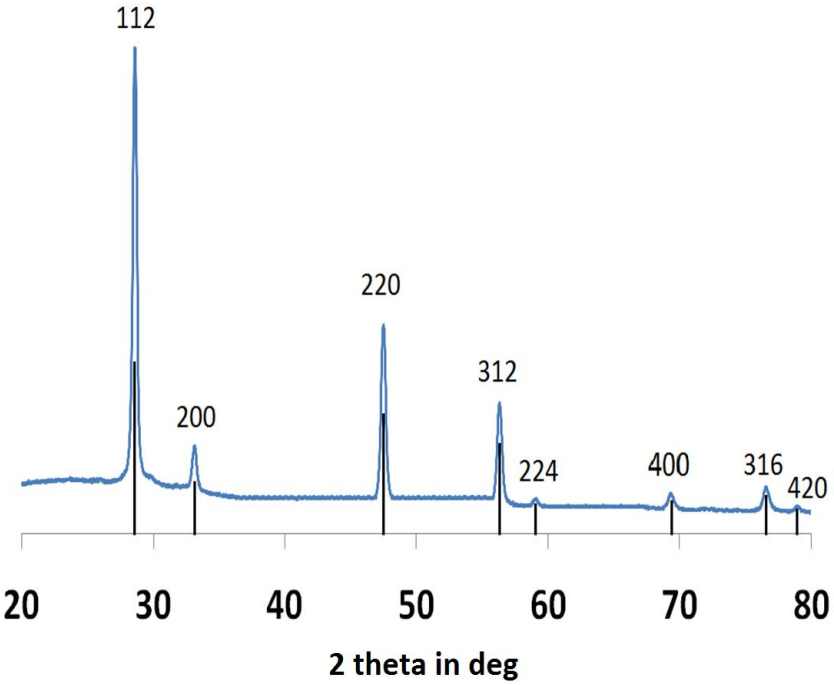


**Figure 3.1 X-ray diffraction pattern of annealed CZTS thin film.**

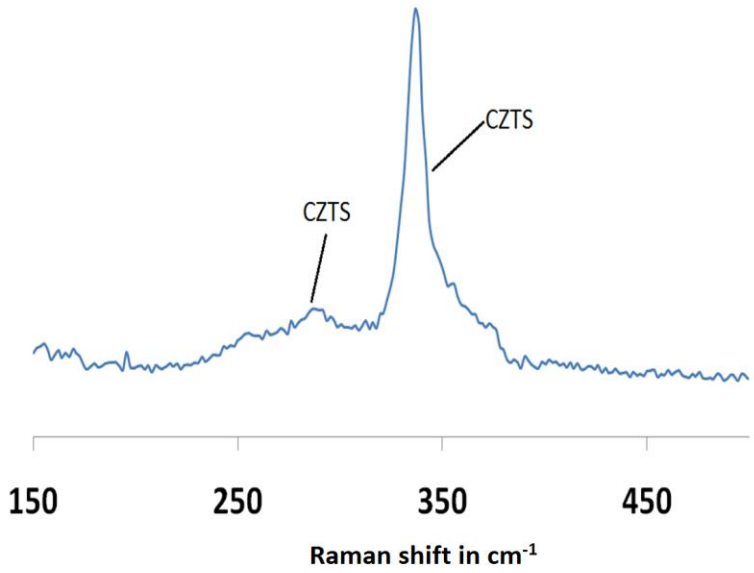


**Figure 3.2 Raman spectrum of annealed CZTS thin film.**

The band gap of the deposited film was obtained using UV visible spectroscopy as shown in figure 3.3, the deposited films band gap was calculated to be 1.5 eV in agreement with the published values [61]. The absorption coefficient was found to be greater than $10^4$ $cm^{-1}$ again in agreement with the published values of CZTS [61].

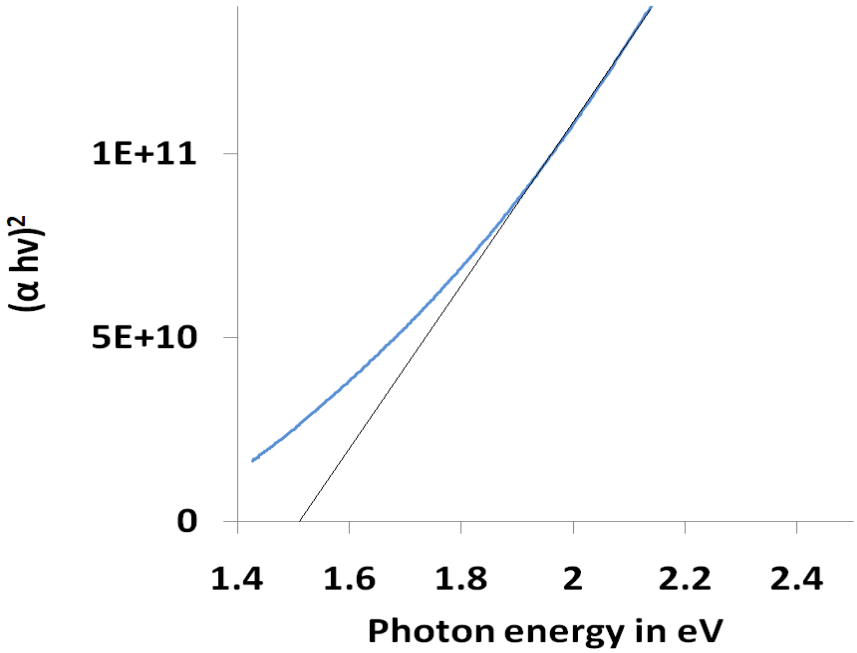


**Figure 3.3 Absorption band edge calculation from U-V visible spectroscopy.**

Composition data from energy dispersive spectroscopy (EDS) in table 3.1, shows that the films are copper deficient, which is known to be ideal for making solar cells [61]. Also the film is Zinc rich and Tin poor, which is also known to be favorable for solar cells [61]. The morphology of the film is shown in figure 3.4, it is highly porous due to volatile precursors making it not suitable for making devices.

**Table 3.1 Composition of the annealed CZTS film obtained through energy dispersive spectroscopy.**

| Atomic % Cu Actual (Target) | Atomic % Sn Actual (Target) | Atomic % Zn Actual (Target) | Atomic % S Actual (Target) |
|---|---|---|---|
| 23% +/- 0.3% (25%) | 12% +/- 0.4% (12.5%) | 13% +/- 4% (12.5%) | 49% +/- 0.6% (50%) |

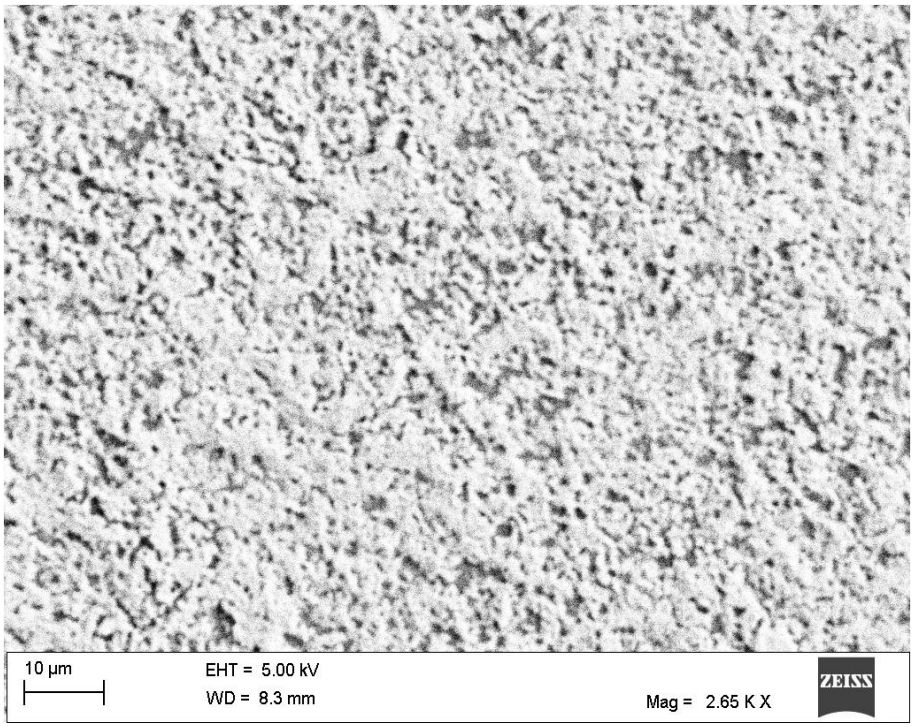


**Figure 3.4 SEM image of the annealed CZTS film.**

## 3.4 Conclusion

The deposited CZTS films were highly crystalline and the measured band gap of 1.5 eV was close to the known values reported in the literature. The deposited films were copper deficient and zinc rich which have been known to provide high efficiencies.

However the deposited thin films were highly porous making it unsuitable for fabricating devices. So multi-layer spin coating and annealing procedure was tried, but due to high volatility of the precursors and due to high vapor pressure of the deposited film the obtained films were still porous. So an alternative solution deposition route to deposit CZTS should be explored in the future.

# CHAPTER 4

## 4. Silicon / Germanium Tandem Four Terminal Solar Cells

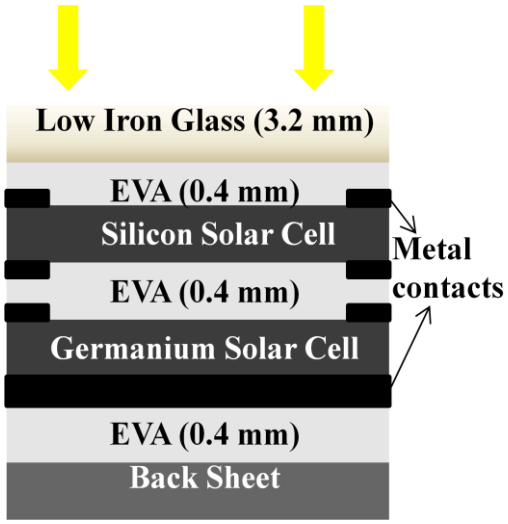


### 4.1 Background and Motivation

In this work we examine a mechanical tandem structure with silicon being the high band gap top solar cell as it constitutes majority of the global solar cell production. Germanium, which has a band gap of 0.662 eV was selected as the low band gap second cell as it was closest to the ideal band gap of 0.68 eV for silicon based tandem solar cells as shown in figure 4.1. Germanium's band gap is attractive for accessing infra-red light absorption from 1107 nm to 1907 nm. Wavelengths from 1107 nm to 1907 nm have an integrated light intensity of 145 $W/m^2$ contributing ~ 14.5% of the total power in the AM1.5 solar spectrum. The theoretical efficiency of a silicon/germanium tandem device is calculated to be as high as 38% as shown in figure 4.1. Though the increase in theoretical efficiency compared to single junction silicon device is ~ 6%, a low cost light

absorber targeting infrared spectrum or germanium which belongs to the same group as silicon, though much expensive than silicon, it could be processed to make solar cells in a similar manufacturing environment with little modifications leading to lower capital cost. The illustration of the device architecture is shown in figure 4.2.

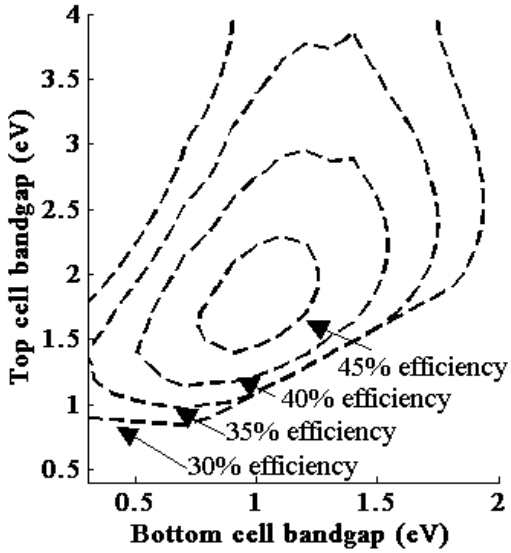


**Figure 4.1 Theoretical conversion efficiencies based on Shockley and Queisser limit for two junction (mechanical stack) solar cells under AM 1.5 solar spectrum.**

We report here on the electrical and optical simulations of this tandem structure, quantifying the various theoretical and practical loss mechanisms in the encapsulation, interfaces and in the device and indicate that a relative efficiency improvement of greater than 12% may be attainable in this configuration with present technology and show that a relative efficiency improvement of over 20% may be feasible with improvements in surface passivation of germanium solar cell.

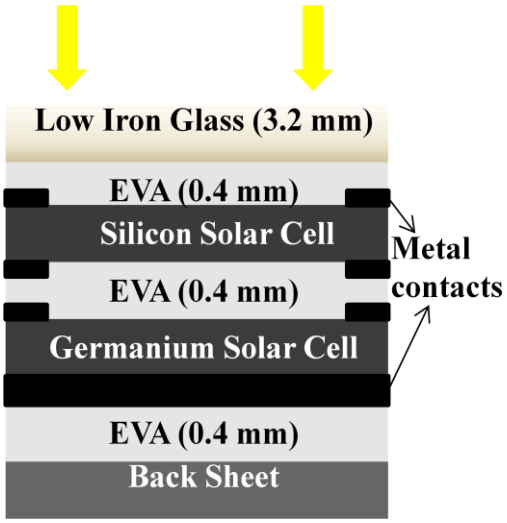


**Figure 4.2 Illustration of the proposed Si/Ge tandem solar cell.**

## 4.2 Experimental

The silicon solar cell device used in the simulations were modeled in two different device configurations, as a HIT (Heterojunction with Intrinsic Thin layer) cell with n-type wafer, a-Si surface passivation on both the surfaces and as a conventional silicon cell with p-type wafer, $SiN_x$ surface passivation on both the surfaces. Illustration of the modeled silicon solar cells are shown in figure 4.3. Both these device architectures have metallic fingers as front and back contacts thereby allowing long wavelength light to pass through the device [83 - 84] and be absorbed at the germanium solar cell. For convenience in the remaining sections of the manuscript the two different silicon solar cell device configurations will be termed as HIT (for n-type wafer, a-Si surface passivation) and bifacial (for p-type wafer, SiNx surface passivation). The material parameters of the individual layers used in the simulation models, their thicknesses and device configuration were obtained from [83 - 94]. In the optical modeling analysis only bifacial silicon solar cell was considered because of the non-availability of the absorption

and refractive index parameters for Indium Tin Oxide (ITO) and a-Si layers in HIT solar cell for the complete solar spectrum.

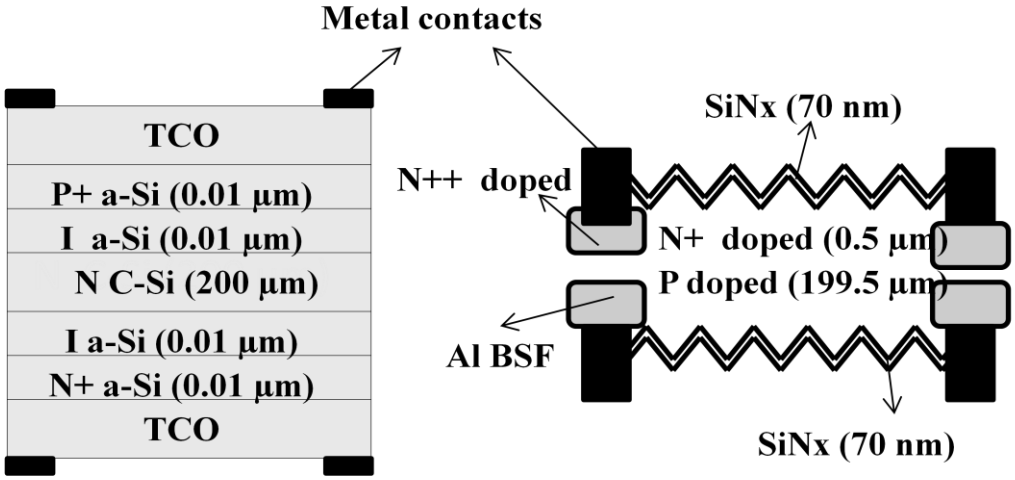


**Figure 4.3 Illustration of the modeled silicon solar cells. On the left is the HIT and on the right is the bifacial solar cell architecture.**

The germanium solar cell was modeled based on the device fabricated and characterized by Posthuma et al reported in [95-97]. Figure 4.4 provides the illustration of the modeled germanium solar cell. The material properties for the germanium solar cell were obtained from [90-92, 95-97].

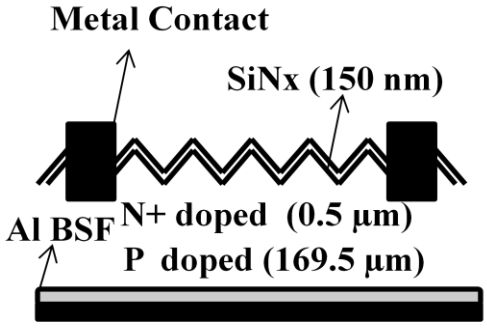


**Figure 4.4 Illustration of the modeled germanium solar cell.**

The electrical simulations of the modeled devices were performed using WxAMPS developed at University of Illinois [55]. WxAMPS is a tool for one-

dimensional numerical simulation of opto-electronic devices, an updated version of AMPS 1-D developed by Prof. Fonash at Pennsylvania State University [56, 57]. It allows for modeling of various recombination effects due to mid-gap states, Shockley-Read-Hall (S-R-H), band-band and incorporation of surface recombination effects. The simulation works by solving for poisson's, electron and hole continuity equations iteratively. Optical modeling and simulation of the non-textured antireflective coated devices were modeled in Matlab as thin solid films [58, 59] and textured antireflective coated devices by finite-difference time-domain (FDTD) method using Lumerical. The thickness of the antireflective coatings were calculated through simulations, texturing of silicon solar cell was modeled based on the data reported in [98], texturing of the germanium solar cell was done identical to silicon, material property data of SiNx antireflective layer was obtained from plasma enhanced chemical vapor deposition (PECVD) experiments which are reported in [99], absorption coefficients and refractive indices of encapsulation and low iron glass were obtained from [100] and [101] respectively. Figure 4.5 and figure 4.6 provides a plot of extinction coefficient and refractive index against wavelength of light for all the materials used in the simulation. The thickness of the encapsulation and low iron glass were based on the information available from module manufacturers.

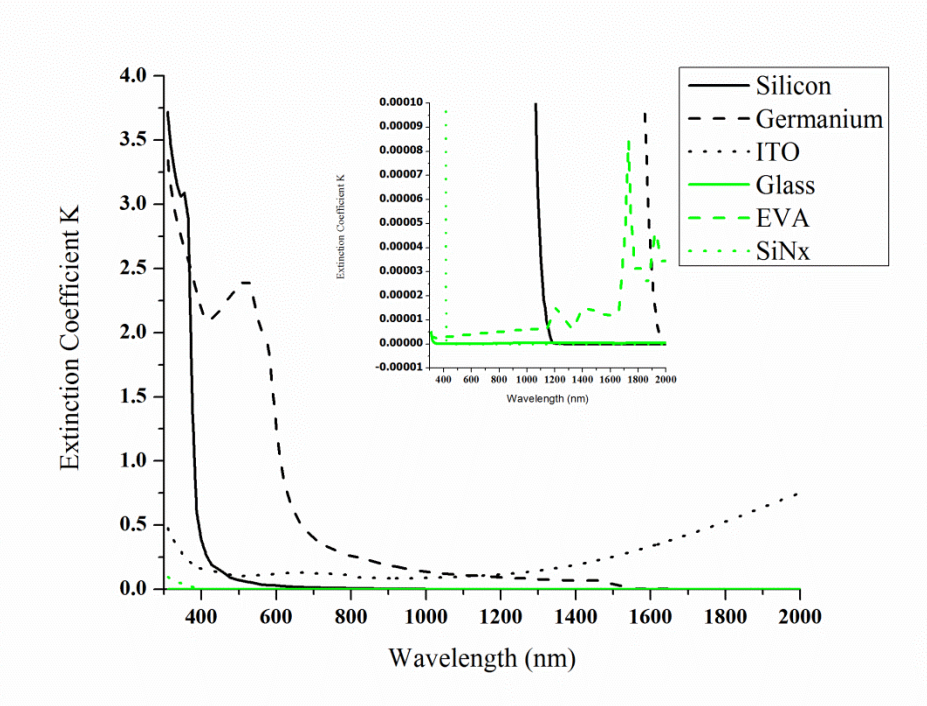


**Figure 4.5 Extinction Coefficient of the materials used in the tandem device.**

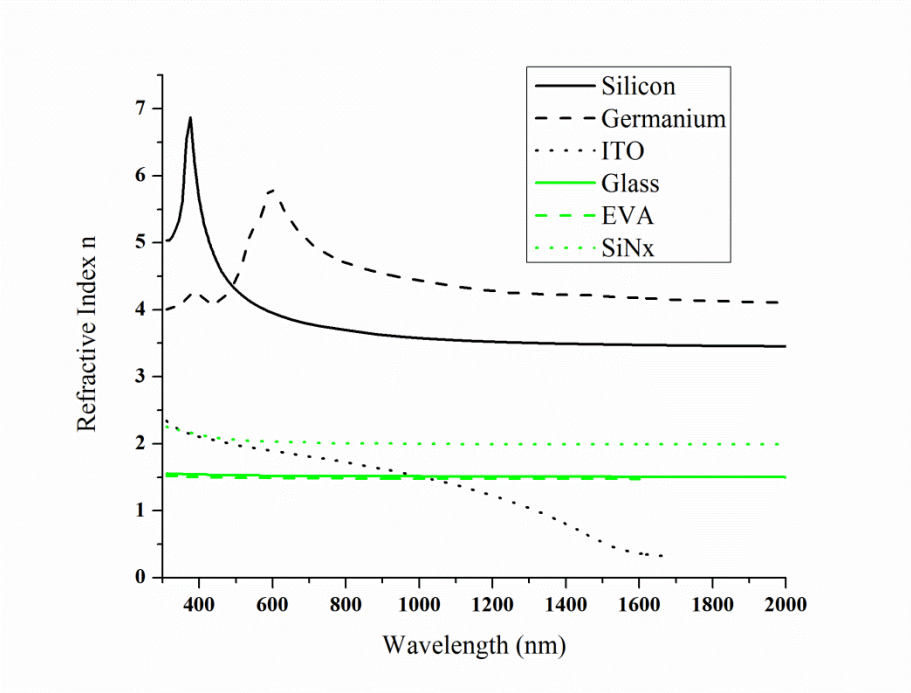


**Figure 4.6 Refractive Index of the materials used in the tandem device.**

## 4.3 Results & Discussion

### 4.3.1 Optical losses in the top (Silicon) solar cell

Absorption and reflection losses in encapsulation and anti-reflection coating layers for the proposed device architecture were calculated for AM 1.5 solar spectral intensity. Figure 4.7 shows the optical loss percentages at the various layers of the top solar cell before the light strikes the silicon layer. Here in this analysis the silicon layer was modeled as a textured surface with 70nm silicon nitride anti-reflection coating, 0.4 mm ethylene vinyl acetate (EVA) sheet on top of the silicon nitride layer which acts as an encapsulant and a 3.2 mm low iron glass on top which does not have an antireflection coating. The reflection loss at the air / glass interface was on an average 4.2% with +- 0.2% at lower and higher wavelengths respectively. Since refractive index of EVA is very close to glass as seen in figure 4.6 the reflection loss due to the index mismatch has been neglected. The silicon nitride antireflection coating thickness was optimized for reducing the reflection loss at the operation wavelengths of silicon solar cell therefore the reflection loss is higher for longer wavelengths as shown figure 4.7. Absorption loss due to combined glass and EVA, is shown in figure 4.7, were high at U-V wavelength ranges because of higher extinction coefficient of glass at those wavelengths, the absorption loss is on an average around 3.64% in visible wavelength region, 4.53% from 700 nm to 1100 nm wavelengths, 5.62% from 1100 nm to 1700 nm wavelengths and the absorption is higher for wavelengths above 1700 nm because of higher absorption coefficient of EVA. Also absorption loss of silicon nitride is high for U-V wavelength regions but the loss is very low for visible and longer wavelength regions as seen in figure 4.7. The total light intensity available at silicon layer is 883.36 watts / sq.m or ~88% of the total AM 1.5

spectral intensity, i.e. ~ 12% of the incident light energy is lost due to absorption and reflection losses. The light spectrum available at silicon layer is shown in figure 4.8.

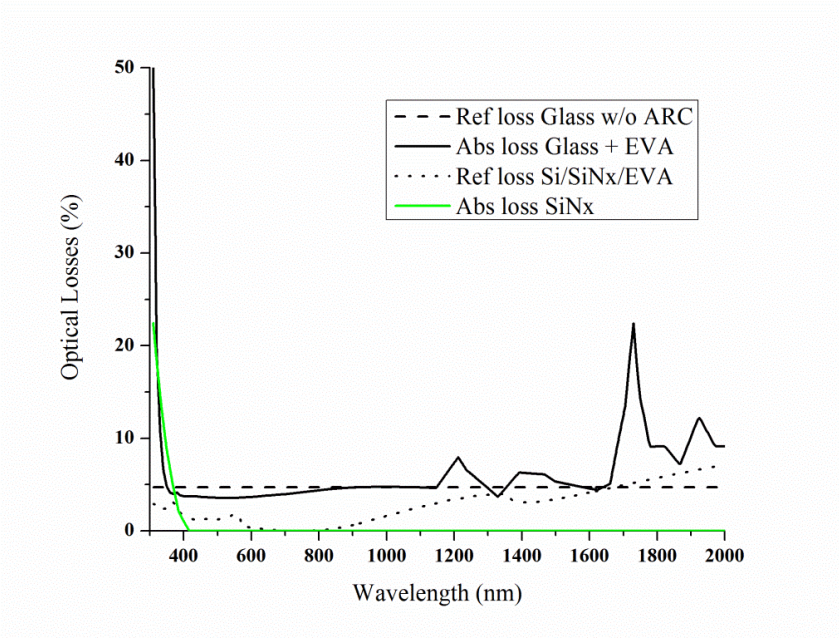


**Figure 4.7 Optical loss due to various layers in the top cell before the light gets absorbed by the silicon layer.**

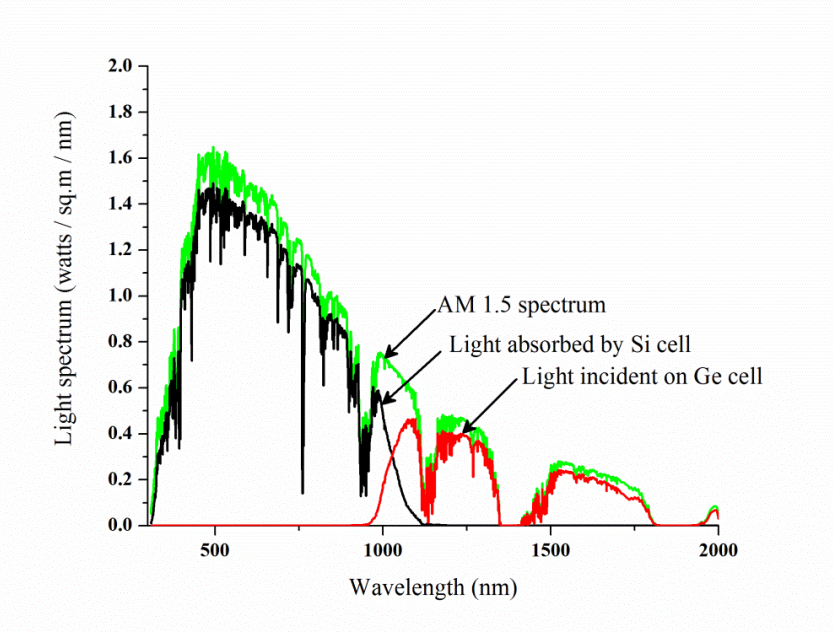


**Figure 4.8 Light spectrum incident on the tandem device, absorbed by silicon cell and light incident on germanium cell.**

### 4.3.2 Optical losses in the bottom (Germanium) solar cell

Silicon, which has a band gap of 1.12eV, is transparent to longer wavelengths of light. Of the 883 W/m$^2$ incident on the silicon surface after absorption and reflection at the front encapsulation layers, about 162.51 W/m$^2$ or ~ 16.25% of the AM 1.5 spectral intensity passes through the silicon layer without absorption as seen in figure 4.8.

In order to optically couple the Si and Ge solar cells, the bottom layer of silicon and top layer of germanium was modeled with SiNx antireflective coating with a 0.4mm layer of EVA as an encapsulant in between the cells. The SiNx thickness was increased to reduce the reflection loss at longer wavelengths relevant for the germanium cell. Figure 4.9 shows the optical loss percentages at the various layers of the bottom solar cell before the light strikes the germanium layer. Here in this analysis the germanium layer was modeled as a textured surface. The silicon nitride antireflection coating thickness was optimized for reducing the reflection loss at the operation wavelengths of the bottom germanium solar cell therefore the reflection loss is higher for visible and near infrared wavelengths as shown in figure 4.9. The reflection loss at Si/SiNx/EVA and EVA/SiNx/Ge textured interfaces are less than 1% for wavelengths below 1500 nm and for wavelengths above that reflection loss increases and reaches a maximum of 1.95% and 2.65% respectively. Absorption loss due to EVA, as shown in figure 4.9, is on an average around 4% for operational wavelength of germanium solar cell except for wavelengths above 1730 nm where EVA begins to absorb significant amount of energy. The absorption loss of silicon nitride is less for longer wavelengths because of its high optical band gap. The total light intensity available at germanium layer is calculated to be 150.2 W/m$^2$ or ~15% of the total AM 1.5 spectral intensity.

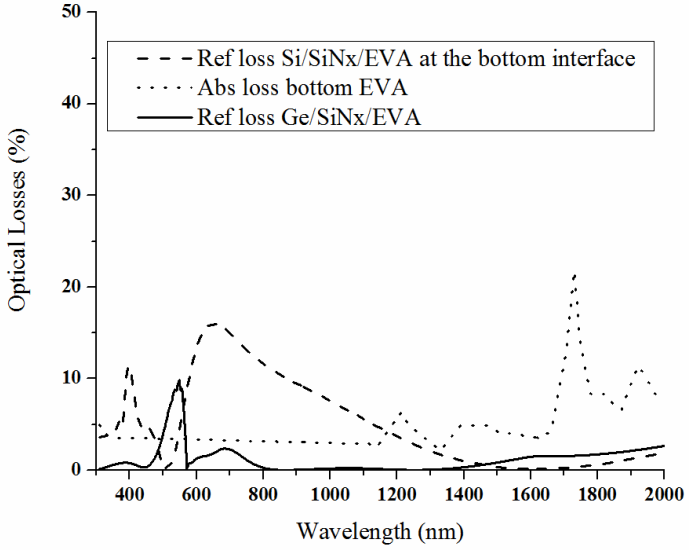


**Figure 4.9 Optical loss due to various layers in the bottom cell before the light gets absorbed by the germanium layer.**

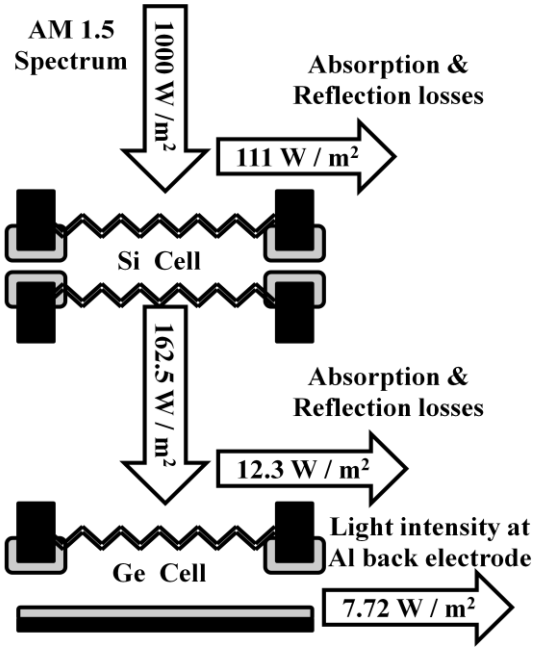


**Figure 4.10 Illustration of the light intensity available at silicon and germanium surfaces and the various optical losses in the device.**

Figure 4.10, illustrates the light intensities available at the silicon and germanium surfaces and the various optical losses in the proposed device architecture. The total front reflection and absorption losses before the light strikes the silicon surface is 111.73 $W/m^2$ or ~ 11.17% of the AM 1.5 spectral intensity. Light intensity incident on silicon surface, passing through silicon without absorption, optical loss at Si/Ge interface, incident on germanium surface and light intensity incident on the back sheet are 883.36 $W/m^2$, 162.5 $W/m^2$, 12.3 $W/m^2$, 150.2 $W/m^2$ and 7.72 $W/m^2$ respectively.

### 4.3.3 Electronic Simulation of Silicon Solar Cells

The bifacial device was modeled with a heavily doped n-type and p-type region at the front and back surface to form good ohmic contacts with the external metal contact as described in [84]. Since SiNx is known to form a good passivation at the emitter layer, the surface recombination rate for the front surface used in the simulation was 10 cm/sec as reported in [87]. At the back surface of bifacial solar cell a surface recombination rate of 1000 cm/sec was used because SiNx is not as good a passivation layer compared to Aluminum at the p-type interface in conventional silicon solar cells. The emitter region is 0.5 μm thick with uniform dopant concentration of $10^{17}$ atoms/$cm^3$. The electron and hole mobilities, conduction band and valence band density of states, electron affinity and dielectric permittivity used in the simulation were obtained from [92]. The HIT solar cell was modeled as described in [88], with a surface recombination rate of 7 cm/sec at the front and back surface. Both HIT and bifacial devices were also incorporated with mid gap and band tail defect states based on the values reported in [88]. Figure 4.11 shows the I-V curves of the simulated bifacial, HIT and the theoretical maximum (Shockley-

Queisser limit) for silicon solar cell devices taking into account the optical losses in the device shown in figure 4.6. The simulated device and best experimental cell electrical characteristics are shown in table 4.1. The difference in power conversion efficiencies between simulated and experimental devices is 2.6% and 2.8% for HIT and bifacial silicon solar cells respectively.

**Table 4.1 Current-voltage characteristics of the simulated and experimental devices.**

| Simulated Data | Voc in mV | Jsc in mA/cm2 | FF in % | Efficiency in % |
|---|---|---|---|---|
| HIT Si solar cell | 748.9 | 35.35 | 76.9 | 20.4 |
| Bifacial Si solar cell | 700.6 | 37.44 | 84.6 | 22.2 |
| c-Ge solar cell | 276.1 | 40.52 | 70.9 | 7.93 |
| c-Ge Tandem solar cell | 249.1 | 14.74 | 69.1 | 2.54 |
| Experimental cell efficiencies (from literature) | | | | |
| HIT Si solar cell [102] | 729 | 39.6 | 80 | 23 +/- 0.6 |
| Bifacial Si solar cell [84] | 647 | 36.7 | 81.8 | 19.4 |
| c-Ge solar cell [96] | 268.7 | 46.4 | 62.4 | 7.8 |

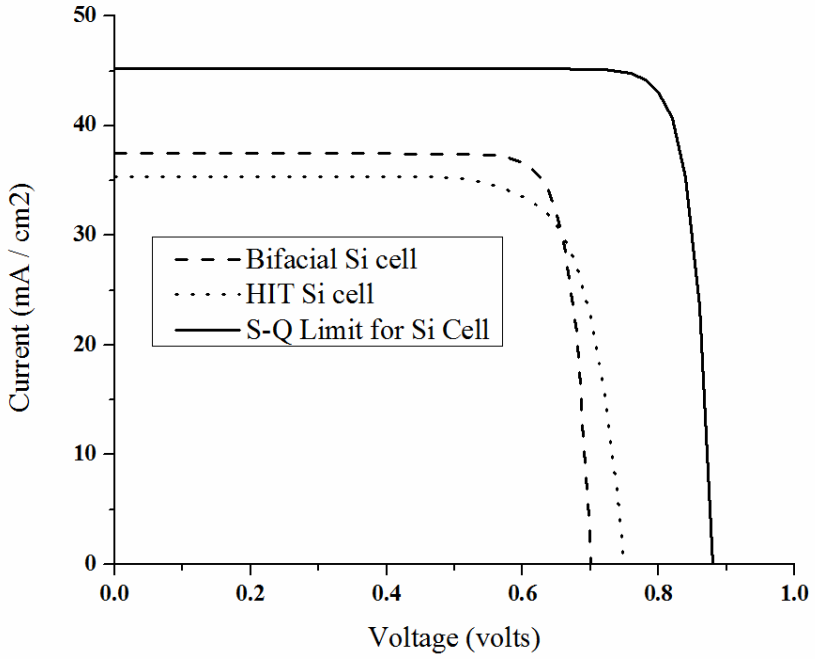


**Figure 4.11 Simulated and theoretical maximum current-voltage curves for silicon solar cells.**

Voltage, current and power loss percentages of HIT and bifacial solar cell were calculated by comparing the simulated device characteristics with Shockley-Queisser values for silicon cell and the calculated loss percentages are tabulated in table 4.2. The lower voltage loss for HIT cell compared to bifacial cell is because of the lower surface recombination rate in the HIT cell due to better passivation of the silicon surface using a-Si as described in [87,103]. The higher current loss in HIT cell is due to light absorption by the front transparent conductor oxide and amorphous silicon layers in HIT device, which also results in a lower external quantum efficiency at UV wavelengths as shown in figure 4.12.

**Table 4.2 Electrical loss in the devices.**

| Device | 1 - (Voc simulated / Voc Shockley-Queisser) (Voltage loss in %) | 1 - (Jsc simulated / Jsc Shockley-Queisser) (Current loss in %) | 1 - (Pmax simulated / Pmax Shockley-Queisser) (Power loss in %) |
|---|---|---|---|
| HIT | 15 | 13 | 34 |
| Bifacial | 20 | 8 | 28 |
| c-Ge | 40 | 33 | 59 |
| c-Ge Tandem | 41 | 6 | 51 |

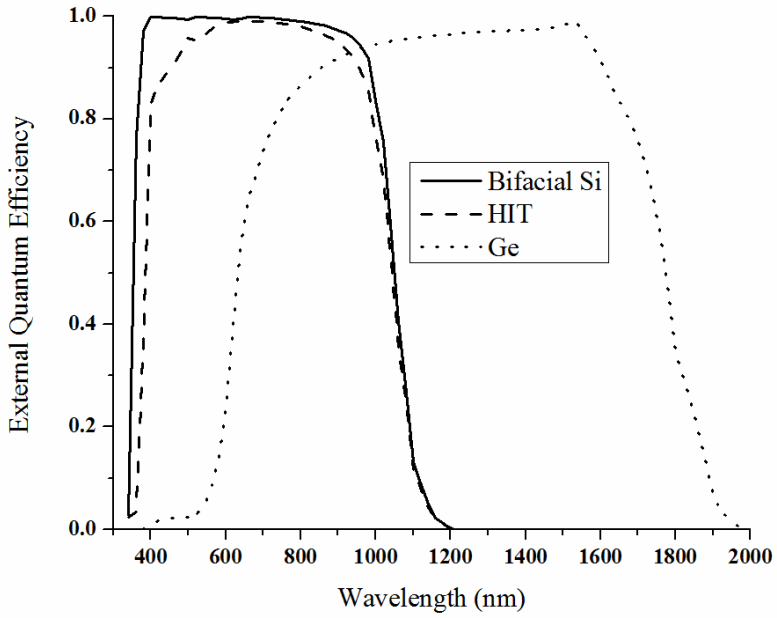


**Figure 4.12 External Quantum Efficiency of simulated silicon and germanium solar cells.**

### 4.3.4 Electronic Simulation Germanium and Tandem Germanium Solar Cells

The germanium solar cell was modeled with a wafer thickness of 170 µm, doping concentration of $10^{17}$ atoms/cm$^3$, emitter thickness of 0.5 µm and emitter doping concentration of 3 x $10^{19}$ atoms/cm$^3$, with an aluminum back surface field as described in [96, 97]. It forms an ohmic back contact but for the front it has a metal contact made of Ag having a barrier height of 0.54 eV. The electron and hole mobilities, conduction band and valence band density of states, electron affinity and dielectric permittivity used in the simulation were obtained from [92]. Surface recombination rate of 4000 cm / sec and 50 cm / sec was used for front and back contacts respectively in the simulation based on the results reported in [97] and the device was modeled with mid gap and band tail states. The I-V characteristics of a simulated stand-alone germanium device and theoretical maximum based on Shockley - Queisser limit are plotted in figure 4.13. The simulated and best experimental standalone germanium cell efficiencies are 7.93 % and 7.8 % respectively and their corresponding electrical characteristics are tabulated in table 4.1.

The germanium tandem device was simulated with a modified light spectrum taking into account the light absorption and reflection at the top bifacial silicon solar cell and at the encapsulation above the germanium solar cell, the light intensity available at the germanium surface is 150.2 W/m$^2$. The I-V characteristics of the simulated and theoretical maximum tandem germanium solar cells are shown in figure 4.13. The efficiency of germanium tandem device is 2.54% and the electrical characteristics are tabulated in table 4.1. The increase in relative efficiency of silicon / germanium tandem

solar cell, compared to standalone bifacial and HIT silicon cell efficiency is 11.42% and 12.45% respectively. Since the optical model for the top silicon cell was developed only for bifacial cell device configuration, the light spectrum transmitted through the bifacial cell was used for calculating the relative efficiency for HIT silicon / germanium cell. But HIT cell has ITO layers which has absorption in far infra-red regions as seen in figure 4.5, thereby reducing the light transmission into germanium cell and lowering the tandem cell efficiency.

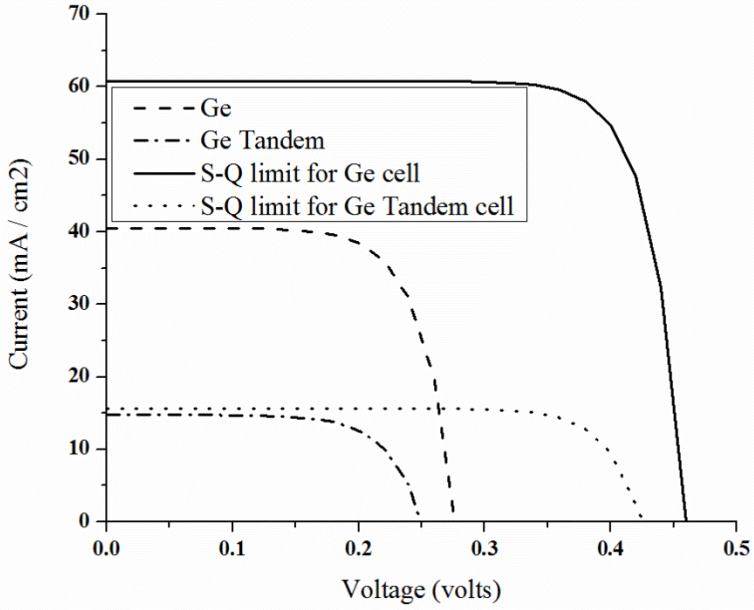


**Figure 4.13 Simulated and theoretical maximum current - voltage curves for germanium solar cells.**

The voltage, current and power loss percentages of the germanium solar cell are calculated and listed in table 4.2. The voltage loss of germanium solar cell is twice that of silicon solar cell due to large surface recombination on the front germanium surface. Lower current loss in tandem germanium solar cell compared to standalone germanium

cell is because of lower charge collection efficiency of the germanium cell at lower wavelengths as shown in figure 4.12. But the quantum efficiency is high for longer wavelengths, so tandem germanium cell which only has to absorb longer wavelengths has a very low current loss. Though the tandem germanium cell has lower current loss, the power loss is still 51% or nearly twice that of a silicon solar cell. Further improvements in efficiency of the germanium solar cell is possible by developing better front surface passivation of germanium devices in order to reduce the surface recombination. So a relative efficiency of greater than 20% compared to standalone silicon solar cells is feasible. Figure 4.13 shows the Shockley-Queisser limit for tandem germanium cell with silicon cell and encapsulation at the top, the maximum possible efficiency for the tandem germanium cell is calculated to be 5.16%.

### 4.3.5 Sensitivity analysis of silicon and germanium solar cells

In this section, the effect of some process parameters that might be adjusted during manufacturing of these devices and their effect on solar cell open circuit voltage and short circuit current are analyzed. Also, the effect of improved passivation layer, which reduces surface recombination, on solar cell electrical characteristics is analyzed.

#### *4.3.5.1 Effect of emitter doping concentration*

Emitter doping concentration was selected as a variable to investigate for modification during manufacturing because both silicon and germanium solar cells are made from their wafers which are normally made by foundries at a high degree of crystal quality. Complete cell fabrication including emitter formation, antireflection coating, and current collecting grid is done by solar cell manufacturers [17], where they make adjustments to improve the device efficiency and quality. Figures 4.14 and 4.15 show the

modeled variations in open circuit voltage and figures 4.16 and 4.17 show variations in short circuit current for different emitter doping concentrations in standalone silicon and germanium solar cells with other optical, electrical and geometric parameters held constant.

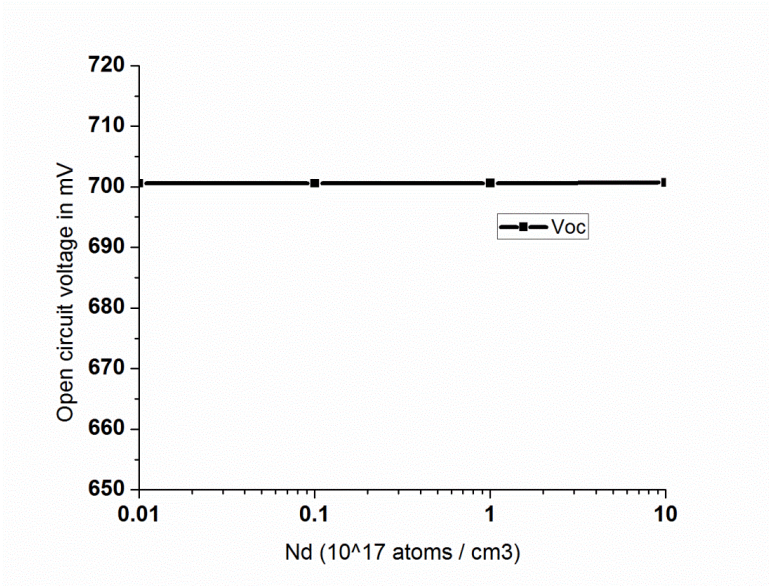


**Figure 4.14 Effect of emitter doping concentration on the open circuit voltage of standalone silicon solar cell.**

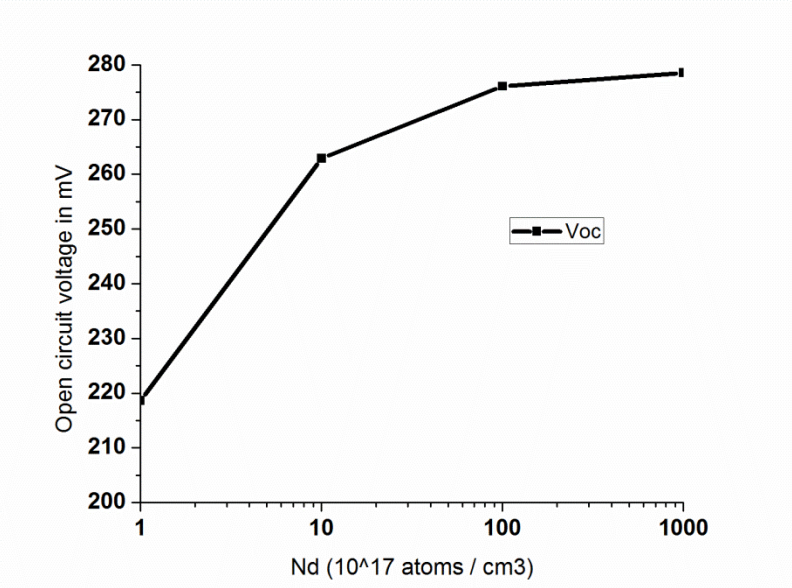


**Figure 4.15 Effect of emitter doping concentration on the open circuit voltage of standalone germanium solar cell.**

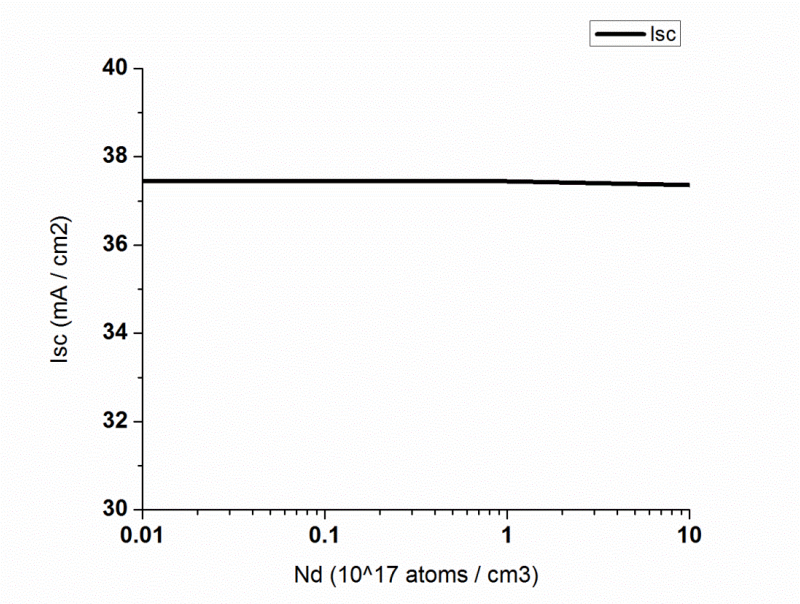


**Figure 4.16 Effect of emitter doping concentration on short circuit current of standalone silicon solar cell.**

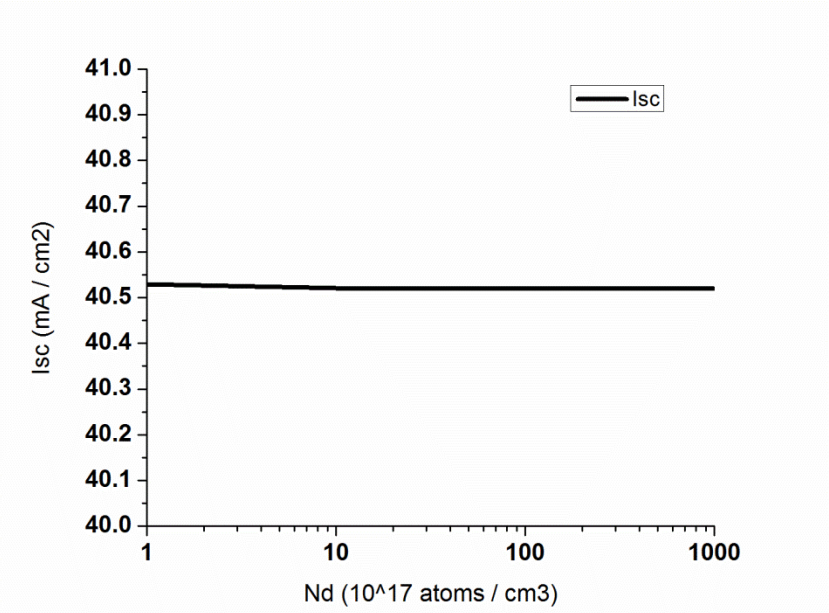


**Figure 4.17 Effect of emitter doping concentration on short circuit current of standalone germanium solar cell.**

It is seen from figures 4.14 and 4.15 that the open circuit voltage increases and saturates for germanium solar cell with increasing doping concentration, whereas the open circuit voltage is more or less saturated for silicon solar cells at lower doping level

already. So for the germanium device it is beneficial for the device to be processed to have an emitter concentration of greater than 1e18 atoms / $cm^3$ to achieve the higher open circuit voltage. This increase in voltage with increasing doping concentration could be due to Fermi energy level increase with increasing carrier concentration. But this does not explain silicon solar cells characteristics of no increase in open circuit voltage with doping concentration. It is seen from figures 4.16 and 4.17 that the short circuit current is independent of doping concentration. This shows that the variation in doping has not appreciably changed the width of the depletion region in any case so that the same number of photons are usefully absorbed.

#### *4.3.5.2 Effect of surface recombination*

Lower surface recombination rate is essential to make efficient PV devices. The rear surface passivation for silicon in bifacial solar cell is poor because of aluminum is not used to cover the entire solar cell which could lead the surface recombination rate to be as high as 1000 cm / sec. So in this study the effect of open circuit voltage and short circuit current for bifacial silicon solar cell for lower rear surface recombination rates was investigated to show the improvement possible with better rear passivation layer.

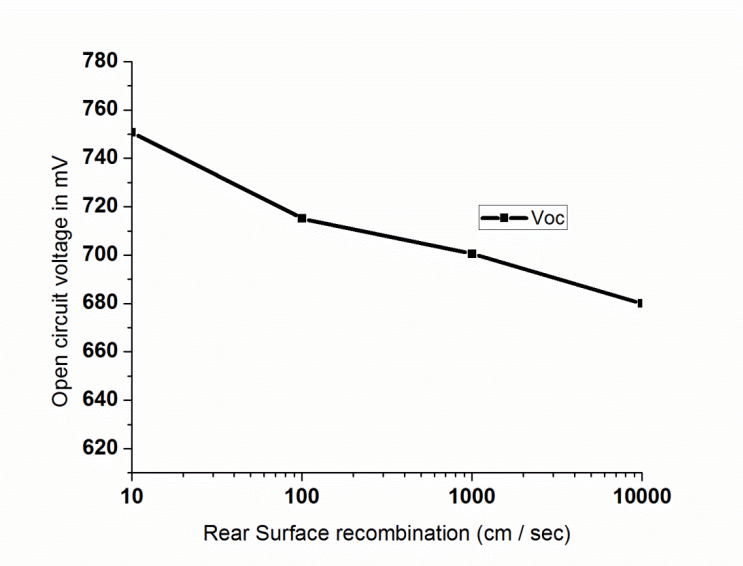


**Figure 4.18 Effect of rear surface recombination rate of silicon solar cell on its open circuit voltage.**

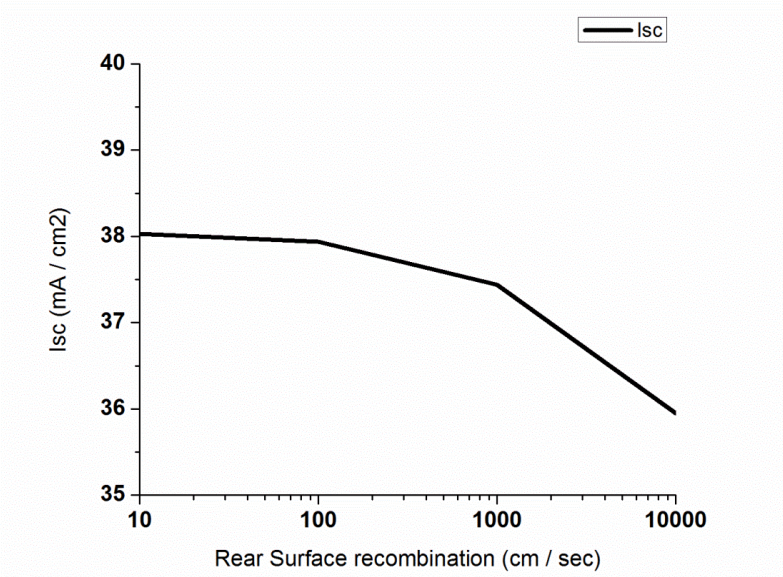


**Figure 4.19 Effect of rear surface recombination rate of silicon solar cell on its short circuit current.**

From the above figures 4.18 and 4.19 it is seen that the short circuit current improves by 1 mA / $cm^2$ and open circuit voltage improves by 42 mV as the surface recombination rate improves from 1000 cm / sec to 10 cm / sec, which is value for best in class all aluminum metal coated silicon layer.

Front surface passivation for germanium solar cells is also not optimal leading to high recombination rates as high as 4000 cm/sec as reported in section 4.3.4. In this study the effect of open circuit voltage and short circuit current for germanium solar cell for lower front surface recombination rates was investigated to show the improvement possible with better front passivation layer.

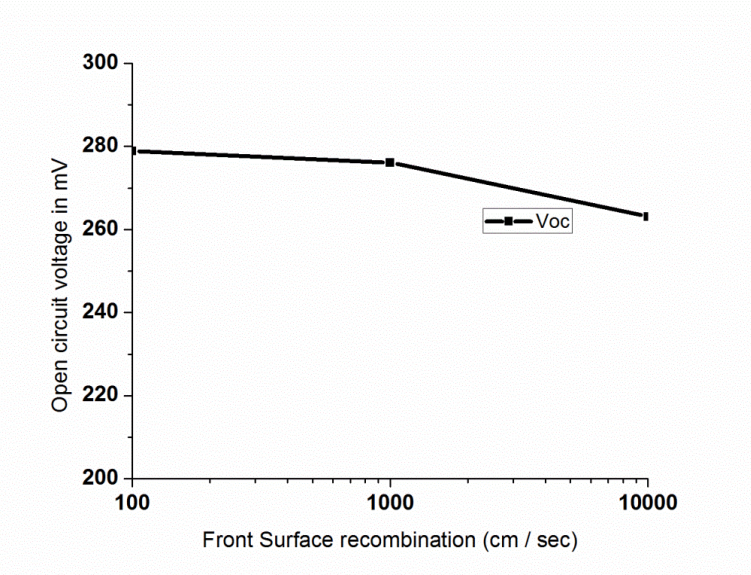


**Figure 4.20 Effect of rear surface recombination rate of germanium solar cell on its open circuit voltage.**

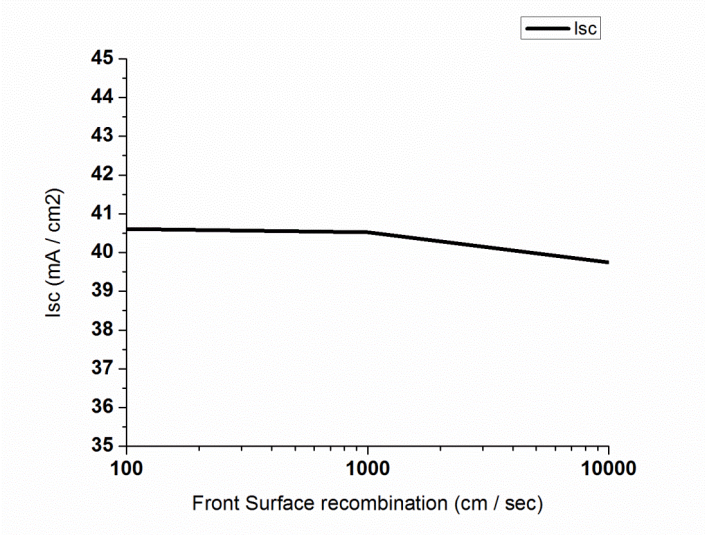


**Figure 4.21Effect of rear surface recombination rate of germanium solar cell on its short circuit current.**

From the above figures 4.20 and 4.21 it is seen that the short circuit current improves by 0.8 mA / $cm^2$ and open circuit voltage improves by about 10 mV as the surface recombination rate improves from 1000 cm / sec to 100 cm / sec.

## 4.4 Conclusion

A detailed simulation model of a mechanical 4 terminal silicon/germanium tandem device was developed. Optical losses in the tandem device were studied for AM 1.5 solar spectrum considering the absorption and reflection losses at the encapsulation and at the top solar cell. Electrical performance of stand-alone and tandem devices were analyzed and it was noted that a relative efficiency improvement of 11.42% to 12.45% can be obtained using tandem device architecture with present generation of devices. The improvement in efficiency is due to increased absorption at infrared wavelengths from 1100 nm to 1900 nm. Further improvements in efficiency are possible with development

of better front surface passivation and development of ohmic front contact for Germanium solar cells[2].

[2] This work has been published as "Optical and Electronic Simulation of Silicon/ Germanium Tandem Four Terminal Solar Cells", Journal of Solar Energy Engineering, DOI: 10.1115/1.4024744. Copyright 2013 ASME. It is reprinted here with permission.

# CHAPTER 5

## 5. Gallium Arsenide / Silicon Tandem Four Terminal Solar Cells

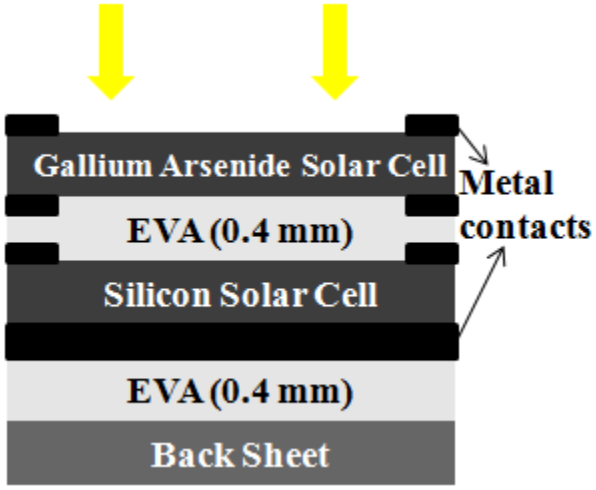


### 5.1 Background and Motivation

In this work we examine a mechanical tandem structure with gallium arsenide as the high band gap top cell, which has a band gap of 1.43 eV, and silicon at 1.11 eV as the low band gap cell. The theoretical efficiency of a gallium arsenide / silicon tandem device is calculated to be as high as 44% as shown in figure 5.1. The increase in ideal theoretical efficiency compared to single junction silicon device is 11%, so a low cost, mass manufactured and efficient solar cell targeting high band gap spectrum in tandem with the silicon solar cell would be an attractive alternative for densely populated regions where land-area may limit installations. The illustration of the device architecture is shown in figure 5.2.

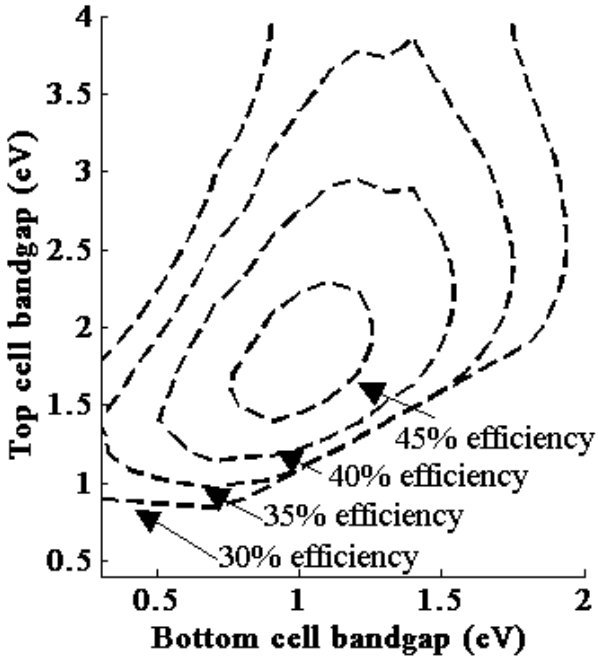


**Figure 5.1 Theoretical conversion efficiencies based on Shockley and Queisser limit for two junction (mechanical stack) solar cells under AM 1.5 solar spectrum.**

We report here on the electrical and optical simulations of this tandem structure, quantifying the various theoretical and practical loss mechanisms in the encapsulation, interfaces and in the device. Based on these studies we find that a practical efficiency improvement of over 5% may be attainable in this configuration with present technology.

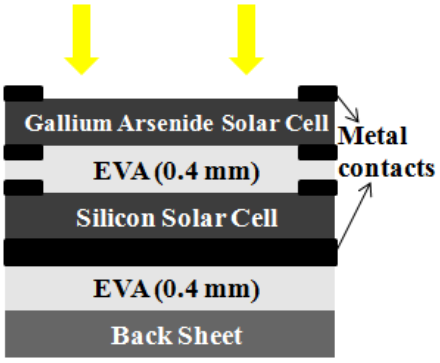


**Figure 5.2 Illustration of the proposed GaAs/Si tandem solar cell.**

## 5.2 Experimental - Device Modeling

The gallium arsenide solar cell was modeled as a thin film device with gallium indium phosphide window layer as shown in figure 5.3. Thin film gallium arsenide solar cells reduce the cost of the device by limiting the expensive gallium arsenide substrates. Such devices have been demonstrated before [104,105] and now Alta Devices Inc. [106] is working to commercialize these devices. The device was modeled with a heavily doped n-type and p-type region at the front and back surface to form good ohmic contacts with the external metal contact [107]. A 0.025 μm thick gallium indium phosphide window layer is modeled here to reduce the front surface recombination achieving a low rate of 200 cm/sec [108]. Individual doping concentrations and thickness of the various gallium arsenide solar cell layers were based on the device fabricated and characterized by Lee et al [109] with the emitter, base and back surface field being 0.15 μm, 3.5 μm and 0.075 μm thick, respectively, and the corresponding dopant concentrations being $1x10^{18}$, $2x10^{17}$, and $4x10^{17}$ atoms/$cm^3$ respectively. The electron and hole mobilities, conduction band and valence band density of states and radiative recombination rate used in the simulation were obtained from Plá et al. [108]. Electron affinity and dielectric permittivity were obtained from Griggs et al. [110]. A two layer antireflection coating of magnesium fluoride and zinc sulfide is added in the simulation model on top of the gallium arsenide solar cell to reduce the reflection loss. The optical properties for magnesium fluoride and zinc sulfide coatings were obtained from experiments reported by Siqueiros et al. [111]. The thicknesses of the bi-layer antireflection coatings were optimized for the device by optical simulations through finite-difference time-domain method using Lumerical. The optical properties for the gallium arsenide solar cell were

obtained from the optical constants handbook edited by Adachi [90]. The gallium arsenide solar cell device architecture that was simulated has metallic fingers as front and back contacts [112,113] thereby allowing infrared light to pass through the device and be absorbed at the silicon solar cell below.

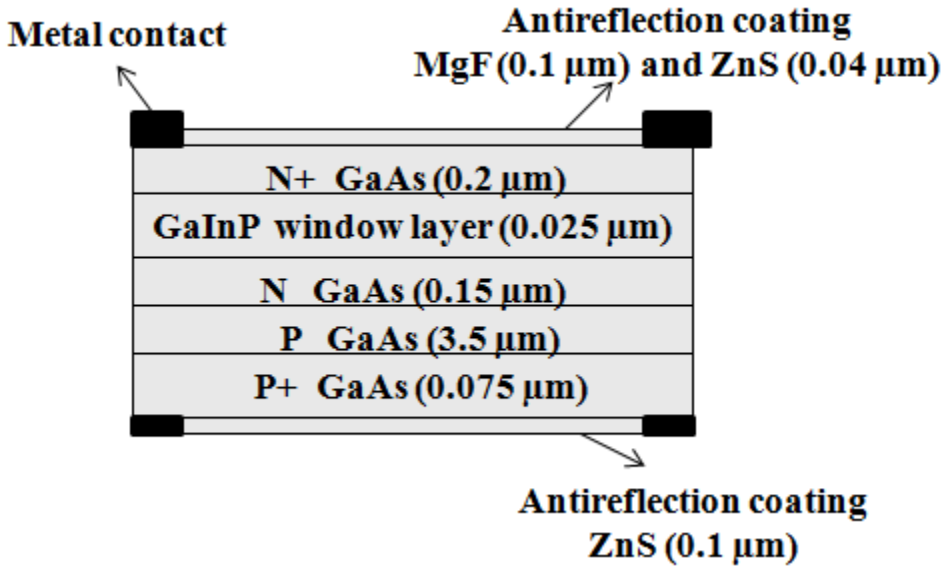


**Figure 5.3 Illustration of the modeled gallium arsenide solar cell.**

The silicon solar cell device used in the simulation was modeled as a conventional silicon solar cell with p-type wafer. It was modeled with a heavily doped n-type and p-type region at the front and back surface to form good ohmic contacts with the external metal contacts [114]. Since SiNx which is used as an antireflection coating on silicon solar cells is also known to form good surface passivation at the emitter layer, the surface recombination rate for the front surface used in the simulation was 50 cm/sec as reported by Aberle [88]. At the back surface due to aluminum back surface field the surface recombination rate is low and it is approximately 250 ~ 300 cm/sec [115]. Illustration of the modeled silicon solar cells are shown in figure 5.4. Electron affinity, dielectric

permittivity, conduction band and valence band density of states for the silicon layers used in the simulation were based on the simulation parameters reported by Zhao et al., [115] while electron and hole mobilities of silicon were obtained from the simulation parameters reported by Dwivedi et al., [117]. Aluminum back surface field properties used in the simulation were based on the modeling and simulation experiments done by Dao et al., [118]. The emitter and base regions are 0.5 µm and 199.5 µm thick with a uniform dopant concentration of $10^{17}$ atoms/$cm^3$. The silicon solar cell was incorporated with mid gap and band tail defect states based on the values reported by Zhao et al., [88]. The optical properties for the silicon solar cell were obtained from the optical constants handbook edited by Adachi [90].

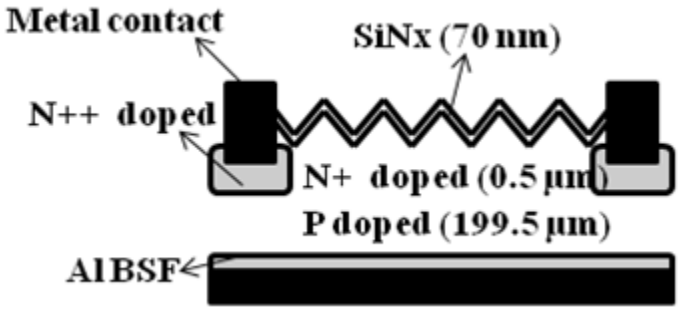


**Figure 5.4 Illustration of the modeled silicon solar cell.**

The electrical simulations of the modeled devices were performed using WxAMPS developed at University of Illinois [55]. WxAMPS a tool for numerical simulation of opto-electronic devices, is an updated version of AMPS 1-D which is widely used for solar cell device simulations [119]. It allows for modeling of various recombination effects due to mid-gap states, Shockley-Read-Hall (S-R-H), band-band and incorporation of surface recombination effects. The simulation works by solving for Poisson's, electron and hole continuity equations iteratively. Optical modeling and

simulation of the non-textured antireflective coated gallium arsenide device and the textured antireflective coated silicon device was done by finite-difference time-domain method using Lumerical. The thicknesses of the antireflective coatings were calculated through simulations, texturing of silicon solar cell was modeled based on the surface electron micrographs reported by Papet et al. [98]. Optical property data of the SiNx antireflection layer was obtained from plasma enhanced chemical vapor deposition (PECVD) experiments of Kang et al. [99] and the optical property data of ethylene vinyl acetate (EVA) encapsulation layer was obtained from experiments performed by French et al. [100]. Figure 5.5 and figure 5.6 provide a plot of extinction coefficient and refractive index against wavelength of light for all the materials used in the simulation.

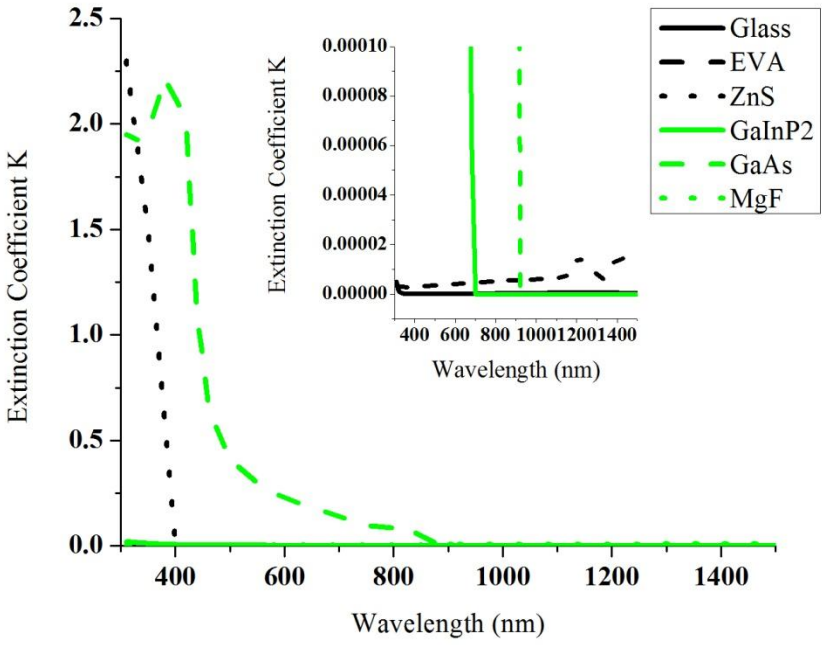


**Figure 5.5 Extinction Coefficient of the materials used in the tandem device.**

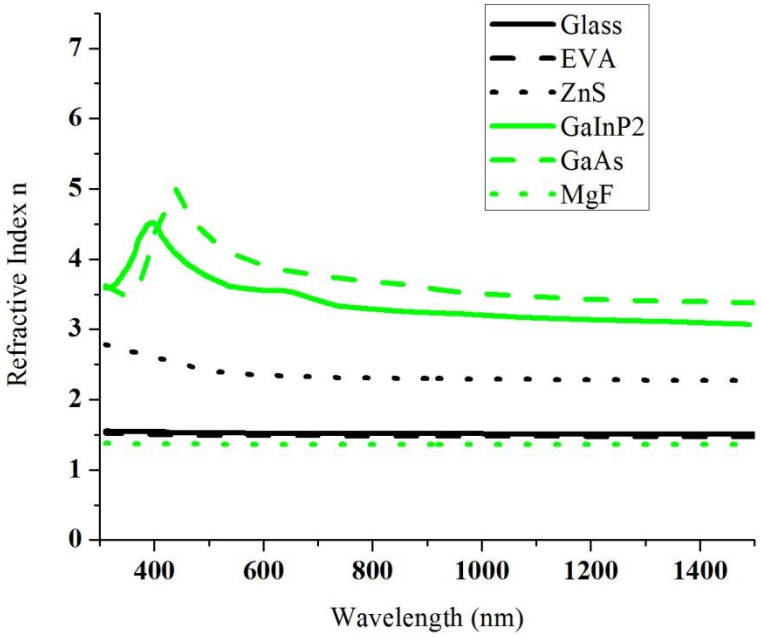


**Figure 5.6 Refractive Index of the materials used in the tandem device.**

## 5.3 Results & Discussion

### 5.3.1 Optical losses in the top (Gallium Arsenide) solar cell

Absorption and reflection losses at the magnesium fluoride and zinc sulfide anti-reflection coating layers for the gallium arsenide solar cell was calculated for AM 1.5 solar spectral intensity. The reflection loss at the air / MgF / ZnS / GaAs interface was on an average 2.6% for visible and infrared wavelengths up to 1117 nm i.e. the operating wavelengths of the tandem device, as shown in figure 5.7. Though reflection loss at UV wavelengths is high they correspond to a small part of the incident spectrum. Absorption loss due to zinc sulfide, shown in figure 5.7, is high at UV wavelengths because of the higher extinction coefficient near its absorption band edge which is at ~ 3.54 eV. However at visible and infrared wavelength regions absorption loss is very low, being on

average around 0.2%. Also absorption loss of magnesium fluoride is less at 0.59% for the operational wavelengths of the tandem device as seen in figure 5.7. The total light intensity available at gallium arsenide layer is 881.5 watts / sq.m or ~88% of the total AM 1.5 spectral intensity, i.e. ~ 12% of the incident light energy is lost due to absorption and reflection losses. The light spectrum available at the silicon layer is shown in figure 5.8.

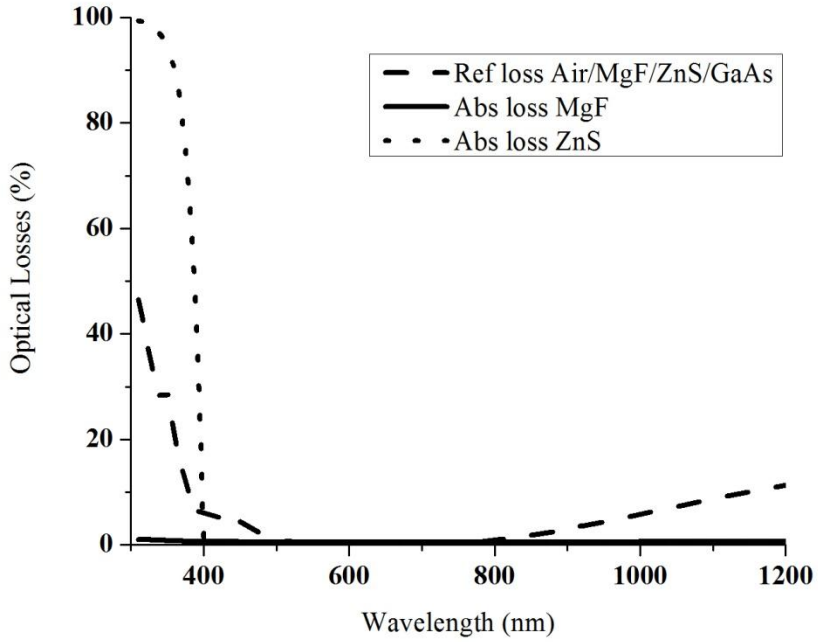


**Figure 5.7 Optical loss due to various layers in the top cell before the light gets absorbed by the gallium arsenide layer.**

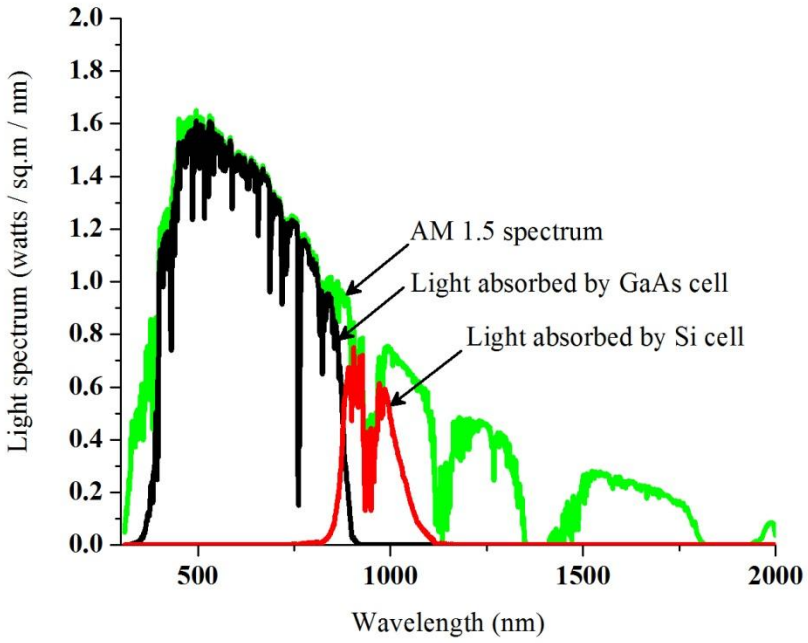


**Figure 5.8 Light spectrum incident on the tandem device, absorbed by gallium arsenide cell and silicon cell.**

### 5.3.2 Optical losses in the bottom (Silicon) solar cell

As shown above in figure 5.8, the longer wavelengths pass through the gallium arsenide device and reach the silicon device, yielding a total of 281 $W/m^2$ or ~ 28% of the AM 1.5 spectral intensity. In order to optically couple the gallium arsenide and silicon solar cells, the bottom layer of gallium arsenide cell is modeled with an antireflective coating of zinc sulfide and the top layer of silicon cell is modeled with silicon nitride antireflective coating. A 0.2 mm layer of EVA, an encapsulant, is incorporated between the cells. The ZnS thickness was increased to reduce the reflection loss at longer wavelengths relevant for the silicon cell. Figure 5.9 shows the optical loss percentages at the various layers of the bottom solar cell before the light strikes the textured silicon layer. The SiNx antireflection coating thickness was optimized for reducing the reflection

loss at the operation wavelengths of the bottom silicon solar cell therefore the reflection loss is higher for visible wavelengths as shown in figure 5.9. The reflection loss at GaAs/ZnS/EVA and EVA/SiNx/Si textured interfaces was on an average 0.3% and 1.54% respectively for operational wavelengths of the tandem silicon solar cell which is between 870 nm to 1200 nm. Absorption loss due to EVA, as shown in figure 5.9, is on average around 2.24% for operational wavelengths of the silicon solar cell. The total light intensity available at silicon layer is calculated to be 281 W/m$^2$ or ~ 28% of the total AM 1.5 spectral intensity.

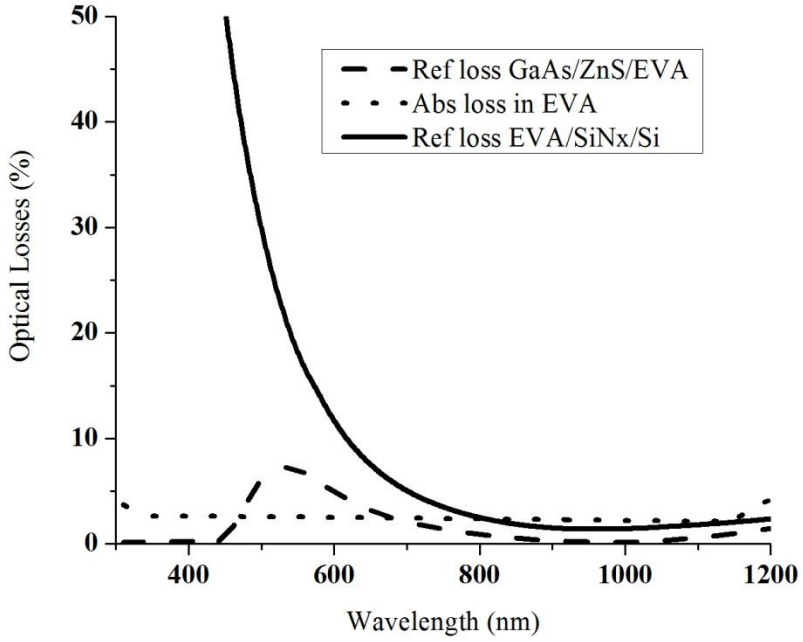


**Figure 5.9 Optical loss due to various layers in the bottom cell before the light gets absorbed by the silicon layer.**

Figure 5.10, illustrates the light intensities available at the gallium arsenide and silicon surfaces and the various optical losses in the optimized tandem device

architecture. The total front reflection and absorption losses before the light strikes the gallium arsenide surface is 119 W/m$^2$ or ~ 11.9% of the AM 1.5 spectral intensity. Light intensity incident on gallium arsenide surface, passing through gallium arsenide without absorption, optical loss at GaAs / Si interface, incident on silicon surface and light intensity incident on the back sheet are 881 W/m$^2$, 286.8 W/m$^2$, 13.6 W/m$^2$, 273.2 W/m$^2$ and 140 W/m$^2$ respectively.

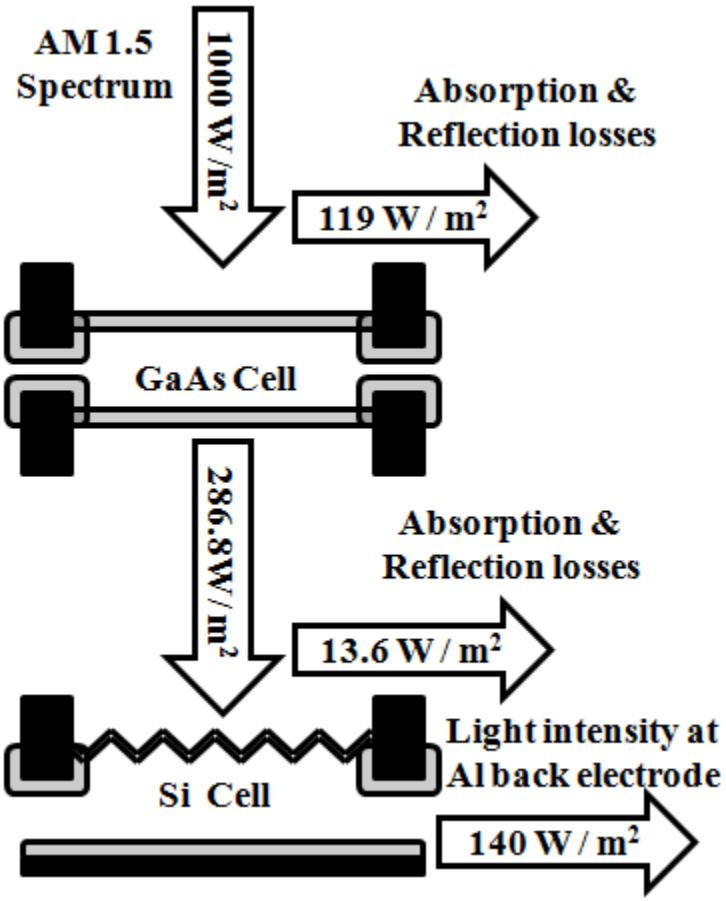


**Figure 5.10 Illustration of the light intensity available at gallium arsenide and silicon surfaces and the various optical losses in the device.**

### 5.3.3 Electronic Simulation of the Gallium Arsenide and Silicon Devices

Figure 5.11 shows the I-V curves of the simulated GaAs solar cell and the theoretical maximum (Shockley-Queisser limit) taking into account the optical losses in the device shown in figure 5.6. Electrical characteristics of the simulated gallium arsenide solar cell and the device fabricated at IMEC [113] are shown in table 5.1. The difference in power conversion efficiencies between simulated and experimental devices is only 0.2%. The I-V characteristics of the simulated stand-alone silicon device was calculated by removing the gallium arsenide solar cell from the top and using the full AM 1.5 spectrum as input into the silicon solar cell with silicon nitride antireflection coating and EVA encapsulation layer. Comparing the standalone silicon solar cell, tabulated in table 5.1, with the experimental device reported by Zhao et al. [24], difference in power conversion efficiency was 2.1%. There is a slight over estimate in the open circuit voltage and under estimate in short circuit current in the simulated gallium arsenide and standalone silicon solar cells. This may be due to lower recombination rate of the simulated device compared to the actual recombination rate leading to higher open circuit voltage. Also, lower light absorption and reflection than estimated in the anti-reflection coatings and encapsulation layer could lead to lower short circuit current in the simulated device. Still the simulated gallium arsenide and standalone silicon solar cells demonstrate a good match with the experimental devices. The silicon tandem device was simulated with a modified light spectrum taking into account the light absorption and reflection at the top gallium arsenide solar cell and at the encapsulation above the silicon solar cell, the light intensity available at the silicon surface is 240 $W/m^2$. The I-V characteristics of the simulated and theoretical maximum Shockley - Queisser limit for tandem silicon solar

cells are shown in figure 5.11. The power conversion efficiency of silicon tandem device was calculated to be 5.13% (referenced to the full AM 1.5 intensity) and the electrical characteristics are tabulated in table 5.1. Thus, the overall tandem structure can provide a combined efficiency of 28.5%, an impressive value. The relative increase in efficiency of the GaAs / Si tandem stack solar cell, compared to standalone gallium arsenide solar cell efficiency can be as high as 22%.

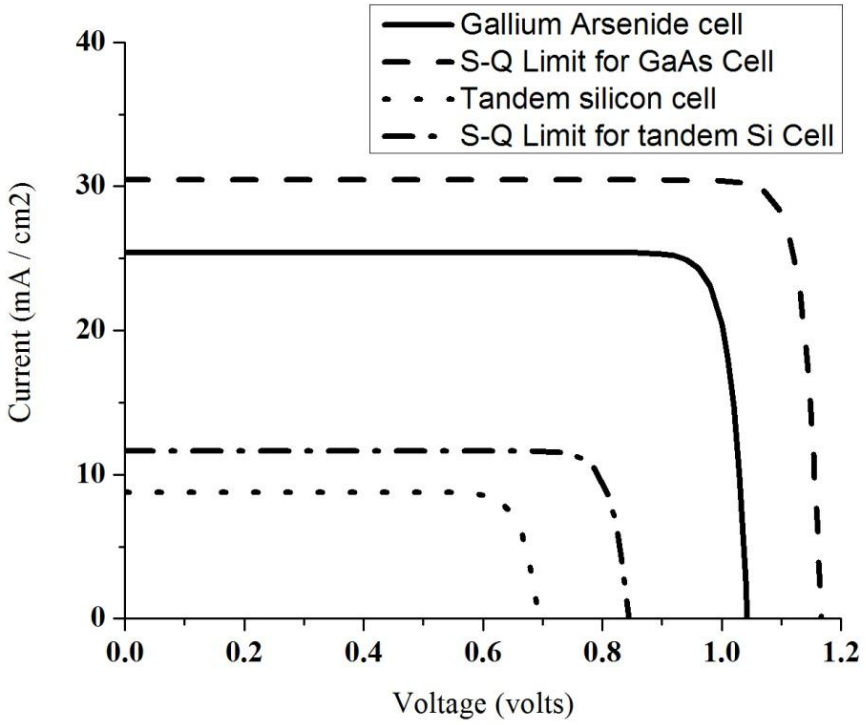


**Figure 5.11 Simulated and theoretical maximum current-voltage curves for silicon solar cell in tandem with gallium arsenide solar cell.**

**Table 5.1 Current-voltage characteristics of the simulated and experimental devices.**

| Simulated Data | Voc in mV | Jsc in mA/cm2 | FF in % | Efficiency in % |
|---|---|---|---|---|
| GaAs solar cell | 1042 | 25.42 | 88.4 | 23.4 |
| Standalone silicon cell | 720 | 37 | 84.9 | 22.6 |
| Tandem silicon solar cell | 692 | 8.8 | 84.2 | 5.13 |
| Experimental cell efficiencies (from literature) | | | | |
| GaAs cell (Flamand et al., 2009) [113] | 1037 | 27.7 | 80.8 | 23.2 |
| Standalone silicon cell (Zhao et al. 1999) [24] | 704 | 42 | 83.5 | 24.7 |

Voltage, current and power loss percentages of the gallium arsenide and tandem silicon solar cell were calculated by comparing the simulated device characteristics with Shockley-Queisser values and the calculated loss percentages are tabulated in table 5.2. The higher current, voltage loss and hence higher power loss for tandem silicon solar cells compared to gallium arsenide solar cell is due to lower back surface and bulk recombination rate in gallium arsenide solar cell compared to the silicon solar cell.

**Table 5.2 Electrical loss in the devices.**

| Device | 1 - (Voc simulated / Voc Shockley-Queisser) (Voltage loss in %) | 1 - (Jsc simulated / Jsc Shockley-Queisser) (Current loss in %) | 1 - (Pmax simulated / Pmax Shockley-Queisser) (Power loss in %) |
|---|---|---|---|
| GaAs cell | 10.1 | 16.4 | 26.4 |
| Tandem Si cell | 18 | 24.5 | 39.2 |

Figure 5.12 provides the quantum efficiencies of gallium arsenide and silicon solar cells determined in the simulation. Note that the interface reflectance losses have already been applied, above in sections 5.3.1 and 5.3.2., so figure 5.12 is the external efficiency for the photons that are not reflected. Gallium arsenide solar cell has lower quantum efficiency in UV to 500 nm wavelength because of the light absorption in the zinc sulfide antireflection and gallium indium phosphide window layers. Silicon because of its indirect band gap is known to have low absorption near its band edge as seen in figure 5.12. So a further improvement in efficiency of tandem silicon solar cell may be possible by developing silicon solar cell architectures with improved infra-red light absorption properties. This would not only reduce the silicon consumption in the device and also increase the device efficiency. Figure 5.11 shows the IV curves calculated in the Shockley-Queisser limit for tandem silicon cell with gallium arsenide solar cell, the maximum possible efficiency for the tandem silicon cell is calculated to be 8.35%.

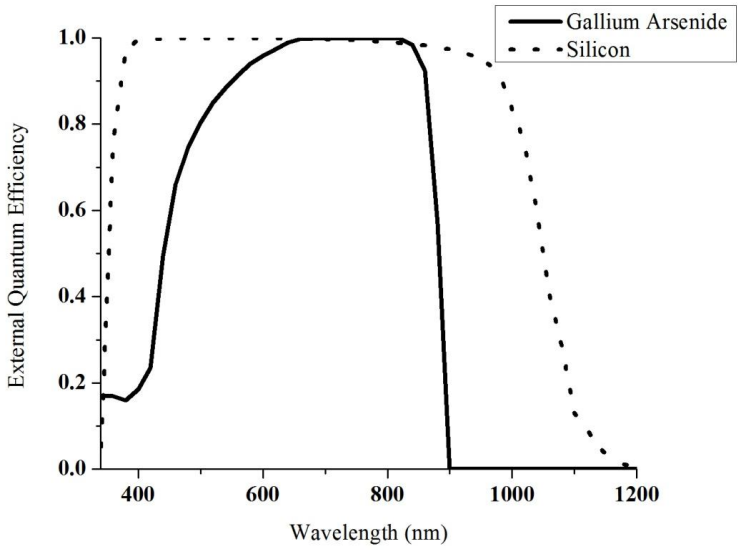


**Figure 5.12 External Quantum Efficiency of simulated gallium arsenide and silicon solar cells.**

### 5.3.4 Sensitivity analysis of gallium arsenide solar cells

In this section, the effect of process parameters during manufacturing of GaAs device and their effect on solar cell open circuit voltage and short circuit current are analyzed. Also, the effect of improved passivation layer, which reduces front surface recombination, on solar cell electrical characteristics was analyzed.

#### *5.3.4.1 Effect of emitter doping concentration*

The emitter doping concentration was varied from 1e15 to 1e18 atoms / $cm^3$. Figures 5.13 and 5.14 show variations in open circuit voltage and short circuit current for different emitter doping concentrations in standalone GaAs solar cells.

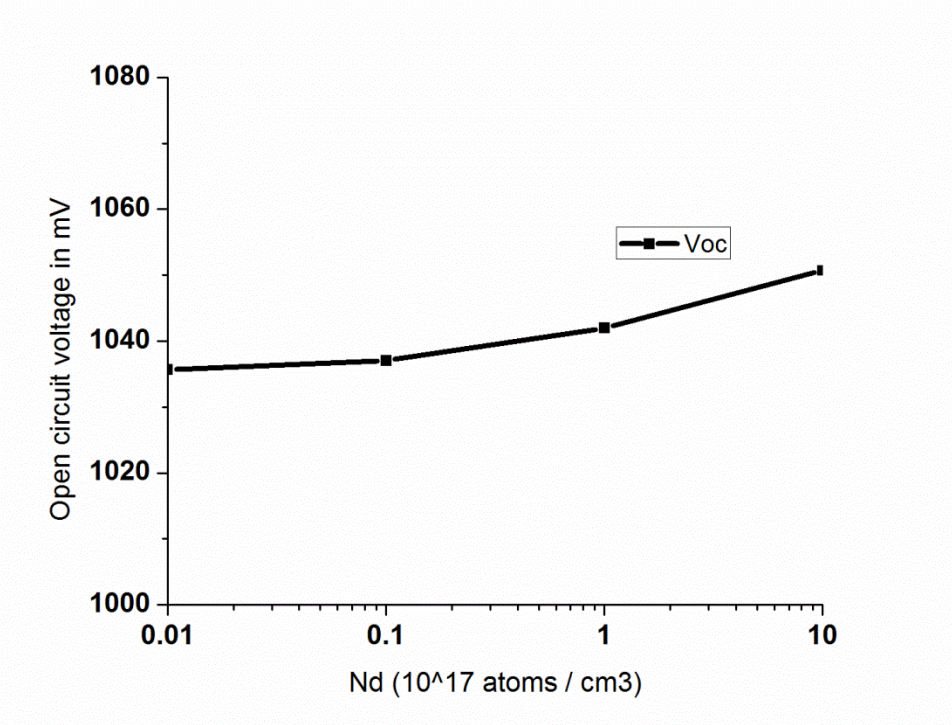


**Figure 5.13 Effect of emitter doping concentration on the open circuit voltage of standalone GaAs solar cell.**

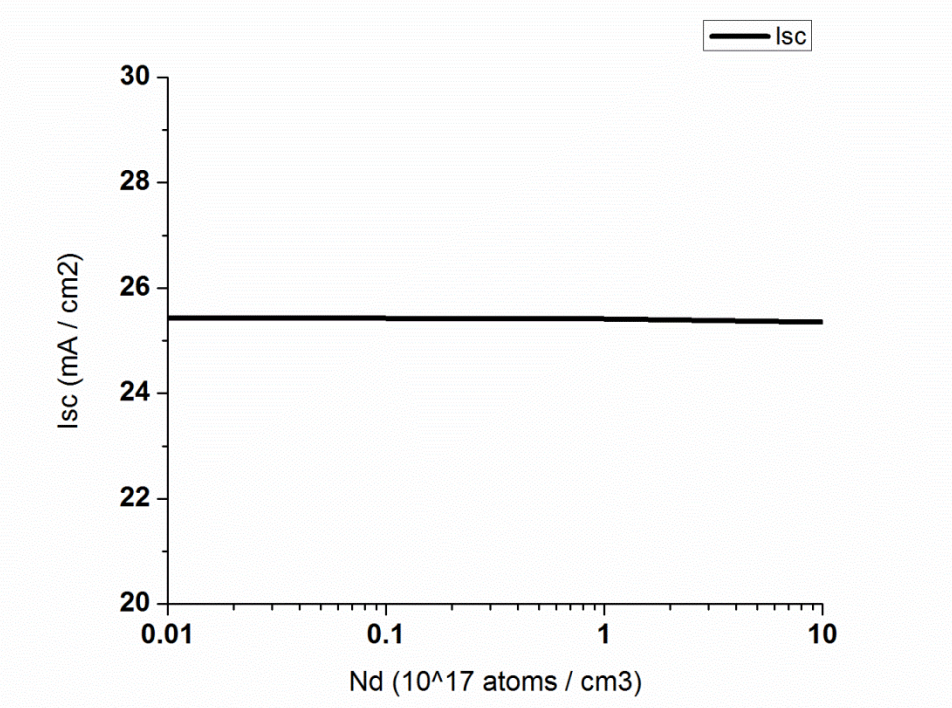


**Figure 5.14 Effect of emitter doping concentration on short circuit current of standalone GaAs solar cell.**

It is seen from figure 5.1 that the open circuit voltage increases for GaAs solar cell similar to germanium solar cell with increasing doping concentration as mentioned in section 4.3.5. This increase in band gap with increasing doping concentration could be due to the expected Fermi energy level increase with increasing carrier concentration. It is seen from figure 5.1 that the short circuit current is independent of doping concentration as seen in section 4.3.5 for silicon and germanium solar cells. So the doping level change has not effectively reduced the active absorption zone in the p-n junction region.

#### *5.3.4.2 Effect of surface recombination*

Low surface recombination rate is essential to make highly efficient PV devices. The front surface passivation for GaAs solar cell is done by GaInP which keeps surface

recombination down to values of 250 ~ 300 cm / sec. So in this study the effect of open circuit voltage and short circuit current for GaAs solar cell for progressively lower front surface recombination rates was investigated to show the improvement possible with better passivation.

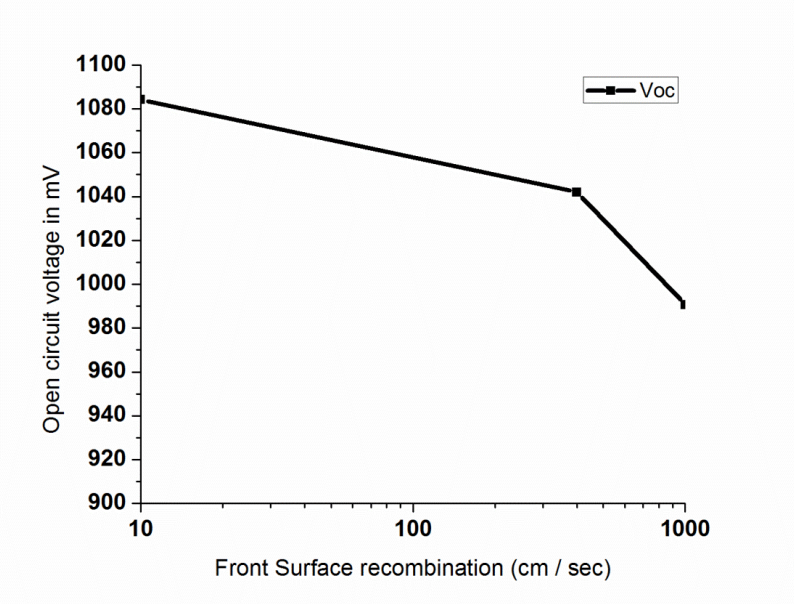


**Figure 5.15 Effect of front surface recombination rate of GaAs solar cell on its open circuit voltage.**

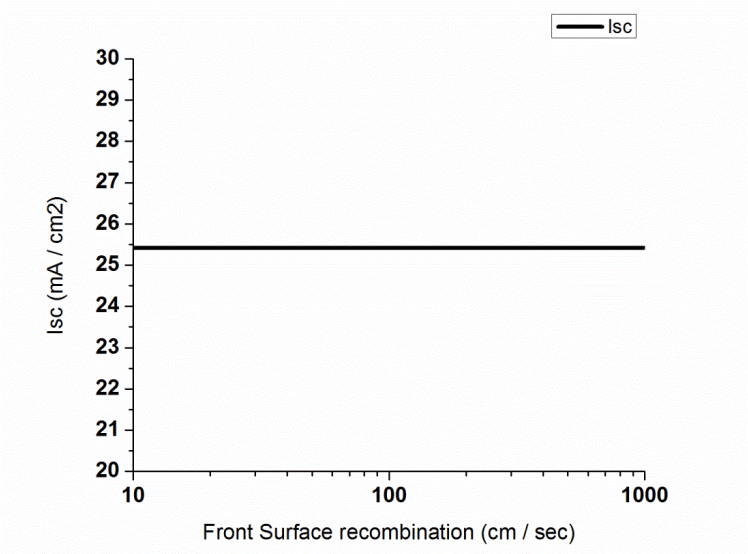


**Figure 5.16 Effect of front surface recombination rate of GaAs solar cell on its short circuit current.**

From the above figures 5.15 and 5.16 it is seen that the open circuit voltage improves by about 30 mV as the surface recombination rate improves from 300 cm / sec down to 10 cm / sec.

## 5.4 Conclusion

A detailed quantitative simulation model of a mechanical gallium arsenide / silicon tandem device was developed. Optical losses in the tandem device were studied for AM 1.5 solar spectrum considering the absorption and reflection losses at the antireflection coatings and encapsulation layers. Electrical performance of stand-alone and tandem devices was analyzed and it was noted that 28.5% efficient tandem devices could be made with present generation of device technology. The improvement in efficiency is due to increased absorption at infrared wavelengths from 870 nm to 1200 nm. Further improvements in efficiency approaching 30% may be possible with more optimized nano-structured silicon surface features that are tuned to emphasize light scattering further into the relevant near infra-red spectral region (between 800 and 1200 nm)[3].

[3] This work has been published as "Optical and Electronic Simulation of Gallium Arsenide / Silicon Tandem Four Terminal Solar Cells", Solar Energy. Copyright 2013 Elsevier Ltd. http://dx.doi.org/10.1016/j.solener.2013.07.033 It is reprinted here with permission.

# CHAPTER 6

## 6. Discussion

The range of possible absorber materials, with their band gaps and their efficiencies for the mechanical tandem device with silicon as a component device, are shown in figure 1.12. Intrinsic efficiencies greater than 45% are feasible for top cells having a band gap of 1.5 eV ~ 2.2 eV. However high band gap cells have not received much scientific attention since most of the developed PV devices are targeted towards single junction having an ideal band gap 1.1 ~ 1.4 eV. Table 6.1 is a compilation of PV device performances from literature [16,61,99,120-121]. From table 6.1. it is seen that CZTS, DSSC (sensitized with N719 and $CH_3NH_3PbI_3$), organic solar cells (OPV) (PCBM-P3HT), CuGaSe, a-Si and GaInP devices all have band gap above 1.5 eV. Of these only DSSC (sensitized with $CH_3NH_3PbI_3$) [120] has so far yielded an efficiency of 15% [120].

In this chapter an investigation on the present state of the art PV devices with a focus on high band gap devices is done to understand the limits of their electrical performance. This is followed by discussion on developing efficient tandem solar cells.

**Table: 6.1 Comparison of different PV devices reported in literature.**

| Material | Band gap (Eg) in eV | Voc in volts | Isc in mA / sq.cm | Power conversion efficiency |
|---|---|---|---|---|
| **Germanium** | 0.67 | 0.268 | 46.4 | 7.8 |
| **Silicon** | 1.12 | 0.706 | 42.7 | 25 |

| | | | | |
|---|---|---|---|---|
| **CIGS** | 1.16 | 0.74 | 35.4 | 20.3 |
| **CZTSSe** | 1.21 | 0.516 | 28.6 | 9.7 |
| **GaAs** | 1.43 | 1.122 | 29.68 | 28.8 |
| **CdTe** | 1.44 | 0.903 | 26.95 | 18.7 |
| **CZTS** | 1.5 | 0.61 | 17.9 | 6.77 |
| **DSSC($CH_3NH_3PbI_3$)** | 1.55 | 0.993 | 20 | 15 |
| **Organic PV (P3HT-PCBM)** | 1.65 | 0.82 | 14.7 | 6 |
| **DSSC (N719)** | 1.65 | 0.744 | 22.47 | 11.9 |
| **CuGaSe** | 1.7 | 0.971 | 16.23 | 9.37 |
| **a-Si** | 1.73 | 0.88 | 21.5 | 6.7 |
| **GaInP** | 1.87 | 1.22 | 14 | - |

## 6.1 Voltage loss of different PV devices

Figure 6.1 plots the ratio of the open circuit voltage to the band gap of the material for various PV devices. The ratio of $V_{oc}$ / $E_g$ provides information about the energy cost involved in generating electron-hole pairs in the device, i.e. voltage loss in the device. This ratio connects the absorption effect (only photons with $E > E_g$ are absorbed) and the power delivery effect (the excited states always have time to thermalize to the band edges before being swept to their respective contacts). It is observed that for Si, CIGS, GaAs, CdTe, DSSC (sensitized with $CH_3NH_3PbI_3$) and GaInP based PV devices the ratio of $V_{oc}$ / $E_g$ is more than 60% indicating these devices were able to retain more than 60% of their band gap value as their open circuit voltage. GaAs based devices had the highest $V_{oc}$ / $E_g$ ratio of 78%. But GaInP generates the highest open circuit voltage at 1.22 volts as shown in table 6.1 and figure 6.2, because of its high band

gap of 1.87 eV and it has a $V_{oc}$ / $E_g$ ratio of 65%. Of the list of devices reported in table 6.1 only DSSC (sensitized with $CH_3NH_3PbI_3$) and GaInP based PV devices have a band gap of >1.5 eV and still have $V_{oc}$ / $E_g$ ratio of 65%.

CZTS, Organic PV (OPV), DSSC (sensitized with N719), a-Si, and CuGaSe have a low $V_{oc}$ / $E_g$ ratio of 43% ~ 57% indicating high voltage loss, with OPV, a-Si and CuGaSe having 50%, 50% and 57% $V_{oc}$ / $E_g$ ratio respectively.

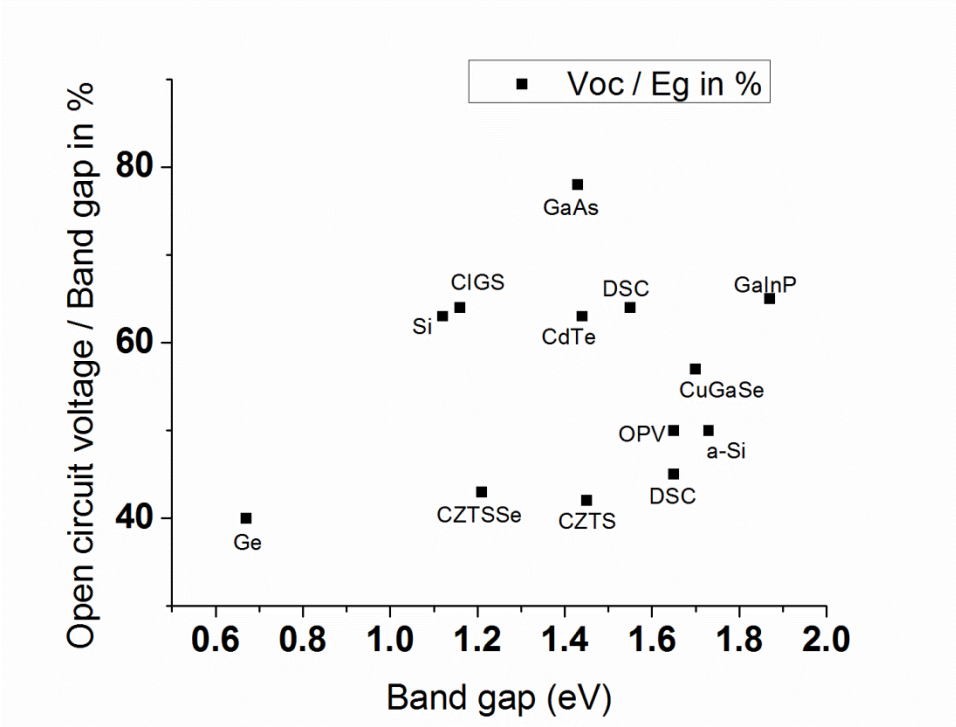


**Figure 6.1 Ratio of the open circuit voltage and band gap of the material for various PV devices.**

Si, CIGS, CdTe, DSSC and GaAs based devices have been researched extensively in the last 2 decades leading to technology improvements enabling low voltage loss in these devices. CZTS based devices are relatively new and perhaps more opportunities exist in increasing Voc / Eg ratios to 60%. OPV's have an order of magnitude higher exciton binding energy [16] so some of the potential energy is used to facilitate charge

separation. So there may be limitations for improving OPV's Voc / Eg ratio. a-Si has been studied extensively in the past but they still have low Voc / Eg ratios, which may be due to large defect density in the device inherent to the amorphous structure.

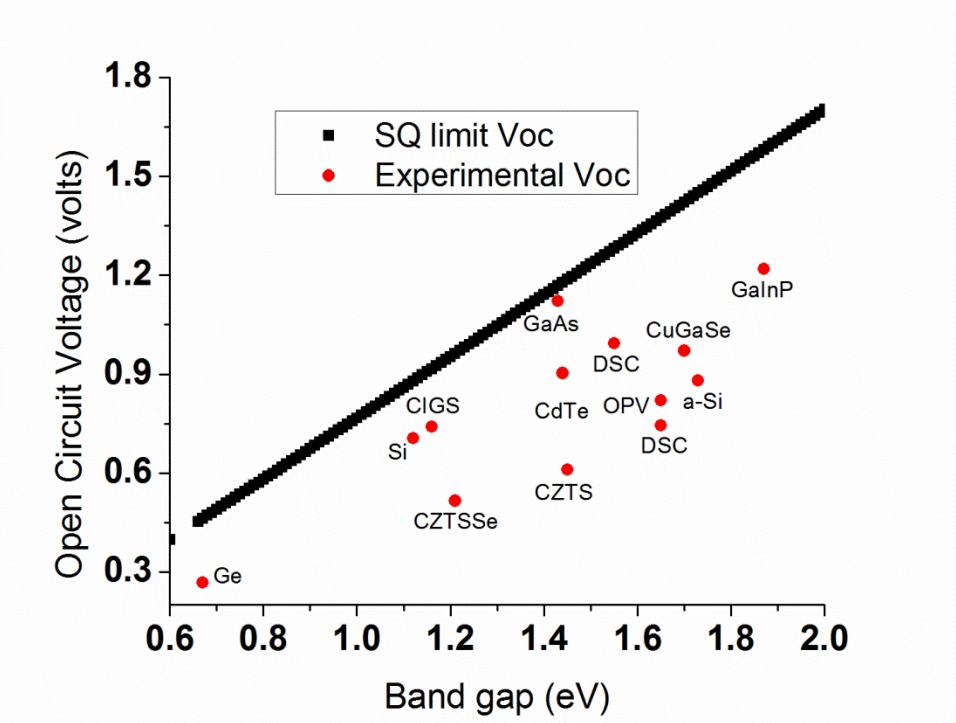


**Figure 6.2 Plot of open circuit voltage for different PV devices and their SQ limit for open circuit voltage.**

GaAs is a direct band gap semiconductor compared to Si which is an indirect band gap material, this may explain lower voltage loss in GaAs device because of its reduced thickness thereby reducing bulk recombination. Presently $V_{oc}$ of GaAs is very close to the SQ limit as seen in figure 6.2., indicating a road block for future improvement in open circuit voltage for GaAs solar cell. But a lot of improvement in voltage may be possible for CZTS devices. In addition, many other chalcogenides (cadmium sulfide and copper tin sulfide) have band gaps of more than 1.5 eV (making

them attractive for the tandem stacks). However, very little is known about their device performances, so it would be necessary to investigate those materials.

### 6.2 Current loss of different PV devices

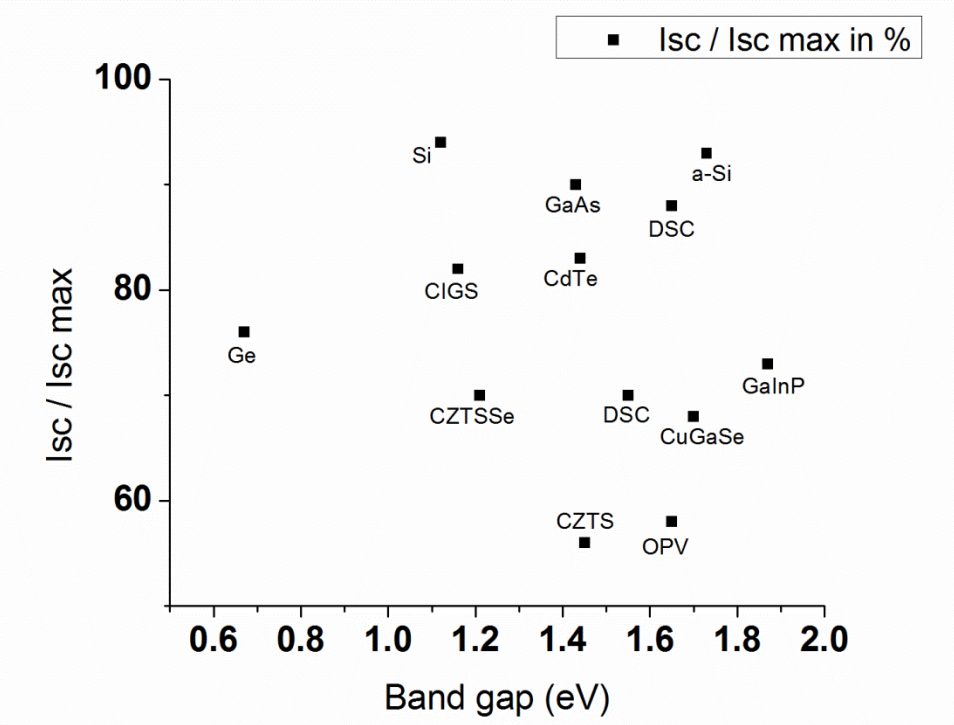


**Figure 6.3 Ratio of short circuit current with the theoretical maximum for short circuit current for various PV devices.**

Figure 6.3 plots the ratio of the short circuit current with theoretical maximum for short circuit current for various PV devices. The ratio of $I_{sc}$ / $I_{sc}$ max indicates current loss within the device. The short circuit currents in Si, a-Si, GaAs are close to 94%, 93% and 90% of the theoretical limit respectively. The ratio is above 80% for CIGS, CdTe and DSSC (sensitized with N719) devices. All of the above devices are inorganic devices exception being DSSC, which is the only organic / inorganic hybrid device. CZTS and OPV are the only two devices having $I_{sc}$ / $I_{sc}$ max ratio below 60%. CZTS has higher

current loss which is blamed on its low electron mobility leading to higher recombination in the long wavelength region [61]. As mention in section 6.1. CZTS devices are relatively new, so future developments in CZTS doping and material development may help in improving its device performance. OPV has a different charge transport mechanism because of its higher exciton binding energy and they are limited by low exciton diffusion length of ~ 10 nm [16] and low carrier mobility [16]. Figure 6.4 plots the short circuit current and the theoretical maximum for short circuit current for various PV devices. It can be seen that for Si, a-Si, DSSC (sensitized with N719) and GaAs the short circuit current is close to its theoretical limits, of which DSSC and a-Si are the only materials having a band gap of >1.5 eV.

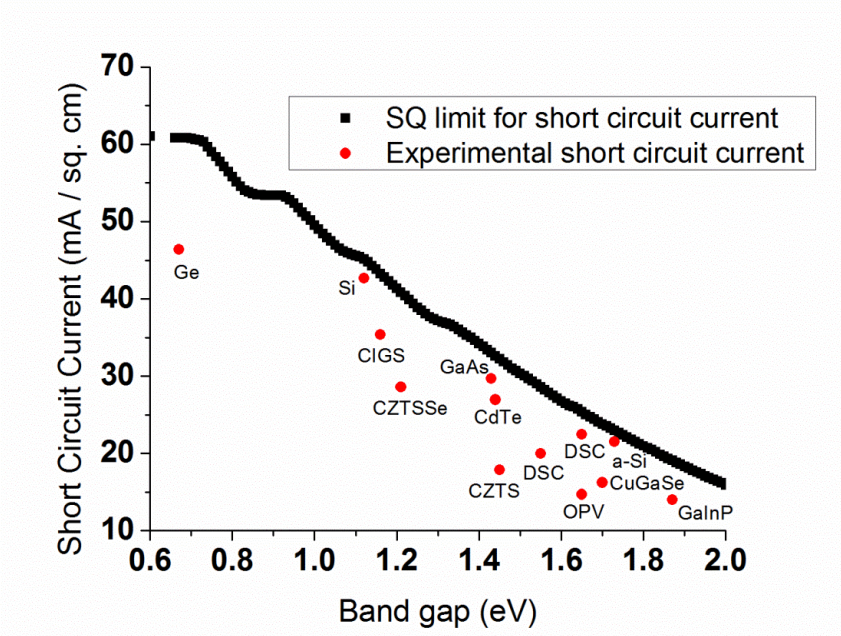


**Figure 6.4 Plot of short circuit current for different PV devices and their SQ limit for short circuit current.**

### 6.3 Tandem Devices

It is seen from figure from 1.12 tandem devices of theoretical efficiency greater than 45% are feasible with silicon as the bottom cell and top cells having band gaps between 1.5 eV ~ 2.2 eV, with a maximum of 47% efficiency between 1.8 eV ~ 2 eV. Efficiencies about 38% could be obtained for silicon as a top cell configuration with bottom cells having a band gap of 0.65 eV ~ 0. 75 eV. So there is a wide region of band gaps that could be utilized for making these tandem devices, as long as they are paired effectively to share the spectral regions well.

**Table 6.2 Efficiencies possible for mechanical tandem solar cells using present generation of top cells with silicon as the bottom cell.**

| Top cell | Best cell efficiency in % | SQ limit for top cell in % | SQ limit for tandem efficiency in % | Bottom Si cell efficiency in % (Total tandem efficiency) | | |
|---|---|---|---|---|---|---|
| | | | | 80% light transmission below the band gap of top cell | 60% light transmission below the band gap of top cell | 40% light transmission below the band gap of top cell |
| GaAs | 28 | 34 | 44 | 5.82 (31.82%) | 4.36 (30.36%) | 2.91 (28.91%) |
| GaAs | 23.4 (device modeled in chapter | 34 | 44 | 5.13 (results from chapter 5) (28.53%) | | |

| | | | | | | |
|---|---|---|---|---|---|---|
| | 5) | | | | | |
| DSSC($CH_3NH_3PbI_3$) | 15 | 33 | 45.2 | 7.09 (22.09%) | 5.32 (20.32%) | 3.55 (18.35 %) |
| OPV | 9 | 31.6 | 46.3 | 8.52 (17.52%) | 6.39 (15.39%) | 4.26 (13.26 %) |
| DSSC(N719) | 11.9 | 31.6 | 46.3 | 8.52 (20.42%) | 6.39 (18.29%) | 4.26 (15.16 %) |
| CuGaSe | 9.37 | 30.7 | 46.6 | 9.23 (18.6%) | 6.92 (16.29%) | 4.61 (13.98 %) |
| a-Si | 6.7 | 30.3 | 46.8 | 9.59 (16.29%) | 7.19 (13.89%) | 4.79 (11.49 %) |
| GaInP | - | 27.6 | 47.1 | 11.34 | 8.50 | 5.67 |
| Si top cell (bottom cell is Ge) | 22 | 33 | 38 | 2.54 (results from chapter 4) (24.54%) | | |

Table 6.2 lists the efficiencies possible under tandem configuration using present generation of high band gap cells with silicon as the bottom cell. It is seen from the above table that for high band gap top cell apart from GaAs, DSSC is the only device which yields above 20% efficient tandem solar cells. But the combined tandem efficiency with DSSC top cell is still slightly lower than best performing standalone silicon solar cell. This is because of high current loss in DSSC device due to recombination as shown in figure 6.3.

Though bifacial GaAs and DSSC PV devices [110, 122] were developed to allow below band gap wavelength light to pass through the device, very little work exists in the literature about other bifacial high band gap solar cells. This would necessitate developments in transparent conductors for chalcogenide and OPV based high band gap solar cells. Also as detailed in sections 6.1 and 6.2 more developments are required to reduce the voltage and current loss in CZTS, a-Si and OPV solar cell to make them better candidates for tandem devices.

**Table 6.3. List of material properties and their significance for selecting candidate high band bap top cells to make tandem devices of greater than 30% efficiency.**

| Property | Significance to get > 30% efficiency |
|---|---|
| Top cell band gap - 1.5 eV to 2.1 eV | Very important |
| Top cell refractive index match with bottom silicon cell | Not very important (could be matched with anti-reflection coatings) |
| Low front and back surface recombination | Very important |

| | |
|---|---|
| for high band gap top cell | |
| Ohmic front and back contacts for high band gap top cell | Very important |
| Metallic grid like back contact for the top cell | Very important |
| High minority carrier lifetime and high minority carrier mobility | Very important |
| Low exciton binding energy | Very important |
| Indirect or direct band gap semiconductor | Both could be used as light absorber |
| Ability to manufacture as thin films | Not very important |
| Thermal expansion of the top cell compared with the bottom silicon cell | May be important |

Table 6.3 lists some of the essential properties for potential high band gap devices and their relative significance in order to make tandem devices greater than 30%. As seen in table 6.3, it is very important for the high band gap cell to have high minority carrier life time, high minority carrier mobility, low exciton binding energy, good surface passivation, with ohmic front and back contacts. Since p-type TCO development has been very challenging it may be important to have metallic grid like contacts at the back to enable below band gap light to pass through the device. The refractive index mismatch of the high band gap cell with the bottom silicon cell or the front ambient atmosphere could be matched with antireflection coatings. Thermal expansion mismatch between the high band gap cell and silicon cell may damage the device during the life time of the tandem device so further studies are required to quantify the magnitude of mismatch which could be allowed to make reliable tandem devices.

# CHAPTER 7

## Conclusion and Future work

In this thesis the feasibility of mechanical tandem solar was investigated. Two different configurations of tandem solar cells were analyzed. In the first configuration silicon was used as the top cell and germanium as the bottom cell. In this case it was noted that 16% of the AM 1.5 spectrum passes through the silicon solar cell and is incident on the germanium solar cell. The electrical efficiency of the Si / Ge tandem configuration improved by 12% compared to standalone silicon solar cell devices. The second configuration was a tandem with GaAs as the front and Si as the back. For this stack about 28% of the AM 1.5 spectrum passes through the GaAs and is incident on the silicon solar cell. The electrical performance of the GaAs / Si tandem device improved by 22% compared to stand alone GaAs solar cells.

Two candidate materials for the top cell in the mechanical tandem device were developed, namely DSSC and CZTS. Flexible DSSC's with SS mesh electrodes coated with dense titania were fabricated and tested. This resulted in a 63% improvement in solar power conversion efficiency compared with uncoated SS meshes. Also the series resistance of SS mesh electrode based DSSC devices was much lower (at 13 ohms compared to 33 ohms) than for FTO electrode based DSSC device. Solution deposited CZTS was also investigated as a candidate material for the top cell in the tandem device. The CZTS films had a band gap of ~1.5 eV and had absorption coefficient greater than $10^4$ $cm^{-1}$. The deposited films composition was determined to be copper deficient and zinc rich which has been known to provide high efficiencies.

Finally a comparative analysis was made of present day high band gap solar cells' open circuit voltage and short circuit current. It was observed that only DSSC (sensitized with $CH_3NH_3PbI_3$) and GaInP were the only high band gap devices having output voltages relatively close to their known band-gap values. CZTS and OPV based devices both have high current and/or voltage losses making them unsuitable for tandem devices. So, improvement in the performance of high band gap solar cells is essential for future development of efficient tandem devices.

If high-output-voltage wide-band-gap devices are developed then tandem devices having efficiencies close to 45% may be possible using top cells with a band gap of 1.5 eV ~ 2.2 eV using conventional silicon solar cells as the bottom cells. Efficient high band gap solar cell devices need to be researched and developed as potential strategies to improve tandem device efficiencies beyond 30%. DSSC's are still a potential candidate for tandem devices because of its ease of manufacture and flexibility in device assembly. They also can have low voltage loss comparable to silicon but they presently have high current loss due to high recombination rates at the electrolyte / dye interface. So, improvement in electrolytes and better understanding of the recombination process will be helpful for developing efficient DSSC devices in the future. Other potential chalcogenides solar cells should be explored as candidate materials for efficient high band gap solar cells. Bifacial DSSC solar cells have been developed before but for other high band gap PV devices it may require developments in transparent conductors for enabling below band gap light to pass through the device. Also experimental investigations on challenges related to tandem device assembly and manufacturing need to addressed. Further developments in low cost stack tandem technology could lead to

higher efficiency module commercialization and therefore a dramatic increase in the adoption of solar energy in the long run.

# APPENDIX

## List of Abbreviations

| | |
|---|---|
| AM | Air mass |
| CZTS | Copper Zinc Tin Sulfide ($Cu_2ZnSnS_4$) |
| DSSC | Dye-sensitized Solar Cell |
| EIS | Electrochemical impedance spectroscopy |
| EQE | External quantum efficiency |
| FESEM | Field emission scanning electron microscopy |
| FF | Fill factor |
| FTO | Fluorine doped tin oxide |
| GaAs | Gallium Arsenide |
| Ge | Germanium |
| IPCE | Incident-photon-to-current conversion efficiency |
| $J_{SC}$ | Short circuit current density |
| PV | Photovoltaic |
| Si | Silicon |
| TBP | 4-tert-butylpyridine |
| TCO | Transparent conducting oxide |
| TW | Tera ($10^{12}$) Watt |
| $V_{OC}$ | Open circuit voltage |
| XRD | X-ray diffraction |

# BIBILIOGRAPHY


1. US Energy Information Administration. International Energy Outlook 2011. <http://www.eia.gov/forecasts/ieo/pdf/0484(2011).pdf>
2. US Environmental Protection Agency. Global Greenhouse Gas Emissions Data 2007.< http://www.epa.gov/climatechange/ghgemissions/global.html>
3. US Environmental Protection Agency. Total US Greenhouse Gas Emissions by Economic Sector, 2011. <http://www.epa.gov/climatechange/ghgemissions/sources/electricity.html>
4. <http://www.bloomberg.com/news/2013-01-18/u-s-wind-power-accounted-for-6-of-generation-capacity-in-2012.html>
5. <http://www.forbes.com/sites/uciliawang/2013/03/14/u-s-solar-market-grew-76/>
6. Office of Energy Projects Energy Infrastructure Update For December 2012. <http://www.ferc.gov/legal/staff-reports/dec-2012-energy-infrastructure.pdf>
7. European Wind Energy Association. Wind in Power 2012 European Statistics, <http://www.ewea.org/fileadmin/files/library/publications/statistics/Wind_in_power_annual_statistics_2012.pdf>
8. <http://about.bnef.com/press-releases/china-was-worlds-largest-wind-market-in-2012/>
9. Renewables 2012 Global Status Report. <http://www.map.ren21.net/GSR/GSR2012_low.pdf>
10. <http://www.treehugger.com/renewable-energy/after-record-2012-world-wind-power-set-top-300000-megawatts-2013.html>
11. <http://www.pv-tech.org/news/ihs_pv_installs_reached_32gw_in_2012_and_35gw_forecasted_for_2013>
12. <http://online.wsj.com/article/SB10001424052748703579804575441683910246338.html>
13. American Wind Energy Association. 20% Wind Energy by 2030: Wind, Backup Power, and Emissions. <http://www.awea.org/learnabout/publications/upload/Backup_Power.pdf>
14. http://www.atmos.washington.edu/~dargan/587/587_2.pdf.

15. Applied Materials Incorporated. Solar Goes Global. <http://www.appliedmaterials.com/sites/default/files/inline-images/solar-driving-map.jpg>
16. Nayak, P.K., Bisquert, J., and Cahen, D., 2011, "Assessing possibilities and limits for solar cells", Advanced Materials 23(25), pp 2870 - 2876.
17. Mehta, S., 2012. PV Technology, Production and Cost Outlook: 2012-2016. Green Tech Media Research. <http://www.greentechmedia.com/research/report/pv-supply-2012>
18. Oklahoma State University. World Wheat, Corn and Rice Cultivation - 2009. <http://www.nue.okstate.edu/Crop_Information/World_Wheat_Production.htm>
19. University of Durham. Principle of Solar Cells. <https://www.dur.ac.uk/cmp/research/groups/aim/themes/solarcellsprinciple/>
20. Vijayakumar, V., Birnie, D.P., 2013, “Optical and Electronic Simulation of Silicon/ Germanium Tandem Four Terminal Solar Cells”, Journal of Solar Energy Engineering, DOI: 10.1115/1.4024744.
21. Yum, J. H., Jang, S. R., Walter, P., Geiger, T., Nüesch, F., Kim, S., Ko, J., Gratzel, M., and Nazeeruddin, M. K., 2007, "Efficient co-sensitization of nanocrystalline TiO2 films by organic sensitizers", Chemical Communications, (44), pp 4680-4682.
22. Wu, T. Y., Tsao, M. H., Chen, F. L., Su, S. G., Chang, C. W., Wang, H. P., Lin, Y.C, Ou-Yang, W.C., and Sun, I. W., 2010, "Synthesis and characterization of organic dyes containing various donors and acceptors", International journal of molecular sciences, 11(1), pp 329-353.
23. Chang, C. H., and Lee, Y. L., 2007, "Chemical bath deposition of CdS quantum dots onto mesoscopic TiO films for application in quantum-dot-sensitized solar cells", Applied Physics Letters, 91, 053503.
24. Zhao, J., Wang, A., and Green, M.A., 1999, "24.5% Efficiency silicon PERT cells on MCZ substrates and 24.7% efficiency PERL cells on FZ substrates", Prog. in Photovolt. Res. and Appl., **7**(6), pp. 471 - 474. DOI: 10.1002/(SICI)1099-159X(199911/12)7:6<471::AID-PIP298>3.0.CO;2-7.

25. Ameri, T., Dennler, G., Lungenschmied, C., and Brabec, C. J., 2009, "Organic tandem solar cells: A review". Energy & Environmental Science, *2* (4), pp.347-363.
26. Shockley, W., and Queisser, H.J., 1961, "Detailed Balance Limit of Efficiency of pn Junction Solar Cells", J. of Appl. Phys., 32(5), pp.510-519. DOI:10.1063/1.1736034.
27. Henry, C.H., 1980, "Limiting efficiencies of ideal single and multiple energy gap terrestrial solar cells", J. Appl. Phys, **51**(8), pp. 4494 - 4500. DOI: 10.1063/1.328272.
28. King, R.R., Law, D.C., Edmondson, K.M., Fetzer, C.M., Kinsey, G.S., Yoon, H., Sherif, R.A., and Karam, N.H., 2007, "40% efficient metamorphic GaInP/GaInAs/Gemultijunction solar cells", Appl. Phys. Lett., 90(18), 183516. DOI:10.1063/1.2734507.
29. Bertness, K.A., Kurtz, S.R., Friedman, D.J., Kibbler, A.E., Kramer, C., and Olson, J.M., 1990, "29.5% efficient GaInP/GaAs tandem solar cells", Appl.Phys.Lett., 65(8), 989. DOI:10.1063/1.112171.
30. Karam, N.H., King, R., Cavicchi, T.B.,, Krut, D.B., Ermer, J.H., Haddad, M., Cai, L., Joslin, D.E., Takahashi, M., Eldredge, J.W., Nishikawa, W.T., Lillington, D.T., Keyes, B.M., and Ahrenkiel, R.K., 1999, "Development and Characterization of High-Efficiency Ga0.5In0.5P/GaAs/Ge Dual- and Triple-Junction Solar Cells", IEEE Trans. on Electron Devices, 46(10), pp.2116 - 2125. DOI: 10.1109/16.792006.
31. Stanbery, B.J., King, B.D., Burgess, R.M., McClelland, R.W., Kim, N.P., Gale, R.P., and Mickelsen, R.A., 1990, "Lightweight Tandem GaAs /CuInSe Solar Cells", IEEE Trans. on Electron Devices, 37(2), pp.438 - 442. DOI: 10.1109/16.46380.
32. Burgess, R.M., Flora, C., and Schneider, M., 1990, "Performance evaluation of cleft GaAs/CuInSe2 tandem cell circuits through solar simulator testing and computer modeling", 21st IEEE Photovolt. Specialists Conf., 2, pp.1340-1345. DOI: 10.1109/PVSC.1990.111829.

33. Gale, R.P., McClelland, R.W., Dingle, B.D., Gormley, J.V., and Burgess, R.M., 1990, "High-efficiency GaAs/CuInSe2 and AlGaAs/CuInSe2 thin-film tandem solar cells", 21st IEEE Photovolt. Specialists Conf., 1, pp.53-57. DOI: 10.1109/PVSC.1990.111590.
34. Burgess, R.M., Stanbery, B.J., Mickelsen, R.A., Avery, J.E., McClelland, R.W., King, B.D., Boden, M.J., and Gale, R.P., 1988, "High efficiency GaAs/CuInSe2 tandem junction solar cells", 20th IEEE Photovolt. Specialists Conf., 1, pp.457 - 461. DOI: 10.1109/PVSC.1988.105743.
35. Mitchell, K., Eberspacher, C., Ermer, J., and Pier, D., 1988, "Single and tandem junction CuInSe2 cell and module technology", 20th IEEE Photovolt. Specialists Conf., 2, pp.1384 - 1389. DOI: 10.1109/PVSC.1988.105935.
36. Liska, P., Thampi, K.R., Grätzel, M., Brémaud, D., Rudmann, D., Upadhyaya, H.M., and Tiwari, A.N., 2006, "Nanocrystalline dye-sensitized solar cell/copper indium gallium selenide thin-film tandem showing greater than 15% conversion efficiency", Appl. Phys. Lett., 88(20), 203103. DOI: 10.1063/1.2203965.
37. Jeong, W.S, Lee, J.W., Jung, S., Yun, J.H., and Park, N.G., 2011, "Evaluation of external quantum efficiency of a 12.35% tandem solar cell comprising dye-sensitized and CIGS solar cells", Sol. Energy Mater. Sol. Cells, 95(12), pp.3419 - 3423. DOI: 10.1016/j.solmat.2011.07.038.
38. Shpaisman, H., Niitsoo, O., Lubomirsky, I., and Cahen, D., 2008, "Can up- and down-conversion and multi-exciton generation improve photovoltaics?", Sol. Energy Mater. Sol. Cells, 92(12), pp.1541-1546. DOI: 10.1016/j.solmat.2008.08.006.
39. Trupke, T., Green, M.A., and Würfel, P., 2002, "Improving solar cell efficiencies by up-conversion of sub-band-gap light", J. of Appl. Phys., pp.4117 - 4112. DOI: 10.1063/1.1505677.
40. Trupke, T., Green, M.A., and Würfel, P., 2002, "Improving solar cell efficiencies by down-conversion of high-energy photons", J. of Appl. Phys., **92**(7), pp.1668 - 1774. DOI: 10.1063/1.1492021.

41. De Wild, J., Meijerink, A., Rath, J. K., Van Sark, W. G. J. H. M., and Schropp, R. E. I., 2011, "Upconverter solar cells: materials and applications". Energy & Environmental Science, 4(12), pp. 4835-4848.
42. US Department of Energy. Photovoltaic Structures. <http://www.eere.energy.gov/basics/renewable_energy/pv_cell_structures.html>
43. Sharp develops concentrator cell with highest efficiency. <http://sharp-world.com/corporate/news/130614.html>
44. Spectra lab beats unconcentrated PV efficiency record. < http://optics.org/news/4/4/16>
45. Greentech Media. The list of diseased solar companies. < http://www.greentechmedia.com/articles/read/Rest-in-Peace-The-List-of-Deceased-Solar-Companies>
46. Song, J., Li, S.S., Huang, C.H., Anderson, T.J., and Crisalle, O.D., 2003, "Modeling and simulation of a CuGaSe/sub 2//Cu(In/sub 1-x/,Ga/sub x/)Se/sub 2/ tandem solar cell", Proc. of 3rd World Conf. on Photovolt. Energy Convers., 1, pp.555 - 558.
47. Nishiwaki, S., Siebentritt, S., Walk, P., and Ch. Lux-Steiner, M., 2003, "A stacked chalcopyrite thin-film tandem solar cell with 1.2 V open-circuit voltage", Prog. in Photovolt.: Res. and Appl., 11(4), pp.243–248. DOI: 10.1002/pip.486.
48. Seyrling, S., Calnan, S., Bucheler, S., Hupkes, J., Wenger, S., Bremaud, D., Zogg, H., and Tiwari, A.N., 2009, "CuIn1 − xGaxSe2 photovoltaic devices for tandem solar cell application", Thin Solid Films, 517(7), pp.2411–2414. DOI: 10.1016/j.tsf.2008.11.038.
49. Kinoshita, T., Dy, J.T., Uchida, S., Kubo, T., and Segawa, H., 2013, " Wideband dye-sensitized solar cells employing a phosphine-coordinated ruthenium sensitizer", Nature Photonics, 7, pp. 535-539.
50. Flamand, G., Zhao, L., Mols, Y., van der Heide, J., and Poortmans, J., 2009, "Development of mechanically stacked multi-junction solar cells applying thin, one-side contacted III-V cells", Proceedings of the 24th European Photovoltaic Solar Energy Conference and Exhibition-EPVSEC, pp. 126-129.

51. Partain, L. D., Kuryla, M. S., Weiss, R. E., Ransom, R. A., McLeod, P. S., Fraas, L. M., and Cape, J. A., 1987, "26.1% solar cell efficiency for Ge mechanically stacked under GaAs", Journal of applied physics, 62(7), pp. 3010-3015.
52. Beiley, Z.M., and McGehee, M.G., 2012, "Modeling low cost hybrid tandem photovoltaics with the potential for efficiencies exceeding 20%", Energy & Environ. Sci., 5(11), pp.9173-9179. DOI: 10.1039/c2ee23073a.
53. Coutts, T.J., Ward, S.J., Young, D.L., Emery, K.A., Gessert, T.A., and Noufi, R., 2003, "Critical issues in the design of polycrystalline, thin-film tandem solar cells", Prog. in Photovolt: Res. and Appl., 11(6), pp.359–375. DOI: 10.1002/pip.491.
54. < http://pveducation.org/pvcdrom/solar-cell-operation/short-circuit-current>
55. Liu, Y., Sun, Y., and Rockett, A., 2012, "A new simulation software of solar cells—WxAMPS", Sol. Energy Mater. Sol. Cells, 98, pp.124-128. DOI:10.1016/j.solmat.2011.10.010.
56. Fonash, S.J., 2010, "Solar Cell Device Physics", Elsevier.
57. A manual for AMPS 1-D. <http://www.ampsmodeling.org/pdfs/AMPS-1D%20Manual.pdf>
58. Grunow, P., and Krauter, S., 2006, "Modelling of the Encapsulation Factors for Photovoltaic Modules", Conference Record of the 2006 IEEE 4th World Conf. on Photovolt. Energy Conversion, 2, pp.2152-2155. DOI:10.1109/WCPEC.2006.279931.
59. Heavens, O.S., 1965, "Optical Properties of Thin Solid Films", Dover Books.
60. Strehlow WH and Cook EL. Compilation of energy band gaps in elemental and binary compound semiconductors and insulators. <http://www.nist.gov/data/PDFfiles/jpcrd22.pdf>
61. Mitzi, D.B., Gunawan, O., Todorov, T.K., Wang, K., and Guha, S., 2011, "The path towards a high-performance solution-processed kesterite solar cell", Solar Energy Materials and Solar Cells, 95, pp: 1421-1436, DOI: 10.1016/j.solmat.2010.11.028.
62. Gratzel, M., 2009, “Recent Advances in Sensitized Mesoscopic Solar Cells”, Acc. Chem. Res., 42(11), pp 1788–1798.

63. Miyasaka, T., Ikegami, M., and Kijitori, Y., 2007, "Photovoltaic Performance of Plastic Dye-Sensitized Electrodes Prepared by Low-Temperature Binder-Free Coating of Mesoscopic Titania", J. Electrochem. Soc., 154(5), pp. A455-A461.
64. Aurelien Du Pasquier, 2007, "An approach to laminated flexible dye sensitized solar cells", Electrochim. Acta, 52, pp. 7469–7474.
65. Boschloo, G., Lindström, H., Magnusson, E., Holmberg, A., and Hagfeldt, A., 2002, "Optimization of dye-sensitized solar cells prepared by compression method", J. Photochem. Photobiol. A: Chem., 148, pp. 11–15.
66. Lindstrom, H., Holmberg, A., Magnusson, E., Lindquist, S.-E., Malmqvist, L., and Hagfeldt, A., 2001, "A new method for manufacturing nanostructured electrodes on plastic substrates", Nano Lett., 1, pp. 97–100.
67. Miyasaka, T., and Kijitori, Y., 2004, "Low-temperature fabrication of dye-sensitized plastic electrodes by electrophoretic preparation of mesoporous $TiO_2$ layers", J. Electrochem. Soc.,151, pp. A1767–A1773.
68. Yum JH, Kim SS, Kim DY, and Sung YE, 2005,"Electrophoretically deposited TiO2 photo-electrodes for use in flexible dye-sensitized solar cells", J. Photochem. Photobiol. A - Chem., 173 (1), pp. 1-6.
69. United States Geological Survey – Indium, 2009.
70. Toivola, M., Ahlskog, F., and Lund, P., 2006,"Industrial sheet metals for nanocrystalline dye-sensitized solar cell structures", Sol. Energy Mater. Sol. Cells, 90, pp. 2881–289.
71. Kang, M.G., Park, N.G., Ryu, K.S., Chang, S.H., and Kim, K.J., 2006,"A 4.2% efficient flexible dye-sensitized TiO2 solar cells using stainless steel substrate", Sol. Energy Mater. Sol. Cells, 90, pp. 574–581.
72. Jun, Y., and Kang, M.G., 2007,"The Characterization of Nanocrystalline Dye-Sensitized Solar Cells with Flexible Metal Substrates by Electrochemical Impedance Spectroscopy", J. Electrochem. Soc., 154 (1), pp. B68-B71.
73. Jun, Y., Kim, J., Kang, M.G., 2007,"A study of stainless steel-based dye-sensitized solar cells and modules", Sol. Energy Mater. Sol. Cells, 91, pp. 779–784.

74. Park, J.H., Jun, Y., Yun, H.G., Lee, S.Y., and Kang, M.G., 2008,“Fabrication of an Efficient Dye-Sensitized Solar Cell with Stainless Steel Substrate”, J. Electrochem. Soc., 155 (7), pp. F145-F149.
75. Yun, H.G., Jun, Y., Kim, J., Bae, B.S., and Kang, M.G., 2008,“Effect of increased surface area of stainless steel substrates on the efficiency of dye-sensitized solar cells”, Appl. Phys. Lett., 93, page 133311.
76. Fan, X., Wang, F., Chu, Z., Chen, L., Zhang, C., and Zou, D., 2007,“Conductive mesh based flexible dye-sensitized solar cells”, Appl. Phys. Lett., 90, page 073501.
77. Fan, Q., McQuillin, B., Ray, A. K., Turner, M. L., and Seddon, A.B., 2000,“High density, non-porous anatase titania thin films for device applications”, J. Phys. D: Appl. Phys., 33, pp. 2683–2686.
78. Nazeeruddin, M. K., Kay, A., Rodicio, L., Humpbry-Baker, R., Miiller, E., Liska, P., Vlachopoulos, N., and Gratzel, M., 1993,“Conversion of Light to Electricity by cis-XzBis( 2,2’-bipyridyl-4,4’-dicarboxylate)ruthenium(II) Charge-Transfer Sensitizers (X = C1, Br, $I^-$, $CN^-$, and $SCN^-$) on Nanocrystalline Ti02 Electrodes”, J. Am. Chem. Soc.,115, pp. 6382-6390.
79. Ferreira, M. G. S., Hakiki, N. E., Goodlet, G., Faty, S., Simões, A. M. P., and Da Cunha Belo, M., 2001,“Influence of the temperature of film formation on the electronic structure of oxide films formed on 304 stainless steel”, Electrochim. Acta, 46 (24-25), pp. 3767 – 3776.
80. Yoon, K.H., and Kim, J.S.,1986,“Photoelectric Behavior of Sintered $TiO_2$ Electrodes”, J. Phys. Chem., 90, pp. 6488-6491.
81. Gratzel, M., and Howe, R.F.,1990,“Electron Paramagnetic Resonance Studies of Doped $TiO_2$ Colloids”, J. Phys. Chem., 94, pp. 2566-2572.
82. Fischereder, A., Rath, T., Haas, W., Amenitsch, H., Albering, J., Meischler, D., Larissegger, S., Edler, M., Saf, R., and Trimmel, G., 2010,"Investigation of Cu2ZnSnS4 formation from metal salts and thioacetamide", Chemistry of Materials, 22(11), pp. 3399-3406.
83. Neuhaus, D.H., and Münzer, A., 2007, "Industrial Silicon Wafer Solar Cells", Adv. in Opto Electronics, 24521. DOI:10.1155/2007/24521.

84. Hubner, A., Aberle, A.G., and Hezel, R., 1997, "Novel cost-effective bifacial silicon solar cells with 19.4% front and 18.1% rear efficiency", Appl. Phys. Lett., 70(8), pp.1008 -1010. DOI:10.1063/1.118466.
85. Becker, M., Gosele, U., Hofmann, A., and Christiansen, S., 2009, "Highly p-doped regions in silicon solar cells quantitatively analyzed by small angle beveling and micro-Raman spectroscopy", J. of Appl Phys., 106(7), pp.074515 - 074523, DOI:10.1063/1.3236571.
86. Fellmeth, T., Mack, S., Bartsch, J., Erath, D., Jäger, U., Preu, R., Clement, F., and Biro, D., 2011, "20.1% Efficient Silicon Solar Cell With Aluminum Back Surface Field", IEEE Electron Device Lett., 32(8), pp.1101 - 1103. DOI: 10.1109/LED.2011.2157656.
87. Aberle, A.G., 2000, "Surface passivation of crystalline silicon solar cells: a review", Prog. in Photovolt.: Res and Appl., 8(5), pp.473–487. DOI:10.1002/1099-159X(200009/10)8:5<473::AID-PIP337>3.0.CO;2-D.
88. Zhao, L., Zhou, C.L., Li, H.L., Diao, H.W., and Wang, W.J., 2008, "Design optimization of bifacial HIT solar cells on p-type silicon substrates by simulation", Sol. Energy Mater. Sol. Cells, 92(6), pp.673-681. DOI:10.1016/j.solmat.2008.01.018.
89. Zhang, C., and Wei, W., 2011, "Model optimization of nanocrystalline Si:H HIT solar cells", International Conf. on Electric Info. and Control Eng., pp.1464-1468. DOI: 10.1109/ICEICE.2011.5777621.
90. Adachi, S., 1999, "Optical Constants of Crystalline and Amorphous Semiconductors – Numerical Data and Graphical Illustration", Kluwer Academic Publishers.
91. Virginia Semiconductor. General properties of Si, Ge, SiGe, SiO2 and Si3N4. <www.virginiasemi.com/pdf/generalpropertiesSi62002.pdf>
92. Kang, M.H., Ryu, K.R., Upadhyaya, A., Rohatgi, A., 2011, "Optimization of SiN AR coating for Si solar cells and modules through quantitative assessment of optical and efficiency loss mechanism", Prog. in Photovolt.: Res. and Appl., 19(8), pp.983–990. DOI: 10.1002/pip.1095.

93. Mohamed, H.A., and Ali, H.M., 2008, "Characterization of ITO/CdO/glass thin films evaporated by electron beam technique", Sci. and Technology of Adv. Mater., 9(2), 025016. DOI: 10.1088/1468-6996/9/2/025016.
94. Ding, K., Kirchartz, T., Pieters, B.E., Ulbrich, C., Ermes, A.M., Schicho, S., Lambertz, A., Carius, R., and Rau, U., 2011, "Characterization and simulation of a-Si:H/μc-Si:H tandem solar cells", Sol. Energy Mater. Sol. Cells, 95(12), pp.3318-3327. DOI:10.1016/j.solmat.2011.07.023.
95. Posthuma, N.E., Flamand, G., Geens, W., and Poortmans, J., 2005, "Surface passivation for germanium photovoltaic cells", Sol. Energy Mater. Sol. Cells, 88, pp.37-45. DOI:10.1016/j.solmat.2004.10.005.
96. Posthuma, N.E., Van der Heide, J., Flamand, G., and Poortmans, J., 2007, "Emitter Formation and Contact Realization by Diffusion for Germanium Photovoltaic Devices", IEEE Trans. on Electron Devices, 54(5), pp.1210-1215. DOI: 10.1109/TED.2007.894610.
97. Posthuma, N.E., Flamand, G., and Poortmans, J., 2003, "Development of stand-alone germanium solar cells for application in space using spin-on diffusants", Proceedings of 3rd World Conf. on Photovolt. Energy Conversion, 1, pp.777-780.
98. Papet, P., Nichiporuk, O., Kaminski, A., Rozier, Y., Kraiem, J., Lelievre, J.F., Chaumartin, A., Fave, A., Lemiti, M., 2006, "Pyramidal texturing of silicon solar cell with TMAH chemical anisotropic etching", Sol. Energy Mater. Sol. Cells, 90(15), pp.2319-2328. DOI: 10.1016/j.solmat.2006.03.005.
99. Kang, M.H., Ryu, K.R., Upadhyaya, A., Rohatgi, A., 2011, "Optimization of SiN AR coating for Si solar cells and modules through quantitative assessment of optical and efficiency loss mechanism", Prog. in Photovolt.: Res. and Appl., 19(8), pp.983–990. DOI: 10.1002/pip.1095.
100. French, R.H., Rodriguez-Parada, J.M., Yang, M.K., Derryberry, R.A., Lemon, M.F., Brown, M.J., Haeger, C.R., Samuels, S.L., Romano, E.C., and Richardson, R.E., 2009, "Optical properties of materials for concentrator photovoltaic systems", 34th IEEE Photovolt. Specialists Conf., pp.000394-000399. DOI: 10.1109/PVSC.2009.5411657.

101. Rubin, M., 1985, "Optical properties of soda lime silica glasses", Sol. Energy Mater., 12, pp.275-288. DOI:10.1016/0165-1633(85)90052-8.
102. Green, M.A., Emery, K., Hishikawa, Y., Warta, W., and Dunlop, E.D., 2012, "Solar cell efficiency tables (version 39)", Prog. in Photovolt.: Res. and Appl., 20(1), pp.12–20. DOI: 10.1002/pip.2163.
103. Mishima, T., Taguchi, M., Sakata, H., and Maruyama, E., 2010, "Development status of high-efficiency HIT solar cells", Sol. Energy Mater. Sol. Cells. 95(1), pp.18-21. DOI:10.1016/j.solmat.2010.04.030.
104. Bozler, C. O., McClelland, R. W. and J. C. C. Fan, 1981,"Ultrathin, high efficiency solar cells made from GaAs films prepared by the CLEFT Process" IEEE Electron Devic. Lett. 2 (8), pp. 203-205. DOI: 10.1109/EDL.1981.25402.
105. Bauhuis, G. J., Mulder, P., Haverkamp, E. J., Huijben, J. C. C. M., and Schermer, J. J., 2009,"26.1% thin-film GaAs solar cell using epitaxial lift-off. Sol. Energ. Mat. Sol. C.", 93(9), pp. 1488-1491. DOI: 10.1016/j.solmat.2009.03.027.
106. Mattos, L. S., Scully, S. R., Syfu, M., Olson, E., Yang, L., Ling, C., Kayes, B.M. and He, G., 2012,"New module efficiency record: 23.5% under 1-sun illumination using thin-film single-junction GaAs solar cells", 38th IEEE Photovolt. Specialists Conf. pp. 003187-003190. DOI: 10.1109/PVSC.2012.6318255.
107. Belghachi, A., and Helmaoui, A., 2008,"Effect of the front surface field on GaAs solar cell photocurrent", Sol. Energ. Mat. Sol. C., 92(6), pp. 667-672. DOI:10.1016/j.solmat.2008.02.003.
108. Plá, J., Barrera, M., and Rubinelli, F., 2007,"The influence of the InGaP window layer on the optical and electrical performance of GaAs solar cells", Semicond. Sci. Tech. 22(10), pp. 1122-1130. DOI: 10.1088/0268-1242/22/10/008.
109. Lee, K., Zimmerman, J. D., Zhang, Y. and Forrest, S. R., 2012, "Epitaxial lift-off of GaAs thin-film solar cells followed by substrate reuse", 38th IEEE Photovolt. Specialists Conf., pp. 001698-001700. DOI: 10.1109/PVSC.2012.6317922.
110. Griggs, M. J., Kayes, B. M. and Atwater, H. A., 2006,"pn junction heterostructure device physics model of a four junction solar cell", Proc. of the SPIE, page. 6339, 63390D. DOI: 10.1117/12.680793.

111. Siqueiros, J. M., Machorro, R., and Regalado, L. E., 1988,"Determination of the optical constants of MgF2 and ZnS from spectrophotometric measurements and the classical oscillator method", Appl. Optics. 27(12), pp. 2549-2553. DOI: 10.1364/AO.27.002549.
112. Gee, J. M., and Virshup, G. F., 1988,"A 31% efficient GaAs / silicon mechanically stacked, multijunction concentrator solar cel", 20th IEEE Photovolt. Specialists Conf. 1, pp. 00754-00758. DOI: 10.1109/PVSC.1988.105803.
113. Flamand, G., Zhao, L., Mols, Y., Van der Heide, J., and Poortmans, J, 2009, "Development of Mechanically Stacked Multi-Junction Solar Cells Applying Thin, One-side Contacted III-V Cells", 24th European Photovolt. Sol. Energy Conf., pp. 126-129. DOI: 10.4229/24thEUPVSEC2009-1BO.5.5.
114. Lin, L. J., and Chiou, Y. P., 2012,"Improving thin-film crystalline silicon solar cell efficiency with back surface field layer and blaze diffractive grating", Sol. Energy, 86(5), pp. 1485-1490. DOI: 10.1016/j.solener.2012.02.009.
115. Fellmeth, T., Mack, S., Bartsch, J., Erath, D., Jäger, U., Preu, R., Clement, F., and Biro, D., 2011,"20.1% Efficient Silicon Solar Cell With Aluminum Back Surface Field", IEEE Electron Device Lett., 32(8), pp. 1101 - 1103. DOI: 10.1109/LED.2011.2157656.
116. Zhao, L., Li, H. L., Zhou, C. L., Diao, H. W., and Wang, W. J., 2009,"Optimized resistivity of p-type Si substrate for HIT solar cell with Al back surface field by computer simulation", Sol. Energy, 83(6), pp. 812-816. DOI: 10.1016/j.solener.2008.11.007.
117. Dwivedi, N., Kumar, S., Bisht, A., Patel, K., and Sudhakar, S., 2013,"Simulation approach for optimization of device structure and thickness of HIT solar cells to achieve ~ 27% efficiency", Sol. Energy, 88, pp. 31-41. DOI: 10.1016/j.solener.2012.11.008.
118. Dao, V.A., Heo, J., Choi, H., Kim, Y., Park, S., Jung, S., Lakshminarayan, N., and Yi, J., 2010,"Simulation and study of the influence of the buffer intrinsic layer, back-surface field, densities of interface defects, resistivity of p-type silicon substrate and transparent conductive oxide on heterojunction with intrinsic thin-

layer (HIT) solar cell", Sol. Energy, 84(5), pp. 777-783. DOI: 10.1016/j.solener.2010.01.029.

119. Chen, A., and Zhu, K., 2012,"Computer simulation of a-Si/c-Si heterojunction solar cell with high conversion efficiency", Sol. Energy, 86(1), pp. 393-397. DOI: 10.1016/j.solener.2011.10.015.
120. Burschka, J., Pellet, N., Moon, S.J., Baker, R.H., Gao, P., Nazeeruddin, M.K., and Grätzel, M., 2013, " Sequential deposition as a route to high-performance perovskite-sensitized solar cells", Nature, 499, pp 316-319.
121. Saad, M., Riazi, H., Bucher, E., and Lux-Steiner, M.C., 1996, "$CuGaSe_2$ solar cells with 9.7% power conversion efficiency", Applied Physics A, 62(2), pp 181-185.
122. Jeong, W. S., Lee, J. W., Jung, S., Yun, J. H., and Park, N. G., 2011, "Evaluation of external quantum efficiency of a 12.35% tandem solar cell comprising dye-sensitized and CIGS solar cells", Solar Energy Materials and Solar Cells, 95(12), pp. 3419-3423.